REMOTE SENSING OF WET SNOW PROCESSES IN A CONTROLLED LABORATORY ENVIRONMENT

by

Christopher Paul Donahue

A dissertation submitted in partial fulfillment
of the requirements for the degree

of

Doctor of Philosophy

in

Mechanical Engineering

MONTANA STATE UNIVERSITY
Bozeman, Montana

May 2022

ACKNOWLEDGEMENTS

The work presented in this dissertation was supported by the National Aeronautics and Space Administration (NASA) New Investigator Program award 80NSSC18K0822. I would also like to thank the Blake W. Morstad Memorial Scholarship and the American Avalanche Association Graduate Student Research Grant for financial support during my PhD.

Thank you to my academic advisor, Dr. Kevin Hammonds, for taking a chance on a truck engineer and introducing me to studying snow for a living. Thank you for allowing me to pursue my own ideas and for providing funding to keep me going throughout my PhD.

Thank you to my PhD committee for accepting the invitation to participate in my PhD work – Dr. HP Marshall, Dr. Joseph Shaw, and Dr. Dan Miller.

Thanks to my fellow graduate students for engaging in discussions about my research and for helping out in the laboratory during data collection - Michael Dvorsak, Kristian Jones, Evan Schehrer, and James Dillon.

I would like to acknowledge the Subzero Research Laboratory at Montana State University, where I spent many hours of my life over the past five years and thank you Dr. Ladean McKittrick for always being willing to help me out in the lab.

Thanks to Doug Roberts and Will Tidd at Sensorlogic Inc. for providing the radars used in this study and for answering many of my questions as I learned about radar.

To my family and friends, thank you for your love and support, I am forever grateful.

To McKenzie, thank you for sharing your brilliance with me and for being such an amazing life & adventure partner.

TABLE OF CONTENTS

TABLE OF CONTENTS CONTINUED

TABLE OF CONTENTS CONTINUED

LIST OF TABLES

LIST OF FIGURES

LIST OF FIGURES CONTINUED

Figure Page

LIST OF FIGURES CONTINUED

Figure Page

LIST OF FIGURES CONTINUED

LIST OF FIGURES CONTINUED

Figure Page

ABSTRACT

Water flow through snow, due to snowmelt or rain-on-snow events, is a heterogeneous process that has implications for snowmelt timing and magnitude, snow metamorphism, albedo evolution, and avalanche hazard. Remote sensing technologies, ranging from ground-based to satellite-borne scales, offer a non-destructive method for monitoring seasonal snowpacks, although there is no single technique that is ideal for monitoring snow. Wet snow, specifically, presents a challenge to both optical and radar remote sensing retrievals. The primary aim of this dissertation was to develop wet snow remote sensing methods from within a controlled laboratory environment, allowing for precise characterization of snow properties. Experiments were conducted by preparing laboratory snow samples of prescribed structures and monitoring them during and after melt using hyperspectral imaging and polarimetric radar. Snow properties were characterized using X-ray computed microtomography, a dielectric liquid water content sensor, and serial-section reconstructions. In addition to laboratory experiments, hyperspectral imaging snow property retrieval methods were developed and tested in the field during wet snow conditions at the ground-based scale.

The primary outcomes from this work were three new remote sensing applications for monitoring wet snow processes. First, a new hyperspectral imaging method to map effective snow grain size was developed and used to quantify grain growth due to wet snow metamorphism. Second, the optimal radiative transfer mixing model to simulate wet snow reflectance was determined and used to map liquid water content in snow in 2- and 3-dimensions. Lastly, snow melt progression was monitored using continuous upward-looking polarimetric radar and it was found, by comparison to 3-dimensional liquid water content retrievals from hyperspectral imaging, that the cross-polarized radar signal was sensitive to the presence of preferential flow paths. The work presented here highlights the utility of using a multi-sensor fusion approach to snow remote sensing. Although these laboratory remote sensing experiments were at a small scale, the remote sensing instrument response to specific snow conditions directly translates to larger scales, which is valuable to support algorithm development for ground, airborne, and spaceborne remote sensing missions.

CHAPTER ONE

INTRODUCTION

Motivation

Snow is a large natural reservoir of fresh water and about one-sixth of the world's population rely on snowmelt for human consumption and agriculture (Barnett and others, 2005). For instance, in the western United States up to 75% of the fresh water supply comes from annual snowmelt in the mountains (Simpkins, 2018). As the world faces climate change, population growth, and land-use change, the need for accurate knowledge of water resources held in the form of snow in mountain environments will continue to grow (Bales and others, 2006). However, accurate snow measurements remain a challenge because much of the Earth's snow cover is in remote and isolated terrain.

In recent decades, optical and radar remote sensing technology has advanced our ability to measure key snow parameters through spaceborne, airborne, and ground-based platforms. However, gaps remain in snow remote sensing knowledge and many opportunities exist for better interpretation of these datasets. One important gap is remote sensing of wet snow properties because the presence of liquid water, hereafter referred to as water, changes snow into a three-phase material (i.e., ice, water, and air), which impacts the physical, optical, and dielectric properties. Additionally, the changes to these properties are spatially and temporally variable due to the infiltration of water into the snowpack being heterogenous and the liquid water content (LWC) varying over diurnal cycles.

Broadly, snow remote sensing knowledge gaps motivated the recent multiyear NASA SnowEx campaign (https://snow.nasa.gov/campaigns/snowex) focused on testing multiple instrument types in a variety of snow environments. Testing snow remote sensing instrumentation in the field is challenging, though, because snow conditions cannot be fully characterized over large spatial scales. It is advantageous to supplement these efforts with small-scale laboratory remote sensing experiments where prescribed snow microstructures can be created, perturbed, and fully characterized in a controlled environment. This dissertation addresses knowledge gaps related to the retrieval of wet snow properties from near-infrared (NIR) hyperspectral imaging and polarimetric radar in situ within a laboratory environment.

Optical Remote Sensing

Optical remote sensing makes use of sensors that detect reflected radiation in the solar spectrum (i.e., visible and infrared). Optical properties, which describe light interactions and the probability of reflection and absorption at different wavelengths, vary across different material types. By measuring reflected radiation at multiple wavelengths, optical remote sensing platforms can leverage unique reflectance signatures to classify materials or determine material characteristics.

In the cryosphere, there is a long legacy of mapping snow and ice extent from satellite optical remote sensing (Hori and others, 2017), which plays an important role in Earth’s climate system. More recently, it has been demonstrated that physical snow properties, such as snow grain size (Nolin & Dozier, 2000, Painter and others, 2009, Seidel and others, 2016), concentrations of light absorbing particles (LAPs) (Skiles and others, 2018, Bair and others, 2021), and LWC (Hyvarinen & Lammasniemi, 1987, Green and others, 2002) can also be retrieved using measured spectral reflectance from optical remote sensors at scales ranging from satellite to ground-based. The ability to quantify these physical snow properties remotely provides useful data about the state of the snowpack, that can be used for climate, hydrology, and avalanche forecasting because they control snow albedo, snowmelt timing, and snow stability.

The basis for being able to retrieve physical snow properties from spectral reflectance lies in knowing the optical properties of snow constituents (i.e., ice, air, water, and LAPs) and their relative size and abundance. In practice, a radiative transfer model inversion technique is commonly used, which compares measured spectral reflectance to a simulated spectral reflectance based on input physical parameters. This dissertation primarily focuses on near-infrared optical remote sensing of snow, where reflectance signatures are controlled by snow grain size and LWC (Warren, 1982). The following sections provide prerequisite background on the optical properties of snow and give a brief overview of radiative transfer modeling, both of which are used extensively throughout Chapters 2-4.

Optical Properties of Snow

The optical properties of pure substances, including ice and water, are described by the spectral complex refractive index (N_λ)

$$N_\lambda = n_\lambda + ik_\lambda \tag{1}$$

The real component (n_λ) describes how fast light travels through a medium, while the imaginary component (k_λ) describes how radiation is absorbed as a wave propagates through the material. For ice and water, there is minimal variation in the real component across the solar spectrum, whereas the imaginary component increases across the same range by orders of magnitude. This means that in the visible wavelengths (380-750 nm) pure water, in both its liquid and solid phase, is essentially transparent and becomes increasing absorptive in the NIR (750-2500 nm). Although the absorption patterns across the NIR are similar between ice and water, there are shifts that distinguish the different phases that can be leveraged using optical remote sensors. To illustrate this point, the spectral complex refractive index for ice (Warren & Brandt, 2008) and water (Rowe and others, 2020) across the NIR wavelengths ranging from 700 – 2500 nm are shown in Figure 1.

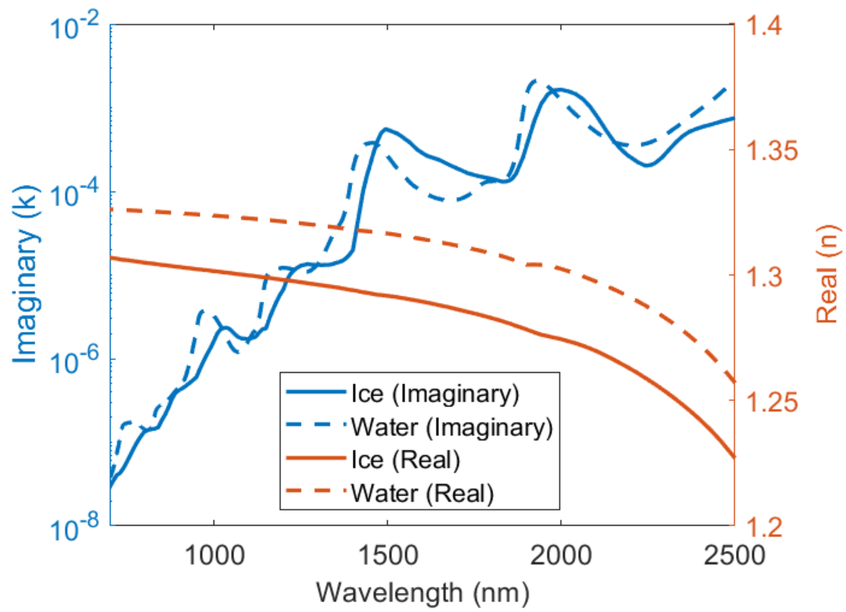

Figure 1. Complex refractive index of pure ice (Warren & Brandt, 20087) and pure water (Rowe and others, 2020) in near-infrared wavelengths ranging from 700-2500 nm.

Snow is a mixed medium and the reflectance is determined by the complex refractive index of its constituents (i.e., ice, air, water). These control light-snow interactions by determining the probability that an incident photon at the snow surface is absorbed, transmitted, or reflected at an ice-air interface (Wiscombe & Warren, 1980). In the visible wavelengths, photons can travel long distances without being absorbed and the opportunity for scattering increases with each interaction at ice-air interfaces. This accounts for the high reflectivity of snow in the visible wavelengths. In the NIR wavelengths, where ice and water are more absorptive, the probability that a photon will be absorbed is dependent on the path length traveled through these materials. The path length increases as snow grains grow larger, or water content increases, hence snow reflectance in this wavelength range is dependent on grain size and LWC (Warren, 1982). To illustrate this, example NIR reflectance spectra are shown for variations in grain size and LWC, in Figure 2, which were generated using a radiative transfer simulation and is discussed further in the next section.

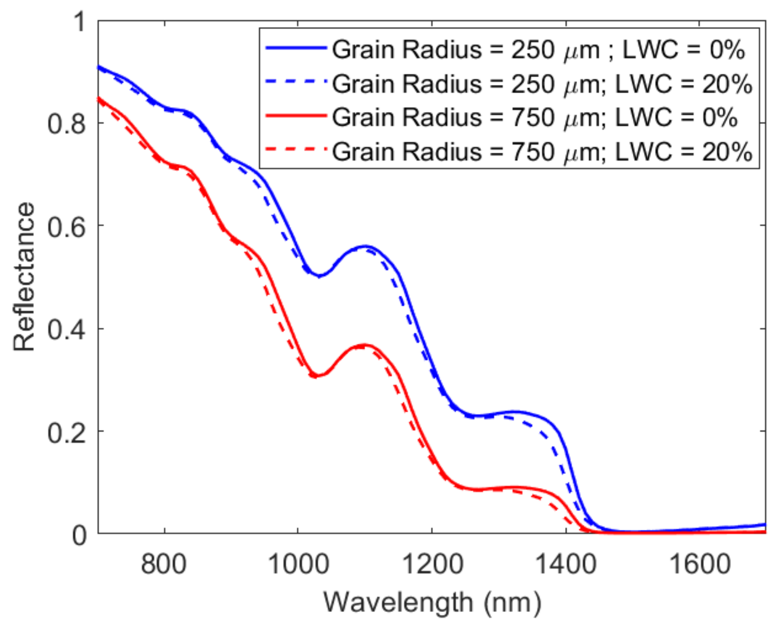

Figure 2. Example snow reflectance spectra showing the impact from grain size and liquid water content (LWC). Figure generated using simulated reflectance spectra output from the Discrete-Ordinate Radiative Transfer Model (DISORT).

Optical Radiative Transfer Modeling

Light interaction with snow grains is a complex process due to the irregular grain shapes and multiple scattering. To model snow reflectance, first, the single scattering properties of snow constituents (i.e., ice and water) is modeled. This is done for a single particle that acts independently, and is described by three dimensionless optical parameters; the absorption efficiency (Q_{abs}), scattering efficiency (Q_{sca}), and asymmetry factor (g) (Gardner & Sharp, 2010). To simplify the calculation, snow grains are commonly modeled as spheres with radius r_e, referred to as the effective grain radius. Leveraging this simplification, the single scattering properties of snow grains can be modeled with Mie scattering theory (Bohren & Huffman, 2008) using the well characterized optical properties (complex refractive index) of ice and water presented in the previous section.

Single scattering optical properties can then be used with the radiative transfer equation to model multiple scattering properties, representing light interactions between multiple grains. Of interest to this research are two radiative transfer models (1) Snow, Ice, and Aerosol Radiative (SNICAR) model (Flanner & Zender, 2005) and (2) Discrete Ordinates Radiative Transfer (DISORT) (Stamnes and others, 1988). SNICAR is computationally favorable because integration of the radiative transfer equation is not computed, but rather a two-stream approximation is used, meaning radiation propagating along only two discrete directions is considered. The output is hemispheric angularly integrated reflectance, or albedo, for a given illumination direction (i.e., directional-hemispherical reflectance) or diffuse light condition (i.e., hemispherical-hemispherical reflectance). DISORT is a more complex model, capable of handling multiple-streams and calculates the angular distribution of spectral reflectance which has been defined by Dozier and Painter (2004) as

$$R_\lambda(\theta_0, \phi_0; \theta_r, \phi_r) = \frac{\pi L_\lambda(\theta_r, \phi_r)}{cos\theta_0 E_{\lambda,direct}(\theta_0, \phi_0) + E_{\lambda,diffuse}} \qquad (2)$$

Where L_{λ} is reflected spectral radiance, $E_{\lambda,direct}$ is the direct incident irradiance on a surface normal to the beam, $E_{\lambda,diffuse}$ is the diffuse incident irradiance and R_{λ} is the spectral directional reflectance. The zenith and azimuth angles are defined as θ and ϕ, and the subscripts *0* and *r* signify incident and reflected, respectively. The spectral albedo is found by integrating R_{λ} over the entire upward-looking hemisphere.

Both radiative transfer models have been used extensively to model the scattering behavior of dry snow (Painter and others, 2007, Skiles & Painter, 2018), which has been used to generate lookup tables of simulated spectral reflectance for the purpose of inverting remotely sensed reflectance to physical snow properties. These types of retrievals have been performed at multiple scales and instrument types. Conversely, radiative transfer modeling of snow has not extended into a rigorous treatment of the scattering behavior of wet snow (Dozier & Painter, 2004). There have been two case studies that have proposed optical property mixing models for simulating wet snow reflectance, however, retrievals from these models have yet to be quantitatively assessed.

Radar Remote Sensing of Snow

Radar, an active remote sensing system, uses antennas to transmit electromagnetic (EM) waves and receive backscattered EM waves from the targeted object to determine its properties. Traditionally, radar has been used to determine distance (ranging) and velocity of an object by leveraging the two-way travel time and phase change of the returned wave. Additionally, the orientation of the EM wave, or polarization, can be leveraged to extract geometrical structure, shape, and orientation of the object (Lee & Pottier, 2017). Over the past several decades, radar has been proven to be a prominent tool for terrestrial snow monitoring because EM waves in the microwave frequencies penetrate into the snowpack, making it possible to retrieve volumetric properties quickly and non-destructively.

Applications of radar remote sensing of snow vary with platform scale (i.e., spaceborne, airborne, or ground-based) and frequency. At the satellite scale, for example, synthetic aperture radar (SAR) acquires high resolution radar image datasets, which have been used to estimate volumetric snow properties by analyzing the integrated radar backscatter, such as snow water equivalent (SWE) (Lievens and others, 2019, Rott and others, 2010). Ground-based radar, on the other hand, measures the two-way travel time of backscatter returns from multiple layers (i.e., full waveform), which are caused by variations in the dielectric properties within the snowpack. The backscatter signals can be used to characterize vertical snow profiles and identify stratigraphy (Marshall and others, 2007), in addition to retrieving volumetric properties (Ellerbruch & Boyne, 1980). The suitability for snow property retrieval varies with frequency; higher frequencies (shorter wavelengths) are sensitive to snow microstructure (Rutter and others, 2019) and are better for resolving stratigraphy, whereas lower frequencies (longer wavelengths) are less sensitive to snow microstructure and are better for volumetric properties (Mitterer and others, 2011). Additionally, the orientation of the EM wave can be used for retrievals relating to snow structure (Leinss and others, 2016).

Generally, analysis of radar data for snow property retrieval relies on understanding the dielectric properties of snow and the backscatter behavior, which is frequency and polarization dependent. This dissertation, in Chapter 4, uses these principles to investigate wet snow processes within the volume of a snowpack. The following sections describe these principles in more detail.

Dielectric Properties of Snow

In general, snow is a dielectric material, meaning EM waves can propagate through the material with minimal conduction. The effective relative permittivity (ε_{eff}) of snow is a complex number consisting of a real and imaginary component that describes the dielectric properties, similar to the complex refractive index described in the previous optical remote sensing section. The real component describes the velocity at which the EM wave travels through the material and the imaginary component describes the absorption of the EM wave. For mixed-media materials, such as snow, ε_{eff} is determined by taking the weighted average of the relative permittivity (ε_r) for the constituents of the material (i.e., ice, air, and water) (Matzler and others, 1984). Ice is a low-loss material, meaning that a microwave can propagate through the material without much energy loss, while water is a high-loss material, meaning that energy is dissipated quickly. For comparison, the unitless ε_r of ice is 3.15 while the value for water is 80 (Hallikainen, 1977). In general, ε_{eff} is a function of snow density, volumetric LWC, frequency, temperature, and the shape of water inclusions (Hallikainen and others, 1986).

In dry snow conditions, the real part (ε_d') is a function of dry snow density (ρ_d) and is generally independent of frequency in the microwave range if the very small imaginary part (ε_d'') is neglected (Matzler, 1996). Many empirical relationships between snow density and dielectric constant have been derived (Ambach & Denoth, 1980, Hallikainen and others, 1982), but for practical purposes, a simple linear relationship can be used (Tiuri and others, 1984)

$$\varepsilon_d' = \varepsilon_{eff} = 1 + 2\rho_d \quad (3)$$

The microwave velocity in a snowpack is directly related to ε_{eff} and can be used to determine volumetric properties, such as total snow height (h), layer thickness, and SWE ($SWE = \rho_d h$) (Mitterer and others, 2011)

$$v = \frac{c}{\sqrt{\varepsilon_{eff}}} = \frac{c}{\sqrt{1 + 2\rho_d}} = \frac{h}{t} \quad (4)$$

where c is the speed of light in a vacuum, v is the wave speed in the snow, and t is the travel time. However, equation (4) contains two unknowns (ρ_d and h) and therefore a priori knowledge of one of these parameters must be known to calculate SWE. Commonly, though, ρ_d is estimated using energy balance models (Marks and others, 1999) and h is solved for using the radar two-way travel time.

In wet snow conditions, radar measurements are more complicated because snow becomes a three-phase mixture of ice, air, and water. The presence of water increases microwave absorption and even small amounts of water (2-3% by volume) leads to high dielectric loss, which drastically affects radar backscatter and decreases penetration depth (Winebrenner and others, 1998, Rott and others, 1988). The penetration depth of a microwave in wet snow is inversely proportional to frequency (i.e., higher frequency has lower penetration). Radar frequencies ranging from L to C band (1-8 GHz) have proven to be suitable for measuring wet snow from a seasonal snowpack, because they have adequate penetration depth (Mitterer and others, 2011, Shi & Dozier, 1995, Marshall and others, 2004).

To predict ε_{eff} for wet snow, three-phase dielectric mixing models have been developed. A commonly used mixing model, for example, was developed by Roth and others (1990)

$$\varepsilon_{eff} = \left[\theta_w \varepsilon_w^{\beta} + (1-n)\varepsilon_i^{\beta} + (n-\theta_w)\varepsilon_a^{\beta}\right]^{\frac{1}{\beta}} \tag{5}$$

where θ_w is the volume fraction of water, $\varepsilon_{i,a,w}$ is the relative permittivity for the three constituents (i.e., ice (i), air (a), and water (w)), β is a factor considering the different layering of a snowpack, and *n* is the porosity of snow. Similar to dry snow, ε_{eff} of wet snow can also be used to calculate SWE. However, in this case the calculation of ε_{eff} relies on many potentially unknown variables and an empirically derived factor (β). These types of models have been shown to closely match in situ measurements (Roth and others, 1990, Hallikainen and others, 1986, Heilig and others, 2015), though, benefited from a priori knowledge of the snowpack properties from measurements. For global snow remote sensing, prior knowledge of the snowpack is not possible, thus radar measurements of wet snow remain a challenge.

Polarimetric Backscatter

A polarimetric radar independently transmits and receives microwaves in a vertical (V) and horizontal (H) polarization state. Full polarimetric data includes co-polarization transmit-receive, i.e., vertical-vertical (VV) and horizontal-horizontal (HH), and cross-polarization transmit-receive, i.e., vertical-horizontal (VH) and horizontal-vertical (HV). Generally, co-polarization returns are dominated by single scattering reflections, such as stratigraphy layers (Marshall and others, 2007), and cross-polarization returns are a result of multiple scattering (Kendra and others, 1998). In dry snow, multiple scattering can occur at the snow-grain scale when the wavelength is of similar size or smaller than the ice particles. In wet snow, the heterogenous infiltration of water causes water inclusions that can be much larger than the ice particle size alone, which likely causes multiple scattering within the snow volume. The application of polarimetric radar data to snow is a relatively recent advancement and the scattering behavior of microwaves within the porous media is not fully understood.

The total radar backscatter (σ_{pq}^{tot}) over a snowpack can be approximated using a four-component model for transmit-receive polarizations p and q (Ulaby, 1982)

$$\sigma_{pq}^{tot} = \sigma_{pq}^{air-snow} + \sigma_{pq}^{snowvol} + \sigma_{pq}^{snowvol-grnd} + T_{pq}^2 * L_{pq}^2 * \sigma_{pq}^{grnd} \quad (6)$$

where $\sigma_{pq}^{air-snow}$is the backscatter from the air snow interface, $\sigma_{pq}^{snowvol}$ is the volume scattering component in the snowpack, $\sigma_{pq}^{snowvol-grnd}$ is the interaction between the volume scattering and the snow-ground interface, and σ_{pq}^{grnd} is ground scattering component, which is attenuated by the snowpack through the power transmission coefficient T_{pq} at the air-snow interface and the snow volume attenuation factor L_{pq}. Each backscatter component is visualized in Figure 3, which was adapted from Liang and Wang (2020).

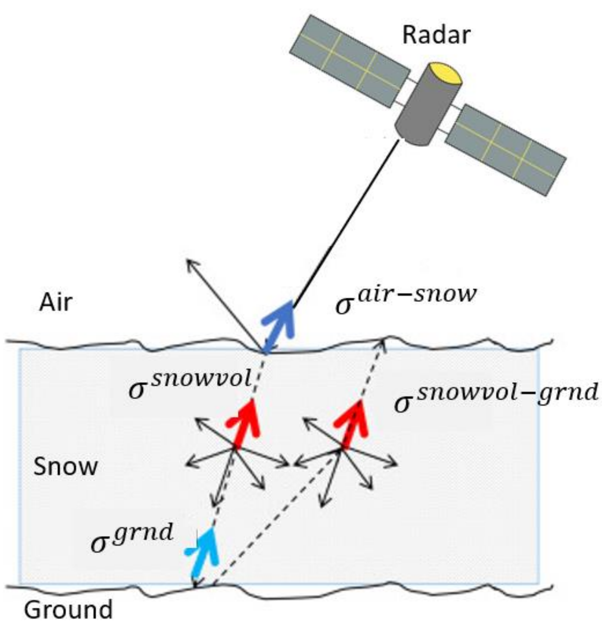

Figure 3. Illustration of the four radar backscatter components from a snow-covered ground. Figure adapted from Liang & Wang (2020).

Research Gap and Objectives

Understanding wet snow processes and snowmelt timing is of interest to the avalanche and hydrology communities because the presence of water directly impacts snow stability and runoff timing. Using remote sensing to monitor these processes is an active area of research, but challenges remain due to the heterogenous nature of melt initiation and water infiltration in a snowpack over space and time. Water is first introduced into a snowpack at the surface during melt initiation or rain-on-snow events. Once the surface layer becomes saturated, water percolates vertically into deeper layers of the snowpack, which is generally classified by two mechanisms: (1) matrix flow and (2) preferential flow (Colbeck, 1979, Schneebeli, 1995). Matrix flow describes a semi-uniform vertical melting front, while preferential flow describes concentrated vertical water pathways that extend deep into the snowpack beyond matrix flow (Webb and others, 2018). Matrix flow typically has broad horizontal extent that is relatively easy to identify using radar remote sensing (Mitterer and others, 2011), whereas preferential flow paths are spatially variable and typically vertically oriented, making them difficult to detect non-destructively using remote sensing techniques.

At the ground-based scale, radars are commonly pulled on a sled to collect transects (McGrath and others, 2019) or mounted to a tower for continuous monitoring (Marshall & Robertson, 2016), both of which collect data in a downward-looking nadir configuration relative to the top of the snow surface. When snowmelt initiates, radars in this configuration get large magnitude returns at the snow surface and microwave penetration into the snowpack is reduced, making it difficult to track snowmelt progression. To mitigate this problem, some studies (Gubler & Hiller, 1984, Mitterer and others, 2011) have buried radars in the ground in an upward-looking configuration to monitor the snowpack from below. This configuration is advantageous in wet snow conditions because the radar can track homogenous matrix flow as it moves towards the radar (Mitterer and others, 2011), however, preferential flow paths have yet to be detected using upward- or downward-looking radar systems.

Previous studies using upward-looking radar to monitor wet snow have used single co-polarized radar systems, which are generally limited to detecting planar single-scattered features in the snowpack, like the horizontal extent of matrix flow. Prior to the research presented here, a polarimetric radar had yet to be used in an upward-looking configuration to monitor snowmelt processes, but it could provide additional information about the orientation and structure of melt pathways, like vertical preferential flow paths. The primary goal of this dissertation was to investigate using a polarimetric radar in an upward-looking configuration to determine if cross-polarized radar returns could be leveraged to help classify wet snow process (i.e., matrix vs preferential flow). To achieve this goal, experiments were conducted in a controlled laboratory environment where snow layer structure and snow melt timing could be controlled, and the final state of the wet snow sample could be precisely characterized.

To meet the primary goal, new methodology was needed to characterize laboratory snow samples at the scale (~ 0.5 m^3) of radar experiments in terms of LWC and grain size distribution. Previous to this work, in situ instruments were limited to discrete point measurements for LWC (Denoth, 1994, A2 Photonic Sensors, 2019) and grain size (Painter and others, 2007, Gergely and others, 2014), which do not adequately capture the spatial variability of snow microstructure. Similarly, X-ray computed microtomography (micro-CT) is frequently used in laboratory experiments to measure snow grain size and other microstructural properties, but the sample size used for analysis is relatively small (cm scale) compared to the scale at which patterns in water infiltration manifest. The need for new methodology to accomplish the primary goal spurred objectives 1-3 of this dissertation, aimed at developing optical remote sensing methods that could quantify snow properties in high spatial resolution maps, rather than discrete point measurements.

The first objective was to develop an effective snow grain size mapping method using hyperspectral imaging, which could be used to characterize grain growth due to the presence of water (i.e., wet snow metamorphism). Building upon the first objective, the second objective was to develop a hyperspectral imaging method to map the LWC across the vertical profile of a wet snow sample. Although these two retrieval methods were developed in a laboratory, they were subsequently tested in the field by imaging a snowpit sidewall. Using the results from objectives one and two, the third objective was to reconstruct the retrieved snow properties in 3-dimensions using a serial-sectioning approach, which could be used for comparison to the polarimetric radar measurements.

Dissertation Outline

The main body of this dissertation includes two chapters that develop snow property retrieval methods using hyperspectral imaging. The third chapter presents polarimetric upward-looking radar snowmelt experiments that were compared against the snow property retrievals developed in the first two chapters. In Chapter 2, effective grain size was retrieved using the established scaled band area method (Nolin & Dozier, 2000), which limited retrievals to dry snow conditions before and after snowmelt. The retrievals were assessed against those from a field spectrometer (Painter and others, 2007) and micro-CT (Flin and others, 2004, Schneebeli &

Sokratov, 2004) and an illumination angle sensitivity study was conducted. Chapter 3 presents a hyperspectral imaging method to map LWC and effective grain size simultaneously in wet snow conditions, which was needed to characterize wet snow samples for radar interpretation. Three wet snow optical property mixing models were used in radiative transfer modeling to simulate wet snow reflectance, which were used to invert hyperspectral images to retrieve per-pixel LWC. Each model was tested against in situ LWC measurements to determine the optimal model for wet snow radiative transfer simulations. The results from Chapters 2 and 3 were combined in Chapter 4 with hyperspectral serial-section imaging to reconstruct snow properties into a 3D model, which was used for comparison to upward-looking polarimetric radar returns during snowmelt experiments. The contents in Chapter 2 and 3 have been published in peer-reviewed open-access journals and Chapter 4 was submitted to a peer-reviewed open-access journal and is currently under review. An abstract for each chapter is included in the outline below.

Chapter 2: In situ effective grain size mapping using a compact hyperspectral imager

This chapter was published in the Journal of Glaciology and is reprinted here in journal formatting.

Donahue, C., Skiles, S. M., & Hammonds, K. (2021). In situ effective snow grain size mapping using a compact hyperspectral imager. *Journal of Glaciology*, *67*(261), 49-57.

Abstract

Effective snow grain radius (r_e) is mapped at high resolution using near-infrared hyperspectral imaging (NIR-HSI). The NIR-HSI method can be used to quantify r_e spatial variability, change in r_e due to metamorphism, and visualize water percolation in the snowpack. Results are presented for three different laboratory-prepared snow samples (homogeneous, ice lens, fine grains over coarse grains), the sidewalls of which were imaged before and after melt induced by a solar lamp. The spectral reflectance in each ~3 mm pixel was inverted for r_e using the scaled band area of the ice absorption feature centered at 1030 nm, producing r_e maps consisting of 54 740 pixels. All snow samples exhibited grain coarsening post-melt as the result of wet snow metamorphism, which is quantified by the change in r_e distributions from pre- and post-melt images. The NIR-HSI method was compared to r_e retrievals from a field spectrometer and X-ray computed microtomography (micro-CT), resulting in the spectrometer having the same mean r_e and micro-CT having 23.9% higher mean r_e than the hyperspectral imager. As compact hyperspectral imagers become more widely available, this method may be a valuable tool for assessing r_e spatial variability and snow metamorphism in field and laboratory settings.

Chapter 3: Mapping liquid water content in snow at the millimeter scale: an intercomparison of mixed-phase optical property models using hyperspectral imaging and in situ measurements

This chapter was published in The Cryosphere and is reprinted here in journal formatting.

Donahue, C., Skiles, S. M., & Hammonds, K. (2022). Mapping liquid water content in snow at the millimeter scale: an intercomparison of mixed-phase optical property models using hyperspectral imaging and in situ measurements. *The Cryosphere*, *16*(1), 43-59.

Abstract

It is well understood that the distribution and quantity of liquid water in snow is relevant for snow hydrology and avalanche forecasting, yet detecting and quantifying liquid water in snow remains a challenge from the micro- to the macro-scale. Using near-infrared (NIR) spectral reflectance measurements, previous case studies have demonstrated the capability to retrieve surface liquid water content (LWC) of wet snow by leveraging shifts in the complex refractive index between ice and water. However, different models to represent mixed-phase optical properties have been proposed, including (1) internally mixed ice and water spheres, (2) internally mixed water-coated ice spheres, and (3) externally mixed interstitial ice and water spheres. Here, from within a controlled laboratory environment, we determined the optimal mixed-phase optical property model for simulating wet snow reflectance using a combination of NIR hyperspectral imaging, radiative transfer simulations (Discrete Ordinate Radiative Transfer model, DISORT), and an independent dielectric LWC measurement (SLF Snow Sensor). Maps of LWC were produced by finding the lowest residual between measured reflectance and simulated reflectance in spectral libraries, generated for each model with varying LWC and grain size, and assessed against the in situ LWC sensor. Our results show that the externally mixed model performed the best, retrieving LWC with an uncertainty of ~ 1 %, while the simultaneously retrieved grain size better represented wet snow relative to the established scaled

band area method. Furthermore, the LWC retrieval method was demonstrated in the field by imaging a snowpit sidewall during melt conditions and mapping LWC distribution in unprecedented detail, allowing for visualization of pooling water and flow features.

Chapter 4: Laboratory observations of preferential flow paths in snow using upward-looking polarimetric radar and hyperspectral imaging

This chapter is under review for Remote Sensing and the preprint is reprinted here in journal formatting.

Donahue C., Hammonds K., Laboratory observations of preferential flow paths in snow using upward-looking polarimetric radar and hyperspectral imaging. Submitted to *Remote Sensing* on 22 March 2022, In Review

Abstract

Infiltration of liquid water in a seasonal snowpack is a complex process that consists of two primary mechanisms: a semi-uniform melting front, or matrix flow, and heterogeneous preferential flow paths. Distinguishing between these two mechanisms is important for monitoring snow melt progression, which is relevant for hydrology and avalanche forecasting. It has been demonstrated that single co-polarized upward-looking radar can be used to track matrix flow, whereas preferential flow paths have yet to be detected. Here, from within a controlled laboratory environment, continuous polarimetric upward-looking C-band radar was used to monitor melting snow samples to determine if cross-polarized radar returns were sensitive to the

presence and development of preferential flow paths. The experimental dataset consisted of six samples, for which the melting process was interrupted at increasing stages of preferential flow path development. Using a new serial-section hyperspectral imaging method, polarimetric radar returns were compared against the 3-dimensional liquid water content distribution and preferential flow path morphology. It was observed that the cross-polarized signal increased by 13.1 dB across these experiments. This comparison showed that the metrics used to characterize the flow path morphology related to the increase in cross-polarized radar returns spanning the six samples, indicating that upward-looking polarimetric radar has potential to identify preferential flow paths.

CHAPTER TWO

IN SITU EFFECTIVE SNOW GRAIN SIZE MAPPING USING A COMPACT HYPERSPECTRAL IMAGER

Manuscript in Chapter 2

Author: Christopher Donahue

Contributions: Conceptualized the study, conducted laboratory experiments, performed radiative transfer simulations using SNICAR, processed and analyzed all data, analyzed results, prepared original draft manuscript, created visualizations, and handled response to peer-reviews.

Co-Author: S. McKenzie Skiles

Contributions: Advised CD during study conceptualization and SNICAR modeling and reviewed and edited the original draft manuscript.

Co-Author: Kevin Hammonds

Contributions: Acquired funding for this research, was responsible for project administration, supervised CD throughout the study, and reviewed and edited the original draft manuscript.

Manuscript Information

Christopher Donahue, S. McKenzie Skiles, and Kevin Hammonds
Journal of Glaciology
Status of Manuscript:
____ Prepared for submission to a peer-reviewed journal
____ Officially submitted to a peer-reviewed journal
____ Accepted by a peer-reviewed journal
__x__ Published in a peer-reviewed journal

Cambridge University Press
Submitted: 17 February 2020
Accepted: 22 July 2020
First Published Online: 18 August 2020
Published in Print: February 2021
Volume 67, Issue 261, Pages 49-57
https://doi.org/10.1017/jog.2020.68

Journal of Glaciology

In situ effective snow grain size mapping using a compact hyperspectral imager

Christopher Donahue[1], S. McKenzie Skiles[2] and Kevin Hammonds[1]

[1]Department of Civil Engineering, Montana State University, Bozeman, MT, USA and [2]Department of Geography, University of Utah, Salt Lake City, UT, USA

Article

Cite this article: Donahue C, Skiles SM, Hammonds K (2021). In situ effective snow grain size mapping using a compact hyperspectral imager. *Journal of Glaciology* **67** (261), 49–57. https://doi.org/10.1017/jog.2020.68

Received: 17 February 2020
Revised: 21 July 2020
Accepted: 22 July 2020
First published online: 18 August 2020

Keywords:
Crystal growth; remote sensing; snow; snow metamorphosis

Author for correspondence:
Christopher Donahue,
E-mail: christopher.donahue2@student.montana.edu

Abstract

Effective snow grain radius (r_e) is mapped at high resolution using near-infrared hyperspectral imaging (NIR-HSI). The NIR-HSI method can be used to quantify r_e spatial variability, change in r_e due to metamorphism, and visualize water percolation in the snowpack. Results are presented for three different laboratory-prepared snow samples (homogeneous, ice lens, fine grains over coarse grains), the sidewalls of which were imaged before and after melt induced by a solar lamp. The spectral reflectance in each ~3 mm pixel was inverted for r_e using the scaled band area of the ice absorption feature centered at 1030 nm, producing r_e maps consisting of 54 740 pixels. All snow samples exhibited grain coarsening post-melt as the result of wet snow metamorphism, which is quantified by the change in r_e distributions from pre- and post-melt images. The NIR-HSI method was compared to r_e retrievals from a field spectrometer and X-ray computed microtomography (micro-CT), resulting in the spectrometer having the same mean r_e and micro-CT having 23.9% higher mean r_e than the hyperspectral imager. As compact hyperspectral imagers become more widely available, this method may be a valuable tool for assessing r_e spatial variability and snow metamorphism in field and laboratory settings.

1. Introduction

Snow grain size is a physical property of snow that exerts controls on snow reflectance (Wiscombe and Warren, 1980), and is used to characterize mechanisms of snow metamorphism and stratigraphy (Colbeck, 1991). At the surface, characterizing the snow grain size is critical for modeling snow albedo, a primary control for snow energy balance and snowmelt timing (Marks and Dozier, 1992). Whereas stratigraphy, or the vertical distribution of snow grain size, is critical for modeling microwave radiative transfer (Brucker and others, 2011) and understanding mechanical (Pielmeier and Schneebeli, 2003) and thermodynamic (Hammonds and others, 2015) properties of a snowpack.

There are multiple ways to characterize snow grain size. The classical snow grain size, defined as the largest extension (mm) of a snow grain, is most simply observed using a crystal card and hand lens (Fierz and others, 2009). Whereas the specific surface area (SSA) is defined as the surface area per unit volume and is measured using stereology methods. Snow grain size can also be described as an effective grain radius (r_e), which is used to approximate the scattering and absorption properties of snow. Grenfell and Warren (1999) demonstrated that a collection of spherical ice particles with the same volume-to-surface area ratio as snow (i.e. characterized with stereology methods) could be used to model hemispherical reflectance. The effective grain radius is directly related to SSA by:

$$\mathrm{SSA} = \frac{3}{r_e}. \tag{1}$$

In the near-infrared (NIR) wavelengths (800–2500 nm), snow spectral reflectance has a characteristic decline due to the increasing absorptivity of ice at these wavelengths. Reflectance, therefore, has an inverse relationship with grain size in this wavelength range because absorption is a function of the amount of ice per unit volume. For the same snow layer, NIR reflectance typically declines over time because grain coarsening occurs due to snow metamorphism. Leveraging this relationship, methods have been developed to retrieve r_e from various instruments that measure snow reflectance by relating the magnitude of NIR reflectance, or area/depth of distinct ice absorption features, to r_e. Broadly, these can be classified as either discrete measurements or mapping techniques, and further characterized by the spectral range and resolution of the instrument.

At the landscape scale, remote-sensing techniques are used to map r_e on a pixel-wise basis from surface reflectance. It has been shown that spaceborne multispectral sensors, like the Moderate Resolution Imaging Spectroradiometer (MODIS), can be used to map r_e using band ratios or spectral unmixing (Painter and others, 2009, 2012). These satellite datasets have value due to their record length, spatial coverage and temporal resolution, but high degrees of uncertainty result from mixed pixels and low spectral resolutions. For airborne imaging spectrometers, like the Airborne Visible/Infrared Imaging Spectrometer (AVIRIS), r_e is mapped at the scale of tens of meters by inverting the shape of ice absorption features resolved in spectral reflectance with radiative transfer modelling (Nolin and Dozier, 2000; Seidel and others, 2016). Spatial and spectral resolution are much higher, and uncertainty lower compared to spaceborne platforms, but due to logistics and cost, airborne datasets are very limited in spatial extent and temporal coverage.

At the local scale (i.e. laboratory, plot, snow pit) field spectrometers are used to retrieve discrete measurements of r_e from surface spectral reflectance, or along the vertical snow profile (∼2 cm) when coupled to a contact probe, known as contact spectroscopy (Painter and others, 2007). Lower spectral resolution field instruments have also been developed to measure r_e from small discrete snow samples (∼3 cm) using an integrating sphere and NIR light source, from which reflectance is empirically related, or calibrated, to known reflectance from a range of snow grain sizes. Examples of these instruments include DUFISSS (Gallet and others, 2009), IceCube (Zuanon and A2 Photonic Sensors, 2013) and Infrasnow (Gergely and others, 2014). Similarly, a vertical profiler, POSSSUM, has been developed to measure SSA profiles in one-dimension from measurements of reflectance at 1310 nm with a vertical resolution of 10 mm (Arnaud and others, 2011). Discrete measurements can be time consuming to collect, are limited to instrument field of view/sample size, and cannot efficiently capture spatial variability. This can be addressed by mapping r_e, which has been demonstrated using a digital NIR photographic method (Matzl and Schneebeli, 2006). NIR photography correlates snow reflectance from 840 to 940 nm to SSA, measured using stereology methods, and is high resolution (∼1 mm). However, because this method uses an empirical calibration from reflectance across a single short NIR wavelength range, it is sensitive to illumination conditions and is not easily transferable between camera sensors. Currently, there is no high spatial and high spectral resolution method for mapping r_e at the local scale.

This gap is addressed here with NIR hyperspectral imaging (NIR-HSI) using a Resonon Pika NIR-320 compact hyperspectral imager and rotational stage mounted on a tripod, shown in Figure 1, to map the NIR spectral reflectance of snow. From the per pixel spectral reflectance, r_e is retrieved by applying the Nolin-Dozier (N-D) scaled band area inversion technique (Nolin and Dozier, 2000). To demonstrate this method, we present results from three laboratory-prepared snow samples with varying initial conditions that underwent induced melt and subsequent wet snow metamorphism. In general, when liquid water is introduced into a snowpack, snow grains begin rapid metamorphism and larger snow grains tend to grow at the expense of smaller grains (Marsh, 1987). By mapping r_e before and after melt, we demonstrate the ability of this technique to map snow stratigraphy for a wide range of r_e values. Further, it is shown that mapping r_e can be used to study wet snow metamorphism processes, filling a gap in current methodologies.

In previous laboratory experiments investigating liquid water flow through snow and wet snow metamorphism, dye tracers have been used to visualize water transport (Gerdel, 1954), preferential flow channels (Schneebeli, 1995) and capillary barriers (Avanzi and others, 2016). With dye tracers, the flow and pooling of water can be visualized, but quantification of grain growth with a hand lens or stereology methods is difficult and time consuming. In other laboratory work, X-ray computed microtomography (micro-CT) has been used to investigate preferential flow (Avanzi and others, 2017). Although snow grain size and many other snow properties can be accurately measured with micro-CT, the spatial resolution is often limited by the sample size limitations of the instrument.

In the results shown here, we demonstrate that when using the NIR-HSI method to map r_e, preferential flow can be visualized, water pooling at interfaces can be identified, and grain growth at the laboratory or snow pit scale can be more effectively quantified, all at a higher spatial resolution than these previous methods. Additionally, a series of experiments were conducted to assess the sensitivity of the NIR-HSI method to illumination angle and general repeatability using homogeneous unperturbed snow samples. In all experiments, our results are validated by comparing the r_e retrieval from the hyperspectral imager to established in situ field spectrometer (Painter and others, 2007) and micro-CT (Flin and others, 2004; Schneebeli and Sokratov, 2004) retrieval methods for quantifying r_e.

2. Methods

2.1 Instrument

For the NIR-HSI method presented here, a Resonon Inc. (Bozeman, MT, USA) Pika NIR-320 near-infrared hyperspectral imager was used. This imager is a compact line-scan imager (also called a 'push-broom' scanner), meaning 2-D images are constructed by collecting the image line by line while the imager translates or rotates relative to the sample (https://resonon.com/). This instrument covers the spectral range from 900 to 1700 nm across 164 channels, resulting in a spectral resolution of 4.9 nm, at 14-bit radiometric resolution. The imager has 320 spatial channels with a sensor pixel size of 30 µm. The operating temperature of the imager, per its datasheet, is 5–40 °C. Following the experiments at −5 °C, it was confirmed by the manufacturer that the optical alignment had not deteriorated, indicating the initial calibration was not compromised by cold temperatures.

The scanner was mounted onto the Resonon rotational stage for imaging perpendicular to the snow sample sidewall at a distance of 100 cm (Fig. 1), resulting in a spatial resolution of ∼3 mm. Two 500-watt halogen lamps mounted on a tripod were located perpendicular to the snow sample for equal illumination of the sidewall. For calibration from digital number to the bidirectional reflectance factor, a Spectralon 99% diffuse white reference reflectance panel was placed in the scene of each hyperspectral image. Using the proprietary Resonon Spectronon software, snow sample sidewalls were imaged with an integration time of 8.05 ms, frame rate of 124 Hz and a scanning speed of 7.7 deg s^{-1}. Before processing, each image was cropped such that only the exposed face of the snow sample was used for the retrieval of r_e.

2.2 Effective grain radius retrieval

Following N-D, the spectra at each pixel in the hyperspectral image was inverted for r_e using the scaled band area (A_b), which is calculated by integrating the continuum-scaled ice absorption feature centered at λ = 1030 nm (Nolin and Dozier, 2000).

$$A_b = \int_{\lambda=984\,\text{nm}}^{\lambda=1087\,\text{nm}} \frac{R_{\text{cont},\lambda} - R_{\text{snow},\lambda}}{R_{\text{cont},\lambda}} \mathrm{d}\lambda, \tag{2}$$

where $R_{\text{snow},\lambda}$ is the measured snow reflectance at wavelength λ and $R_{\text{cont},\lambda}$ is the continuum reflectance at wavelength λ, defined as the slope between the shoulders of the ice absorption feature, which represents what the reflectance spectrum would be in the absence of ice absorption. To help visualize the scaled band area and continuum reflectance, Figure 2a illustrates them as the shaded gray area and solid red line, respectively. Here, the end points are the reflectance values from the Pika NIR-320 bands centered at λ = 984 nm and λ = 1087 nm, with the integral taken over the 21 bands between end points. We chose to use 984 nm, which narrows the range relative to N-D, because it is not impacted by noise at the lower limit of the Pika NIR-320 hyperspectral sensor (900 nm). By integrating relative to the continuum reflectance, the grain size

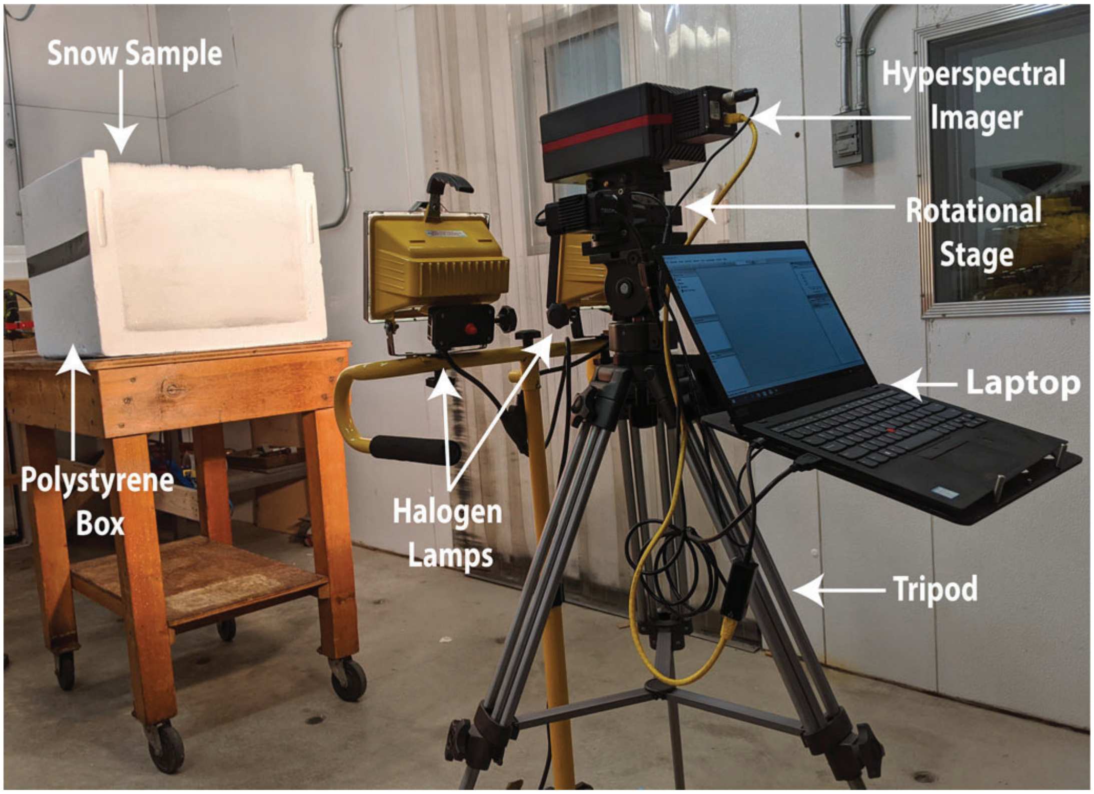

Fig. 1. Laboratory setup showing a laboratory-prepared snow sample, two halogen lamps, a Resonon Pika NIR-320 hyperspectral imager and a rotational stage mounted on a tripod inside a cold room. The hyperspectral imager is located 100 cm from the exposed snow sample sidewall.

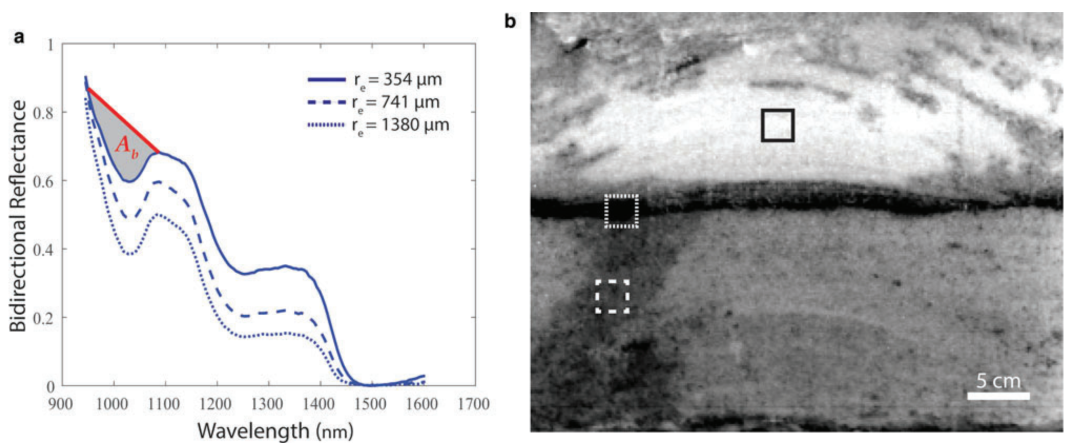

Fig. 2. (a) Three snow spectra are plotted from a single pixel located within the boxes of (b). For the solid line spectrum, an example of the scaled band area (A_b) is shaded gray, which corresponds to an effective grain radius (r_e) of 354 µm. The continuum reflectance, shown as the red line, is the slope between the shoulders of the ice absorption feature (λ = 984 nm and λ = 1087 nm). (b) Gray scale near-infrared image of the post-melt fine grain over coarse grains snow sample at λ = 1030 nm taken with the Resonon Pika NIR-320 hyperspectral imager. Each box represents an area with a different r_e.

estimates are independent of the magnitude of reflectance (Nolin and Dozier, 2000). This means that r_e retrievals should also be relatively insensitive to variability in illumination that can result from slight deviations of the imager and light source from normal incidence, relative to the snow sample sidewall and Spectralon panel, although this was assessed separately (see Section 2.4.2).

Nolin and Dozier (2000) validated their model with a crystal card, hand lens and stereology measurements, finding that retrieved r_e matched measurements with a correlation coefficient of $r = 0.997$. They also assessed the sensitivity of the method to instrument noise, finding that retrieved r_e between 30 and 900 µm could vary by ± 10–50 µm. The signal-to-noise ratio (SNR) used for AVIRIS in the study was 100, whereas the SNR for the Resonon Pika NIR-320 is 1885. With the better SNR and higher spectral resolution of the Pika NIR-320, the NIR-HSI method should be more robust with respect to sensor noise, when compared to the N-D method applied to AVIRIS.

In place of the Discrete Ordinates Radiative Transfer Program, or DISORT (Stamnes and others, 1988) used by N-D, the theoretical snow spectra in this study were modeled with the Snow, Ice, and Aerosol Radiative Transfer Model, or SNICAR (Flanner and others, 2007). SNICAR simulates radiative transfer through a snowpack comprised of spherical grains of ice at a given grain size and illumination geometry using the updated ice optical property compilation of Warren and Brandt (2008). Model inputs include illumination angle, r_e (µm), snow layer thickness (m), snow density (kg m^{-3}) and when appropriate, concentrations of light-absorbing particles (ppb). In this case, we simulated snow directional-hemispherical reflectance for clean snow only, by running the model iteratively through r_e values between 30 and 1500 µm. The other forcing inputs were held constant at values that best represent the bulk characteristics of the snow sample; 300 kg m^{-3} snow density, 0° illumination angle (light source perpendicular to snow surface) and a single optically thick snow layer. We did not vary the snow layer thickness because light penetration in the NIR is very shallow (0.5–3 cm) and grain size can be considered mostly homogeneous at this scale (Warren, 1982; Nolin and Dozier, 2000). We also did not vary snow density because density has little to no effect on snow reflectance (Bohren and Beschta, 1979).

To help visualize the NIR hyperspectral image, a grayscale image at $\lambda = 1030$ nm is shown in Figure 2b. In each pixel, r_e is determined through the best match to the theoretical scaled band area values contained within a lookup table (Supplementary Material Table S1), populated from modeled snow spectra using SNICAR. In Figure 2a, three snow spectrums are plotted from single pixels located within the boxes in Figure 2b, representing areas in the image with different r_e. Smaller grains are highlighted with the solid line box in an area where there was no water percolation. Larger grains and ice are highlighted in the dotted line box where there was water pooling at the capillary barrier then refreezing. Medium-sized grains are highlighted in the dashed line box where there was a preferential flow path. For the solid line spectrum in Figure 2a, an example of the scaled band area (A_b) is shown, which corresponded to $r_e = 354$ µm using the lookup table.

2.3 Laboratory experiments

To demonstrate the novelty of the NIR-HSI method presented here, three laboratory-prepared snow samples with varying snow stratigraphy were analyzed initially and post-melt in the Subzero Research Laboratory (SRL) at Montana State University. The stratigraphy scenarios were homogeneous snow, a snow sample with an ice lens placed in the middle and a snow sample with fine grains sieved over coarse grains. In all cases, snow collected outside was sieved into a polystyrene box (42.5 cm × 42.5 cm × 38.1 cm) with a removable top and sidewall. The homogeneous snow sample was prepared by sifting snow using a 0.68 mm sieve. For the ice lens, snow grains were initially sifted using a 1.2 mm sieve, followed by fine misting water that had been chilled to 0 °C over the snow sample, such that it froze on contact creating an ice 'lens'. Once the ice lens was completely frozen, the top layer of snow grains was sifted on top of the ice lens using the same 1.2 mm sieve. For the snow sample with fine grains placed over the top of coarse grains, the coarse grains at the bottom were sieved with a range of 1.5–5 mm, while the fine grains on top were sifted using a 1.2 mm sieve.

An initial hyperspectral image of each snow sample sidewall was taken to map r_e prior to melt, under the assumption that the stratigraphy was approximately uniform throughout the snow sample. The snow samples were then placed under a metal-halide lamp that simulates the complete solar spectrum for ∼6 h, while the room temperature was held constant at −5 ± 1 °C. The homogeneous snow sample was subjected to a simulated solar irradiance of 800 W m^{-2}, while the ice lens and fine over coarse grain samples were subjected to a simulated solar irradiance of 650 W m^{-2}. Once the solar lamp was turned off, the snow samples were moved to a separate storage chamber within the SRL and held at −30 °C for rapid refreezing. After 24 h at −30 °C, the sidewall of the polystyrene box was removed to reveal the snow stratigraphy, like viewing a snow pit wall in the field. Each snow sample sidewall was serial sectioned using a snow saw at intervals of 3–5 cm, with hyperspectral images taken of the sidewall between the removal of each section. Each image was processed using the methodology outlined above in Section 2.2 to map r_e across each image. To illustrate this method, we present one imaged cross-section for each snow sample, initially and post-melt.

2.4 Method assessment

2.4.1 Instrument comparison

To assess the validity of the NIR-HSI method, the r_e retrieval from the hyperspectral imager was compared to retrieval methods using a field spectrometer and micro-CT. A homogeneous snow sample (1 mm sieved snow grains) was prepared using the method described in Section 2.3 and the snow sample sidewall was measured with each instrument for comparison. The snow sample sidewall was first imaged with the hyperspectral imager, resulting in 54 570 spatial pixels, which was inverted to r_e using the method described in Section 2.2.

Next, using the same halogen light source and white reference panel, sidewall reflectance was measured using an Analytical Spectral Devices (ASD) FieldSpec 4 High Resolution field spectrometer, which has a spectral range of 350–2500 nm, and spectral bandwidth of 1.1 nm in the NIR. To reduce shadowing, the halogen light source was positioned to the side of the spectrometer (15° off nadir). The field of view was reduced using an 8° fore optic, which was held perpendicular to the sidewall at a distance of ∼4 cm from the snow surface, resulting in an approximate spot size of 5.6 mm. Following a white reference measurement, 30 discrete measurements of snow reflectance were made in a space covering a grid pattern. Each spectrum was then inverted for r_e using the method described in Section 2.2 but using a separate lookup table for an illumination angle of 15°.

Last, five snow sub-samples were cut from the snow sample sidewall for measurement using a SkyScan 1173 micro-CT housed in a −10°C cold room in the SRL. Samples were measured in a 33 mm diameter × 67 mm long cylindrical tube that allowed for a voxel size of 19.4 µm. Measurements were taken using a 42 kV, 190 mA X-ray beam, 100 ms exposure time, and each sample was rotated 180° at 0.7° increments. The scanning time of each sample was ∼25 min and all five samples were measured within 3 h of the hyperspectral imager and field spectrometer measurements. Additionally, a 3 × 3 × 3 median filter was applied to the reconstructed images, thresholding of the grey-scale images into ice and air phases was performed by visual inspection, and a despeckling filter was used to remove both white and black speckles <25 voxels. The volume and surface area of each snow sample was measured in 3D based on the marching cubes method (Lorensen and Cline, 1987). The total surface area calculated from the proprietary Bruker micro-CT analysis software (CTAn) includes 'false' surface area from the volume of interest intersecting snow grains, which is believed to add a positive bias to the measured SSA. Conversely, removing the intersection surface area from the total surface area results in a negative bias to the measured SSA, whereas the actual SSA resides somewhere in the middle. Therefore, we report the average SSA value measured by including intersection surface area and removing intersection surface area to calculate r_e using Eqn (1).

To quantitatively compare r_e retrievals between each instrument, the mean, std dev. and distributions of r_e were compared and visualized. Furthermore, each measurement from the micro-CT and field spectrometer was overlaid onto the r_e map produced by the hyperspectral imager to visualize the spatial variability between all retrievals. These results are shown in Section 3.2.

2.4.2 Sensitivity to illumination angle

Because it is an important control on NIR reflectance, the NIR-HSI method relies on the illumination angle to be correctly accounted for when generating r_e lookup tables. At higher incidence angles, a photon will, on average, undergo its first scattering event closer to the surface which increases the probability of scattering in an upward direction, exiting the snowpack without being absorbed (Warren, 1982). Therefore, for the same r_e, reflectance increases with illumination angle, resulting in smaller A_b values. For example, Figure 3 shows the directional-hemispherical reflectance at 0°, 30° and 45° illumination angles for an r_e of 100 µm modeled using SNICAR. In assessing the sensitivity of the retrieval of r_e to illumination angle, we note that although for modeling purposes we assume the halogen lights are at 0°, there are slight variations from this in our experiments. This is due to two factors, (1) the two halogen lights can be independently rotated, and (2) the lights must be placed slightly below the scanning stage to not obstruct the field of view of the imager.

The sensitivity of the r_e retrieval to variation in illumination angle was assessed by comparing consecutive images of the same homogeneous snow sample sidewall, prepared following the procedure in Section 2.2. While the hyperspectral imager remained stationary and perpendicular to the snow sample sidewall, the halogen lights were moved from 0° to 45° illumination angles at increments of 5°. To demonstrate the error that can result from not specifying the correct illumination angle, each image was processed using the lookup table for a 0° illumination angle and compared to additional lookup tables generated with SNICAR for the corresponding illumination angles.

2.4.3 Repeatability

Multiple images of a homogeneous snow sample were also used to assess sensitivity to sensor noise and investigate the precision of the r_e retrieval. To accomplish this, the snow sample sidewall was imaged five consecutive times over a 3 min time period without any changes made to the experimental setup. To compare the consistency in r_e retrievals, we compare the range of values from each image using a box plot analysis and assess spatial differences with pixel by pixel std dev. However, since it was not possible to exactly align pixels between images, std dev. were calculated over 3.5 cm^2 subregions of the image. This represents the average std dev. across ∼20 × 20 pixels in the original images.

3. Results and discussion

3.1 Laboratory experiment

In Figures 4a–f, r_e is shown for the three laboratory-prepared snow samples initially and post-melt. Although the lookup table

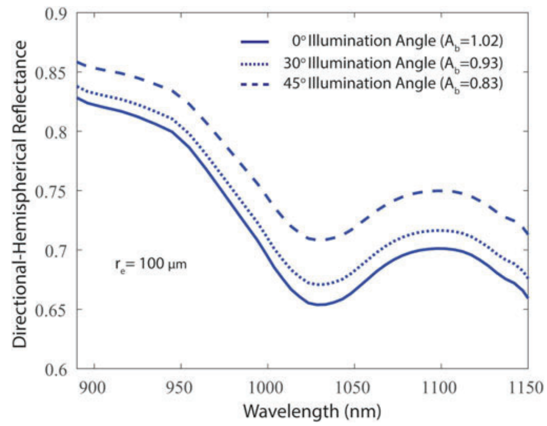

Fig. 3. Directional-hemispherical reflectance at 0°, 30° and 45° illumination angles for effective grain radius (r_e) of 100 µm modeled using SNICAR. Scaled band area (A_b) of the ice absorption feature centered at 1030 nm decreases with increasing illumination angle.

for these measurements is populated for grains with r_e ranging from 30 to 1500 µm, to increase contrast and improve visualization, the color bar used in Figure 4 ranges from only 30 to 1000 µm. Grains outside the range of the lookup table are white ($r_e \geqslant 1500$ µm) and classified as ice. In Figures 4g–i, the initial and post-melt r_e distributions are plotted to show the shift in r_e due to grain coarsening during wet snow metamorphism (Raymond and Tusima, 1979). Interestingly, the r_e maps reveal patterns in the stratigraphy profile, seen best in initial images Figures 4a–c, which are due to the laboratory sifting process. This is the first time, of which we are aware, that this pattern has been captured and shows that although still relatively homogeneous at the sample scale, the sifting process itself does introduce spatial variability.

Prior to melt, the homogeneous snow sample mean r_e was 149 µm (std dev. (σ) = 17 µm), whereas the post-melt mean r_e was 191 µm (σ = 53 µm) (Figs 4a, d). The sample was prepared in a way that classical grain size would be homogeneous throughout the sample, and the homogeneity was also present in the mapped r_e, with the corresponding distribution being relatively narrow and unimodal (Fig. 4g). Post-melt, the r_e increased and the distribution widened due to grain coarsening and wet snow metamorphism. This example demonstrates that this method can be used to quantify and map the magnitude of grain coarsening post-melt and visualize preferential flow channels in refrozen snow (Fig. 4g).

Initial mean r_e for the snow sample containing an ice lens was 211 µm (σ = 41 µm), and the post-melt mean r_e was 395 µm (σ = 148 µm) (Figs 4b, e). Like the homogeneous sample, the corresponding distribution (Fig. 4h) is unimodal, but with a broader r_e range for both the initial and post-melt r_e maps. In the initial image, it is evident that the shift in the distribution relative to the homogeneous sample is primarily due to the larger grains associated with the ice lens. In the post-melt image, r_e has generally increased across the full image, and the r_e map shows evidence of preferential flow channels and pooling water at the ice lens interface.

In the fine over coarse grain snow sample, the initial mean r_e was 292 µm (σ = 110 µm), while the post-melt mean r_e was 452 µm (σ = 192 µm) (Figs 4c, f). The layer of fine grains over coarse grains is clearly visualized in the initial and post-melt r_e maps, and corresponding distributions (Fig. 4i), which were bimodal. In the post-melt image, evidence of water pooling at the interface

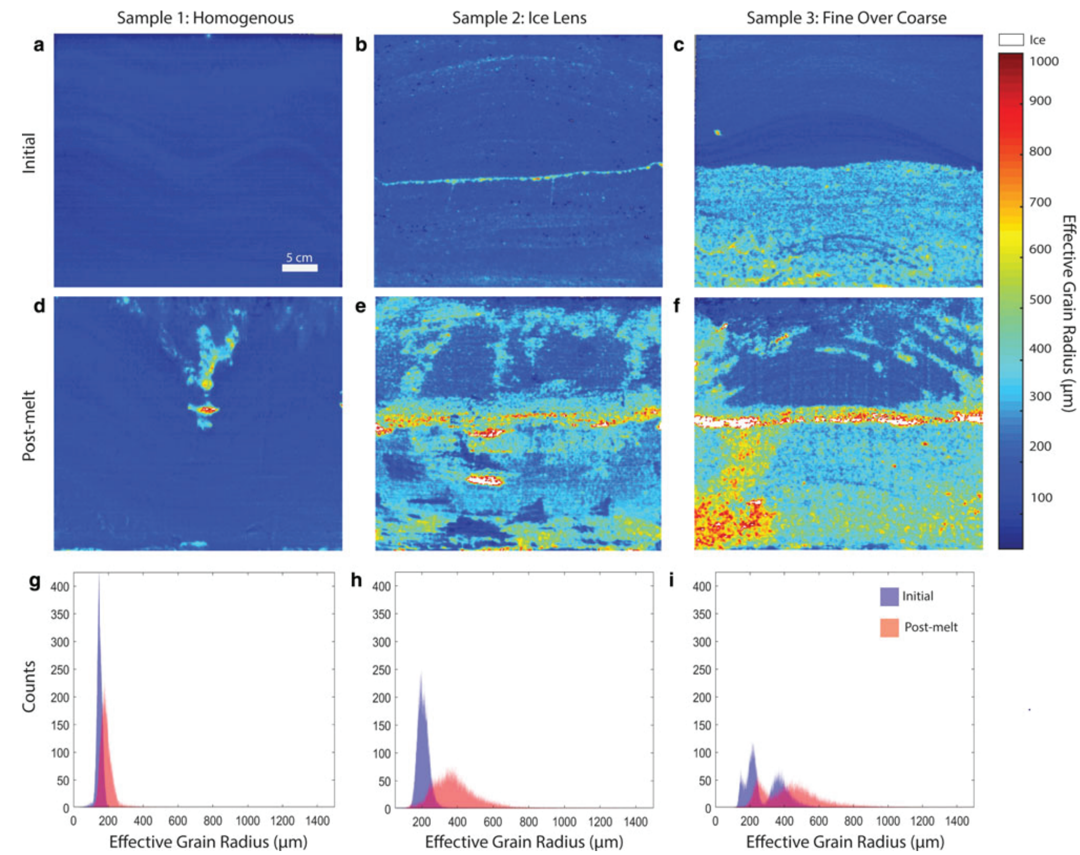

Fig. 4. (a–c) Effective grain radius (r_e) map for three laboratory-prepared snow samples; (a) homogeneous, (b) ice lens, (c) fine grains over coarse grains. (d–f) Post-melt r_e map for the three initial snow samples shown in (a–c). (g–i) Distribution of r_e for each snow sample initially, and post-melt.

between fine and coarse r_e, referred to as a capillary barrier (Waldner and others, 2004), can be seen by the formation of an ice layer surrounded by larger grains. Capillary barriers in a snowpack are generally due to infiltrating water in finer grains having a very high suction, which prevents water from entering the lower (coarse grain) layer, causing local accumulation of water at the interface (ponding) and horizontal diversion of water (Yamaguchi and others, 2010; Avanzi and others, 2016).

As mentioned in Section 2.3, it should be noted that in all the hyperspectral images presented here, the snow samples had been refrozen at −30°C, such that there was no liquid water present (i.e. dry snow) during the data collection. This is important to reiterate because the presence of liquid water in snow does affect the ice absorption feature centered at 1030 nm due to the two absorption features associated with liquid water at 950 and 1150 nm (Nolin and Dozier, 2000). Furthermore, Green and Dozier (1996) demonstrated that high amounts of liquid water (25% by volume) shifted the ice absorption feature to shorter wavelengths and reduced the depth. However, Nolin and Dozier (2000) reported that for low amounts of liquid water (3–5% by volume), there were no effects on the accuracy of the r_e retrievals using the scaled band area (N-D) method.

3.2 Instrument comparison

The retrieved r_e from each instrument is shown in a box plot analysis in Figure 5a. The mean r_e, std dev. (σ), and number of samples (n) for the hyperspectral imager, field spectrometer and micro-CT, respectively, were: $r_e = 151\ \mu m$, $(\sigma) = 20\ \mu m$, $(n) = 54\ 570$; $r_e = 151\ \mu m$, $\sigma = 7\ \mu m$, $n = 30$; $r_e = 192 \pm 2\ \mu m$, $\sigma = 12\ \mu m$ and $n = 5$. The mean r_e value from the field spectrometer matched that of the hyperspectral imager, although the median value was 4% higher. Additionally, the full range of spectrometer r_e values generally aligned with the interquartile range of the hyperspectral imager, but the full range was not represented in the distribution. The retrieved r_e from the micro-CT fell within the upper range of r_e values from the hyperspectral imager, but the mean r_e was 23.9% higher.

The map of r_e retrievals from all three instruments is shown in Figure 5b. Although this snow sample was prepared to be homogeneous, the r_e map revealed slightly larger grains at the top and bottom of the snow sample. This spatial variability was not seen in field spectrometer retrievals; however, it is important to note that the spot size (~5.6 mm) only spans a few pixels (~3 mm) and the circles representing these measurements were only enlarged for better visualization in the figure. The micro-CT r_e measurements, which are shown approximately to scale, were higher relative to the other methods. The general trend, however, was captured across the vertical profile, as illustrated in Figure 5b.

It was expected that the r_e retrievals between the hyperspectral imager and field spectrometer would be similar given that the N-D method was applied to both instruments. This close match in mean r_e values demonstrates that the instrument specifications of the hyperspectral imager are sufficient to retrieve an accurate r_e.

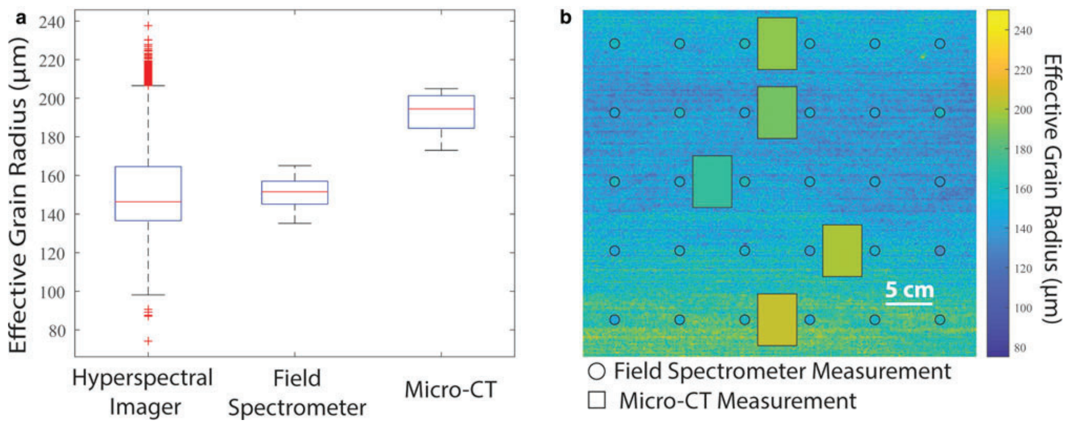

Fig. 5. Effective grain radius (r_e) retrieval comparison between the hyperspectral imager, field spectrometer and micro-CT using a homogeneous snow sample. (a) Box plot showing the median, range and distribution of r_e from each instrument. (b) Map of r_e retrieved from the hyperspectral imager overlaid with field spectrometer and micro-CT measurements. The circles representing the field spectrometer have been enlarged for better visualization.

Provided that the field spectrometer has a significantly higher spectral resolution, broader range and better SNR than the hyperspectral imager, this is an encouraging result. The spatial variability in r_e values between the two instruments (Fig. 5b) is primarily attributed to the comparison design (i.e. fewer number of spectrometer measurements and difference in field of view), but also demonstrates the value of using a mapping technique for a more complete characterization of the r_e range and spatial variability, as evidenced in Figure 5 for the hyperspectral imager.

The discrepancy in values between the hyperspectral imager and micro-CT could be attributed to multiple factors. First, there is a fundamental difference in measurement methods. The micro-CT measures the actual snow grain surface area and volume, which is converted to r_e using the relationship in Eqn (1). Whereas the hyperspectral imager and field spectrometer are optically based methods that use a radiative transfer inversion technique based on snow grains modeled as spheres. It has been demonstrated that SSA from optical methods could have uncertainties by not accounting for grain shape (Picard and others, 2009). Additionally, there are two experimental factors that could have contributed to the discrepancy in r_e values; (1) the micro-CT measures a volume that extends 33 mm into the snow sample sidewall, whereas the hyperspectral imager and field spectrometer measure r_e only at the snow surface, due to the shallow penetration of light in the NIR wavelengths, and (2) the five micro-CT scans spanned ~3 h post reflectance measurements, during which some change in the grain morphology may have occurred. These results are similar to reported values in Gergely and others (2014), where r_e values retrieved from NIR reflectance measurements using the Infrasnow instrument were within 25% of micro-CT measurements. Although Nolin and Dozier (2000) report a much better agreement ($r = 0.997$) between retrieved r_e and measured r_e, we cannot compare these micro-CT results to those because they do not specify which of their measured grain radii are from stereology versus hand lens.

3.3 Sensitivity to illumination angle

The primary goal of the illumination sensitivity experiment was to assess how deviations in the light source illumination angle from nadir (0°) could impact the NIR-HSI method r_e retrieval. As noted in Section 2.4.2, images were progressively collected across increasing illumination angles, and 0° was treated as the baseline against which all other retrievals were compared. The baseline image mean r_e was 120 μm (red line in Fig. 6). When the 0° lookup table was used at all other angles the retrieved r_e decreased relative to the baseline image, from 119 μm at 5° to 83 μm at 45°, with the decrease being relatively proportional to the cosine of the illumination angle (Fig. 6, squares and dashed blue line). For the r_e retrievals presented in Section 3.1, we assumed the halogen light source was at a 0° ± 5° and processed images with a 0° illumination angle lookup table. The deviation of mean r_e values was <1% between 0° and 5°, indicating that slight deviations from 0° do not significantly impact the r_e retrieval, but that larger deviations would introduce a bias toward smaller r_e (Fig. 6).

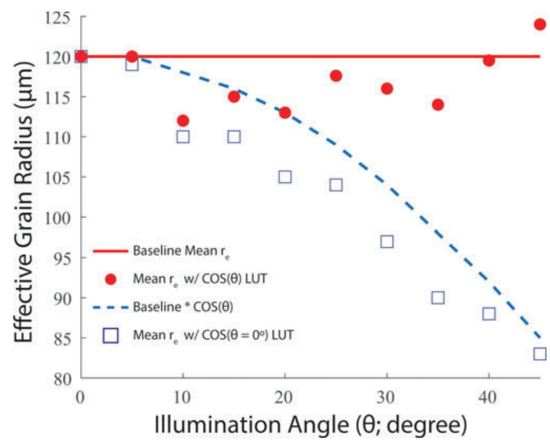

Fig. 6. Sensitivity of illumination angle to the effective grain radius (r_e) retrieval method. Retrieved mean r_e using the lookup table generated for nadir illumination ($\theta = 0°$) is plotted as a function of illumination angle as blue squares. The decrease is relatively proportional to the baseline r_e multiplied by the cosine of the illumination angle (dashed blue line). Mean r_e retrievals using a lookup table generated with the correct illumination angle are plotted as red circles and compared to the baseline mean r_e from nadir illumination (red line).

On the other hand, comparable mean r_e values to the baseline image were retrieved across all illumination angles included in the experiment when individual lookup tables were generated for each respective illumination angle tested (Fig. 6, circles). The difference

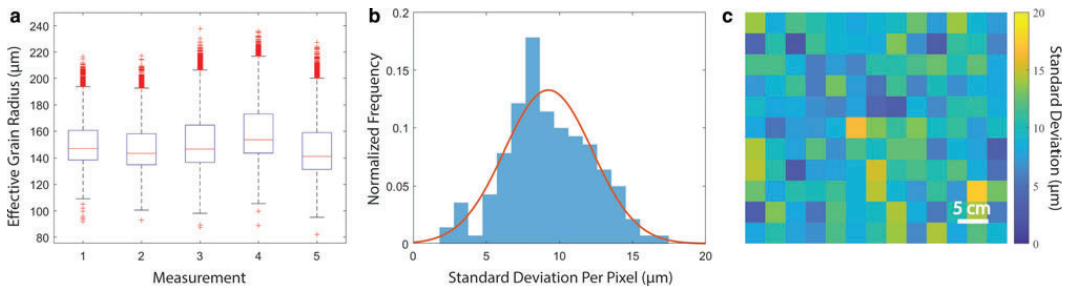

Fig. 7. Hyperspectral imager repeatability results to assess sensitivity to sensor noise. (a) Box plot analysis of five consecutively obtained images. (b) Histogram of the per pixel (3.5 cm^2 subregion) std dev. of mean effective grain radius (r_e) from the snow sample sidewall imaged, (c) map of r_e standard deviations across the snow sample sidewall subregions.

between mean r_e at increasing illumination angles, relative to the baseline image, was 0 µm at 5° and then ranged from −8 µm at 10° to + 4 at 45°. Although the error between these results and the baseline data are within the repeatability range of this method, discussed further in Section 3.4, having an off-nadir illumination angle introduces angular uncertainties into the retrieval.

In the NIR wavelengths, snow reflectance is anisotropic, preferentially scattering light in the forward direction (Warren, 1982). This can impact the accuracy of retrieving r_e from measured directional reflectance (Painter and Dozier, 2004*a*, 2004*b*). When the illumination angle is nadir, however, snow reflectance is essentially Lambertian (Dumont and others, 2010). In our experimental setup, the uncertainty due to angular effects was minimized by keeping the view and illumination angles nadir. If both the view and illumination angles were off-nadir, using a radiative transfer model that computes angular intensities, like DISORT, would be recommended.

Lastly, we recognize that the lights used in these experiments introduce some level of uncertainty, even if minor, because the illumination may vary slightly between images. The method could be improved by modifying the light source to minimize slight variations in illumination angle. For example, lights could be fully diffused and/or co-aligned with the imager and evenly spaced around the lens. This would allow the lights to rotate with the imager, resulting in a better quasi-monostatic measurement.

3.4 Repeatability

The box plot analysis, shown in Figure 7a, shows that the general distribution of r_e values is similar across all five consecutive images used to test repeatability. The interquartile range for each image spans ∼20–30 µm, while the full range is ∼110–220 µm. The mean r_e ranged from 147 to 161 µm across the five images and was 151 µm for all images with a std dev. of 5 µm. Among all images, image 4 stands out as having a slight shift to higher values.

To assess the spatial variability across repeated images, the std dev. of the mean r_e was calculated in 3.5 cm^2 subregions (20 × 20 pixels). The distribution of std dev. is shown in Figure 7b and a map of std dev. corresponding to the snow sample sidewall is shown in Figure 7c. The std dev. are randomly distributed across the image, indicating that the repeatability is most likely due to sensor noise, which can be approximated as Gaussian (Fig. 7b). The mean std dev. across subregions was 9 µm, which we use as the repeatability of the instrument. This repeatability is lower than the error due to sensor noise from AVIRIS bands (±10–50 µm) reported by Nolin and Dozier (2000), which can be attributed to the Resonon imager having more spectral bands across the ice absorption feature and a higher SNR.

4. Conclusion and future applications

We presented a new high spatial resolution NIR-HSI method to map r_e from spectral reflectance data measured with a Resonon Pika NIR-320 compact hyperspectral imager. To demonstrate the effectiveness of the method over a wide range of r_e, the method was applied to laboratory-prepared snow samples that had undergone wet snow metamorphism induced by a simulated solar lamp. Our results demonstrate that the NIR-HSI method can be a valuable tool for (1) quantifying spatial and temporal variability in r_e, (2) measuring change in grain size, (3) investigating wet snow metamorphism under refrozen conditions and (4) visualizing liquid water flow in a refrozen snowpack.

Additionally, the NIR-HSI method was compared to r_e retrievals from a field spectrometer and micro-CT. It was found that the hyperspectral imager r_e retrieval compared well to the higher spectral resolution field spectrometer but was better able to capture spatial variability due to the extensive number of data points produced from the mapping technique. Although it was found that micro-CT mean r_e values were 23.9% higher than that of the hyperspectral imager, the vertical profile followed the same spatial trend seen in the r_e map produced by the NIR-HSI method.

This robust high-resolution mapping method fills a gap in current r_e retrievals. There is increasing commercial availability of compact hyperspectral imagers, at feasible size and weight for laboratory and field applications, which will make this method more accessible. Although outside the scope of this paper, this method could be extended into the field to map r_e in an excavated snow pit or at the surface when mounted on an unmanned aerial vehicle. For field applications, careful consideration of illumination conditions would be important for accurate r_e retrievals. Mapping r_e at the snow surface would require lookup tables to be generated for the solar zenith angle at the time of measurement. In a snow pit, mapping r_e becomes more challenging because the direct and diffuse light ratio is unknown and would require some approximations to be made when generating the lookup table.

Supplementary material. The supplementary material for this article can be found at https://doi.org/10.1017/jog.2020.68

Acknowledgements. This research was supported by the NASA New Investigator Program Award 80NSSC18K0822. Additionally, Skiles was supported by the University of Utah GCSC, SWC, and Nexus. We acknowledge Resonon Inc. for supplying the hyperspectral imager used in this study. We also thank James Dillon and Ladean McKittrick for their assistance in the laboratory. We also acknowledge the use of the Subzero Research Laboratory in the Department of Civil Engineering at Montana State University. We thank Ghislain Picard and Henning Löwe for providing insightful comments that helped improve this manuscript. The presented data are available upon request from the lead author.

References

Arnaud L and 7 others (2011) Measurement of vertical profiles of snow specific surface area with a 1 cm resolution using infrared reflectance: instrument description and validation. *Journal of Glaciology* **57**(201), 17–29.

Avanzi F, Hirashima H, Yamaguchi S, Katsushima T and Michele CD (2016) Observations of capillary barriers and preferential flow in layered snow during cold laboratory experiments. *The Cryosphere* **10**(5), 2013–2026.

Avanzi F, Petrucci G, Matzl M, Schneebeli M and De Michele C (2017) Early formation of preferential flow in a homogeneous snowpack observed by micro-CT. *Water Resources Research* **53**(5), 3713–3729.

Bohren CF and Beschta RL (1979) Snowpack albedo and snow density. *Cold Regions Science and Technology* **1**(1), 47–50.

Brucker L and 7 others (2011) Modeling time series of microwave brightness temperature at Dome C, Antarctica, using vertically resolved snow temperature and microstructure measurements. *Journal of Glaciology* **57**(201), 171–182.

Colbeck SC (1991) The layered character of snow covers. *Reviews of Geophysics* **29**(1), 81–96.

Dumont M (2010) High-accuracy measurements of snow bidirectional reflectance distribution function at visible and NIR wavelengths-comparison with modelling results. *Atmospheric Chemistry and Physics, European Geosciences Union* **10**(5), 2507–2520.

Fierz C (2009) *The international classification for seasonal snow on the ground. International Association of Cryospheric Sciences*. IHP-VII Technical Documents in Hydrology N°83, IACS Contribution N°1, Paris: UNESCO-IHP.

Flanner MG, Zender CS, Randerson JT and Rasch PJ (2007) Present-day climate forcing and response from black carbon in snow. *Journal of Geophysical Research: Atmospheres* **112**, D11.

Flin F, Brzoska J-B, Lesaffre B, Coléou C and Pieritz RA (2004) Three-dimensional geometric measurements of snow microstructural evolution under isothermal conditions. *Annals of Glaciology* **38**, 39–44.

Gallet JC, Domine F, Zender CS and Picard G (2009) Measurement of the specific surface area of snow using infrared reflectance in an integrating sphere at 1310 and 1550 nm. *The Cryosphere* **3**(2), 167–182.

Gerdel RW (1954) The transmission of water through snow. *Eos. Transactions American Geophysical Union* **35**(3), 475–485.

Gergely M, Wolfsperger F and Schneebeli M (2014) Simulation and validation of the InfraSnow: an instrument to measure snow optically equivalent grain size. *IEEE Transactions on Geoscience and Remote Sensing* **52**, 4236–4247.

Green RO and Dozier J (1996) Retrieval of surface snow grain size and melt water from AVIRIS spectra. In *Proceedings of the 6th Annual JPL Airborne Earth Science Workshop, JPL Pub*, Vol. 1, pp. 127–134.

Grenfell TC and Warren SG (1999) Representation of a nonspherical ice particle by a collection of independent spheres for scattering and absorption of radiation. *Journal of Geophysical Research: Atmospheres* **104**(D24), 31697–31709.

Hammonds K, Lieb-Lappen R, Baker I and Wang X (2015) Investigating the thermophysical properties of the ice–snow interface under a controlled temperature gradient: Part I: experiments & observations. *Cold Regions Science and Technology* **120**, 157–167.

Lorensen WE and Cline HE (1987) Marching cubes: a high resolution 3D surface construction algorithm. *ACM Siggraph Computer Graphics* **21**(4), 163–169.

Marks D and Dozier J (1992) Climate and energy exchange at the snow surface in the Alpine Region of the Sierra Nevada: 2. Snow cover energy balance. *Water Resources Research* **28**(11), 3043–3054.

Marsh P (1987) Grain growth in a wet arctic snow cover. *Cold Regions Science and Technology* **14**(1), 23–31.

Matzl M and Schneebeli M (2006) Measuring specific surface area of snow by near-infrared photography. *Journal of Glaciology* **52**(179), 558–564.

Nolin AW and Dozier J (2000) A hyperspectral method for remotely sensing the grain size of snow. *Remote Sensing of Environment* **74**(2), 207–216.

Painter TH and 5 others (2009) Retrieval of subpixel snow covered area, grain size, and albedo from MODIS. *Remote Sensing of Environment* **113**(4), 868–879.

Painter TH, Bryant AC and Skiles SM (2012) Radiative forcing by light absorbing impurities in snow from MODIS surface reflectance data. *Geophysical Research Letters* **39**(17), 1–7.

Painter TH and Dozier J (2004*a*) The effect of anisotropic reflectance on imaging spectroscopy of snow properties. *Remote Sensing of Environment* **89**(4), 409–422.

Painter TH and Dozier J (2004*b*) Measurements of the hemispherical-directional reflectance of snow at fine spectral and angular resolution. *Journal of Geophysical Research: Atmospheres* **109**(D18), 1–21.

Painter TH, Molotch NP, Cassidy M, Flanner M and Steffen K (2007) Contact spectroscopy for determination of stratigraphy of snow optical grain size. *Journal of Glaciology* **53**(180), 121–127.

Picard G, Arnaud L, Domine F and Fily M (2009) Determining snow specific surface area from near-infrared reflectance measurements: numerical study of the influence of grain shape. *Cold Regions Science and Technology* **56**(1), 10–17.

Pielmeier C and Schneebeli M (2003) Developments in the stratigraphy of snow. *Surveys in Geophysics* **24**(5), 389–416.

Raymond CF and Tusima K (1979) Grain coarsening of water-saturated snow. *Journal of Glaciology* **22**(86), 83–105.

Schneebeli M (1995) Development and stability of preferential flow paths in a layered snowpack. *IAHS Publications-Series of Proceedings and Reports-International Association of Hydrological Sciences* **228**, 89–96.

Schneebeli M and Sokratov SA (2004) Tomography of temperature gradient metamorphism of snow and associated changes in heat conductivity. *Hydrological Processes* **18**(18), 3655–3665.

Seidel FC, Rittger K, Skiles SM, Molotch NP and Painter TH (2016) Case study of spatial and temporal variability of snow cover, grain size, albedo and radiative forcing in the Sierra Nevada and Rocky Mountain snowpack derived from imaging spectroscopy. *The Cryosphere* **10**(3), 1229–1244.

Stamnes K, Tsay S-C, Wiscombe W and Jayaweera K (1988) Numerically stable algorithm for discrete-ordinate-method radiative transfer in multiple scattering and emitting layered media. *Applied Optics* **27**(12), 2502–2509.

Waldner PA, Schneebeli M, Schultze-Zimmermann U and Flühler H (2004) Effect of snow structure on water flow and solute transport. *Hydrological Processes* **18**(7), 1271–1290.

Warren SG (1982) Optical properties of snow. *Reviews of Geophysics* **20**(1), 67–89.

Warren SG and Brandt RE (2008) Optical constants of ice from the ultraviolet to the microwave: a revised compilation. *Journal of Geophysical Research: Atmospheres* **113**, D14.

Wiscombe WJ and Warren SG (1980) A model for the spectral albedo of snow. I: Pure snow. *Journal of the Atmospheric Sciences* **37**(12), 2712–2733.

Yamaguchi S, Katsushima T, Sato A and Kumakura T (2010) Water retention curve of snow with different grain sizes. *Cold Regions Science and Technology* **64**(2), 87–93.

Zuanon N and A2 Photonic Sensors (2013) IceCube, a portable and reliable instrument for snow specific surface area measurement in the field. *International Snow Science Workshop*, Grenoble – Chamonix Mont-Blanc.

CHAPTER THREE

MAPPING LIQUID WATER CONTENT IN SNOW AT THE MILLIMETER SCALE: AN INTERCOMPARISON OF MIXED-PHASE OPTICAL PROPERTY MODELS USING HYPERSPECTRAL IMAGING AND IN SITU MEASUREMENTS

Manuscript in Chapter 3

Author: Christopher Donahue

Contributions: Conceptualized the study, collected laboratory and field data, performed radiative transfer simulations using DISORT, processed all data, analyzed the results, wrote the original draft manuscript, created visualizations, and handled the response to peer-reviews.

Co-Author: S. McKenzie Skiles

Contributions: Advised CD during study conceptualization and DISORT modeling, assisted during data collection, and reviewed and edited the original draft manuscript.

Co-Author: Kevin Hammonds

Contributions: Acquired funding for this research, was responsible for project administration, supervised CD throughout the study, and reviewed and edited the original draft manuscript.

Manuscript Information

Christopher Donahue, S. McKenzie Skiles, and Kevin Hammonds
The Cryosphere
Status of Manuscript:
____ Prepared for submission to a peer-reviewed journal
____ Officially submitted to a peer-reviewed journal
____ Accepted by a peer-reviewed journal
__x__ Published in a peer-reviewed journal

Copernicus Publications
Submitted: 10 August 2021
Accepted: 30 November 2021
Published in Print: 6 January 2022
Volume 16, Issue 1, Pages 43-59
https://doi.org/10.5194/tc-16-43-2022

The Cryosphere, 16, 43–59, 2022
https://doi.org/10.5194/tc-16-43-2022

The Cryosphere
Open Access

Mapping liquid water content in snow at the millimeter scale: an intercomparison of mixed-phase optical property models using hyperspectral imaging and in situ measurements

Christopher Donahue[1], **S. McKenzie Skiles**[2], **and Kevin Hammonds**[1]

[1]Department of Civil Engineering, Montana State University, Bozeman, MT 59717, USA
[2]Department of Geography, University of Utah, Salt Lake City, UT 84112, USA

Correspondence: Christopher Donahue (christopher.donahue2@student.montana.edu)

Received: 10 August 2021 – Discussion started: 12 August 2021
Revised: 9 November 2021 – Accepted: 30 November 2021 – Published: 6 January 2022

Abstract. It is well understood that the distribution and quantity of liquid water in snow is relevant for snow hydrology and avalanche forecasting, yet detecting and quantifying liquid water in snow remains a challenge from the micro- to the macro-scale. Using near-infrared (NIR) spectral reflectance measurements, previous case studies have demonstrated the capability to retrieve surface liquid water content (LWC) of wet snow by leveraging shifts in the complex refractive index between ice and water. However, different models to represent mixed-phase optical properties have been proposed, including (1) internally mixed ice and water spheres, (2) internally mixed water-coated ice spheres, and (3) externally mixed interstitial ice and water spheres. Here, from within a controlled laboratory environment, we determined the optimal mixed-phase optical property model for simulating wet snow reflectance using a combination of NIR hyperspectral imaging, radiative transfer simulations (Discrete Ordinate Radiative Transfer model, DISORT), and an independent dielectric LWC measurement (SLF Snow Sensor). Maps of LWC were produced by finding the lowest residual between measured reflectance and simulated reflectance in spectral libraries, generated for each model with varying LWC and grain size, and assessed against the in situ LWC sensor. Our results show that the externally mixed model performed the best, retrieving LWC with an uncertainty of $\sim 1\,\%$, while the simultaneously retrieved grain size better represented wet snow relative to the established scaled band area method. Furthermore, the LWC retrieval method was demonstrated in the field by imaging a snowpit sidewall during melt conditions and mapping LWC distribution in unprecedented detail, allowing for visualization of pooling water and flow features.

1 Introduction

The distribution and quantity of liquid water within a snowpack, introduced by rain and/or melt, are relevant for multiple snow-related applications including snow hydrology, remote sensing, and avalanche forecasting. In terms of snow hydrology, water is an indicator of snow energy balance and snowmelt timing; the change in phase from ice to water indicates that the cold content of the snowpack is depleted and that energy balance inputs are contributing to melt (DeWalle and Rango, 2008). Rain on snow can accelerate this process by contributing large energy inputs into the snowpack over a short amount of time (Mazurkiewicz et al., 2008). Water at the surface will also lower snow albedo, initiating a positive feedback loop that increases absorbed solar radiation, the main driver of snowmelt (Gupta et al., 2005). For active and passive microwave remote sensing of snow, the presence of water alters microwave signatures because of the large difference in relative permittivity between liquid water and ice (i.e., dry snow). For active microwave sensors, wet snow causes characteristic changes in microwave backscatter and reduces penetration depth (Shi and Dozier, 1992), while for passive sensors, the emissivity of the snow surface is increased (Walker and Goodison, 1993). For avalanche forecasting, the infiltration of liquid water into the snowpack impacts snow stability (Conway and Raymond, 1993). The strength of the snowpack can be increased at lower water content, where grains form well-bonded clusters, but reduced at higher water content, when water flow through pore space deteriorates a significant number of snow grain bonds, resulting in relatively cohesionless particles (Colbeck, 1982). Although it is recognized as a critical snow property across the cryospheric sciences, liquid water content (LWC) measurements in a snowpack are notoriously difficult to accurately quantify due to the high spatial and temporal variability in liquid water distribution.

Here, the utility of mapping LWC in situ using near-infrared hyperspectral imaging (NIR-HSI) and radiative transfer model inversion is assessed. This approach leverages the segments of the near-infrared (NIR) spectrum where the optical properties of liquid water, hereafter referred to as water, vary from those of ice. To date, wet snow has been modeled using effective spheres with a known radius, referred to as the effective grain radius (r_e), where the optical properties of ice and water are mixed either internally or externally. In wet snow, the arrangement of water relative to ice particles and pore space varies based on the level of saturation, which may be relevant for radiative transfer modeling. For example, water saturation below 7 % (pendular regime), when water is contained in menisci held in between the ice particles (Colbeck, 1979), might be best represented using an internally mixed particle model where an ice sphere is coated in water. On the other hand, water saturation above 7 % (funicular regime), when ice particles become surrounded by water as it fills the pore space, might be best represented as an internally mixed-phase sphere or externally mixed interstitial ice and water spheres.

Although different mixing model representations have been proposed and demonstrated (Green et al., 2002; Hyvarinen and Lammasniemi, 1987), no study has quantitatively compared the different approaches or compared LWC retrievals to established LWC measurement methods. Without intercomparing or validation, the best approach for retrieving LWC from NIR spectral reflectance has yet to be determined. Additionally, radiative transfer approaches to retrieving r_e are based on the optical properties of ice and implicitly assume dry snow, and such retrievals have not been assessed for wet snow. The main objectives of this study are threefold: (1) intercompare three wet snow reflectance models against measured LWC from a dielectric measurement instrument in a controlled laboratory environment, (2) simultaneously assess effective grain size retrieval methods and their suitability for use with wet snow, and (3) demonstrate the capability of a compact NIR hyperspectral imager to simultaneously map LWC and snow grain size at the laboratory and field scales.

2 Background

2.1 Liquid water in snow

Water infiltration through snow is a spatially and temporally complex process, controlled by water saturation level, snow microstructure, and topography. Generally, water infiltration is described by two primary mechanisms: homogenous matrix flow and heterogeneous preferential flow. Matrix flow is described as the semi-uniform vertical movement of water, while preferential flow is made up of concentrated water pathways that follow the path of least resistance that can extend deep into the snowpack, ahead of the matrix flow (Schneebeli, 1995). Although gravitational forces primarily drive vertical movement of water in snow, large amounts of water can be diverted horizontally due to stratigraphic layers in the snowpack, such as ice crusts or capillary barriers (i.e., fine grains over coarse grains) (Waldner et al., 2004; Webb et al., 2021; Eiriksson et al., 2013). As the snowpack becomes less stratified throughout the melt season, the general pattern transforms from preferential flow to homogenous flow (Webb et al., 2018).

2.2 Measurement of liquid water in snow

The complexity of water movement through snow makes observations and measurements challenging. Early observations of water flow patterns through snow were made using dye tracers (Seligman et al., 1936; Gerdel, 1954), a method which is still used today. Dye tracers provide a spatial visualization of water infiltration that has been used to study processes such as preferential flow (Schneebeli, 1995; Waldner et al., 2004) and capillary barriers (Avanzi et al., 2016). While these methods remain primarily a qualitative visualization technique, Williams et al. (2010) quantified the three-dimensional (3D) spatial distribution of meltwater within a 1 m^3 snowpack using dye tracers and serial-section imaging. The 3D data were binarized into dry and wet categories to quantify flow features at the centimeter scale, but LWC is not obtainable using this method.

In situ measurements of LWC in snow have traditionally been measured by centrifugal separation (Kuroda and Hurukawa, 1954), melting calorimetry (Yosida, 1940), freezing calorimetry (Jones et al., 1983), and the dilution method (Davis et al., 1993). A more detailed summary of these methods can be found in Stein et al. (1997). Generally, these methods are difficult to perform and time-consuming and have only been occasionally used since their introduction. More commonly, LWC is measured using dielectric methods at frequencies ranging from 1 MHz to 1 GHz by leveraging the large differences in the relative permittivity (ε_r) between water ($\varepsilon_r \approx 88$), ice ($\varepsilon_r \approx 3.15$), and air ($\varepsilon_r \approx 1$) (Tiuri et al., 1984). This is done by time domain reflectometry (TDR) or with capacitance sensors which measure the relative permittivity of snow (Lundberg, 1997; Denoth et al., 1984). Although the measured relative permittivity is primarily a function of LWC, snow density also has some influence. Therefore, dielectric methods also require a separate density measurement. Examples of currently available dielectric instruments include the snow fork (Sihvola and Tiuri, 1986); Denoth meter (Denoth, 1994); A2 Photonic WISe sensor (A2 Photonic Sensors, 2019); and the SLF Snow Sensor (FPGA Company, 2018), which was used in this study. Although these instruments make measurements quicker relative to traditional methods, they often require destructive sampling and only provide a discrete volume-averaged point measurement. Therefore, there is currently no in situ method to effectively quantify spatial variability in LWC at a high (sub-centimeter) spatial resolution, which could be used, for example, to validate process-based modeling of wet snow (Hirashima et al., 2019) or initialization and validation of microwave radiative transfer models (e.g., Wiesmann and Mätzler, 1999; Picard et al., 2013).

Previous non-destructive measurements of LWC in snow have been made using remote sensing techniques. Like dielectric sensors, active and passive microwave sensors leverage the difference in relative permittivity between water, ice, and air. At the ground-based scale, upward-looking ground-penetrating radar (upGPR) has been used to measure the volumetric LWC directly above antennas buried below a snowpack (Schmid et al., 2014). At the spaceborne scale, active and passive microwave sensors have been used to make classification maps of wet or dry snow at spatial resolutions on the order of tens of meters (e.g., Lund et al., 2020; Walker and Goodison, 1993). Similarly, in the optical wavelengths, the shift in absorption patterns of ice and water across the NIR have been leveraged to map surface LWC (Green et al., 2002), which is the primary method of interest in this work.

2.3 Modeling wet snow near-infrared reflectance

Absorption in the optical wavelengths is described by the imaginary part of the complex refractive index. Although the absorption patterns across the NIR are similar between ice and water, there are shifts that distinguish the different phases. The spectral complex refractive index for ice (Warren and Brandt, 2008) and water at 0 °C (Rowe et al., 2020) across NIR wavelengths is shown in Fig. 1. Compared to the difference in the relative dielectric properties across the radio and microwave wavelengths, the shifts in the imaginary part of the complex refractive index are relatively minor and therefore require measured reflectance at multiple wavelengths and radiative transfer modeling to detect. Additionally, the penetration of light in the NIR wavelengths is relatively shallow, limiting detection of water to the snow surface (∼ 2 cm). This has limited the use of optical methods to detecting surface water using either in situ spectrometer measurements or airborne imaging spectrometer measurements (Green et al., 2002; Hyvarinen and Lammasniemi, 1987).

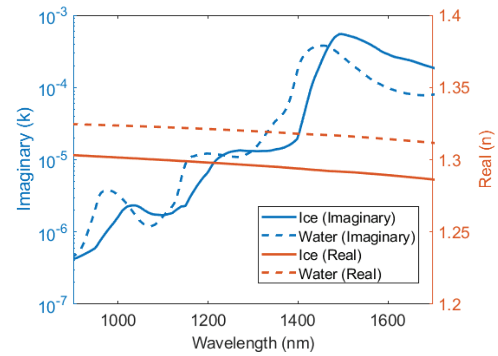

Figure 1. Complex refractive index of ice and liquid water at 0 °C across the near-infrared region ranging from 900–1700 nm, which is the same range measured by the Resonon Pika NIR-320 hyperspectral imager.

Inversion of radiative transfer models is commonly used in remote sensing applications to retrieve physical snow properties from measured spectra, and many modeling approaches have been proposed. Hyvarinen and Lammasniemi (1987) modeled the reflectance of wet snow using a collection of spheres with radius r_e to simultaneously estimate LWC and grain size. To describe the optical properties of the effective spheres, an effective complex refractive index (k_{eff}) was calculated by volume-mixing the complex refractive index of ice and water. Using a forward-modeling approach, LWC and r_e were retrieved using only three bands (1030, 1260, and 1370 nm), which were assessed using a dilatometer in a laboratory. Alternatively, Green et al. (2002) modeled wet snow using two approaches: (1) as a collection of water-coated ice spheres and (2) water spheres interspersed in the interstitial space within an ice-sphere matrix. LWC and r_e were retrieved by matching the simulated spectra to measured spectra by finding the lowest residual. By visual inspection, Green et al. (2002) concluded that wet snow is best modeled as water-coated ice spheres, though no quantitative retrieval assessment was performed. More recently, a three-band ratio method to classify wet or dry snow was proposed by Shekhar et al. (2019), based on a correlation between field spectrometer measurements and snow fork LWC measurements, although snow grain size was not considered.

To date, three radiative transfer approaches for simulating the reflectance of wet snow have been proposed: (1) mixed-phase spheres, hereafter referred to as "k_{eff} spheres"; (2) water-coated ice spheres, hereafter referred to as "coated spheres"; and (3) externally mixed interstitial ice and water spheres, hereafter referred to as "interstitial spheres". A schematic of each model is presented in Fig. 2. The k_{eff} sphere and coated sphere models are referred to as internally mixed particles because the optical properties are mixed inside of a single particle having a single r_e. The interstitial sphere model is referred to as an external mixture

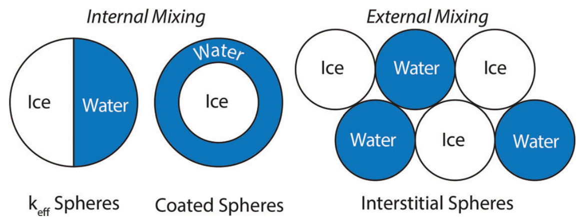

Figure 2. A schematic of three ice and water optical mixing models used to simulate the reflectance of wet snow.

because the components are assumed to be physically separate from one another.

3 Methodology

Three optical property mixing models were used to simulate the bidirectional reflectance of wet snow across a range of r_e and LWC using radiative transfer modeling. To determine the optimal mixing model for retrieving LWC from NIR reflectance, snow samples were prepared in a controlled laboratory environment with varying grain type, grain size, and density and then subjected to warm air advection to induce melt. During melt, time series NIR-HSI measurements were taken, and LWC was retrieved in each pixel by best matching the measured spectra to the simulated spectra from each of the three models. For comparison to the NIR-HSI LWC retrievals, time series LWC measurements were taken with the SLF Snow Sensor, a dielectric measurement instrument, and compared to the average LWC from pixels covering the same measurement area as the SLF Snow Sensor such that the two measurements would be comparable on the same spatial scale. Time series measurements of r_e were retrieved simultaneously with LWC and were compared against the established scaled band area method of Nolin and Dozier (2000), which has been previously applied to the same compact hyperspectral imager used in this study to map the r_e of dry snow (Donahue et al., 2021). Lastly, retrievals were demonstrated in the field across an image of a snowpit wall, visualizing water infiltration and quantifying vertical LWC and r_e distributions. The modeling and in situ measurements are described in more detail in Sect. 3.1–3.3, and the retrieval and assessment workflow is represented in Fig. 3.

3.1 Instruments

3.1.1 Near-infrared hyperspectral imager

Snow reflectance in the NIR was mapped with a Resonon Inc. Pika NIR-320 near-infrared hyperspectral imager. A brief description of the instrument follows (for a more detailed description see Donahue et al., 2021). The imager has a spectral resolution of 4.9 nm, measuring 164 bands across the NIR region from 900–1700 nm. The imager constructs a 2D image containing the full spectrum in each pixel by collecting the image line by line, known commonly as a "push broom" or "line" scanner. Thus, to collect an image, the camera needs to be moving (translating or rotating) relative to the scene, or the scene needs to be moving relative to the imager. Here, both types of image acquisition techniques are used. In the laboratory, a linear scanning stage was used to move the sample beneath the sensor, while in the field, a rotational stage mounted on top of a tripod was used to scan the snowpit wall.

3.1.2 SLF Snow Sensor

The SLF Snow Sensor (FPGA Company, 2018), hereafter referred to as the "SLF sensor", is a capacitance sensor that is placed on the snow surface to measure the relative permittivity. This is used to determine snow density and LWC in dry snow and wet snow conditions, respectively. The factory calibration for the LWC measurement is based on an empirical equation derived from reference measurements of snow with varying wetness and density using the dilution method (Davis et al., 1985) and weighted volumes. The sensor measures a snow surface area of 45×95 mm, and the penetration of the electric field into the snow is ~ 17 mm. The SLF sensor produces a spatially comparable measurement to the retrieved LWC from the NIR-HSI method presented here because the penetration of NIR light into snow is similarly shallow. Additionally, time series LWC measurements over the same surface area can be made because the sensor is nondestructive to the snow surface.

3.2 Experimental setup

3.2.1 Laboratory

The hyperspectral imager was mounted onto the Resonon benchtop linear scanning stage, which positions the imager on a stationary tower above a linear translating stage where samples are placed (shown in Fig. 4a). The lens of the imager is surrounded by four halogen lamps, and both are positioned for nadir viewing and illumination. The halogen lamps and lens of the imager were at a height of 38 and 47 cm above the snow surface, respectively. This quasi-monostatic configuration results in a bidirectional reflectance measurement in each pixel of the image when calibrated using a white reference panel. A large Spectralon ® 99 % reflectance panel was placed at the same height as the surface of the snow samples and filled the imager's entire field of view, such that each snow sample was calibrated from radiance to reflectance on a pixel-by-pixel basis. This method of calibration is ideal for hyperspectral imaging because it minimizes effects to illumination imperfections across the scene.

Snow samples were prepared in the laboratory using laboratory-made and collected natural snow to generate a dataset with a range of grain types including precipitation

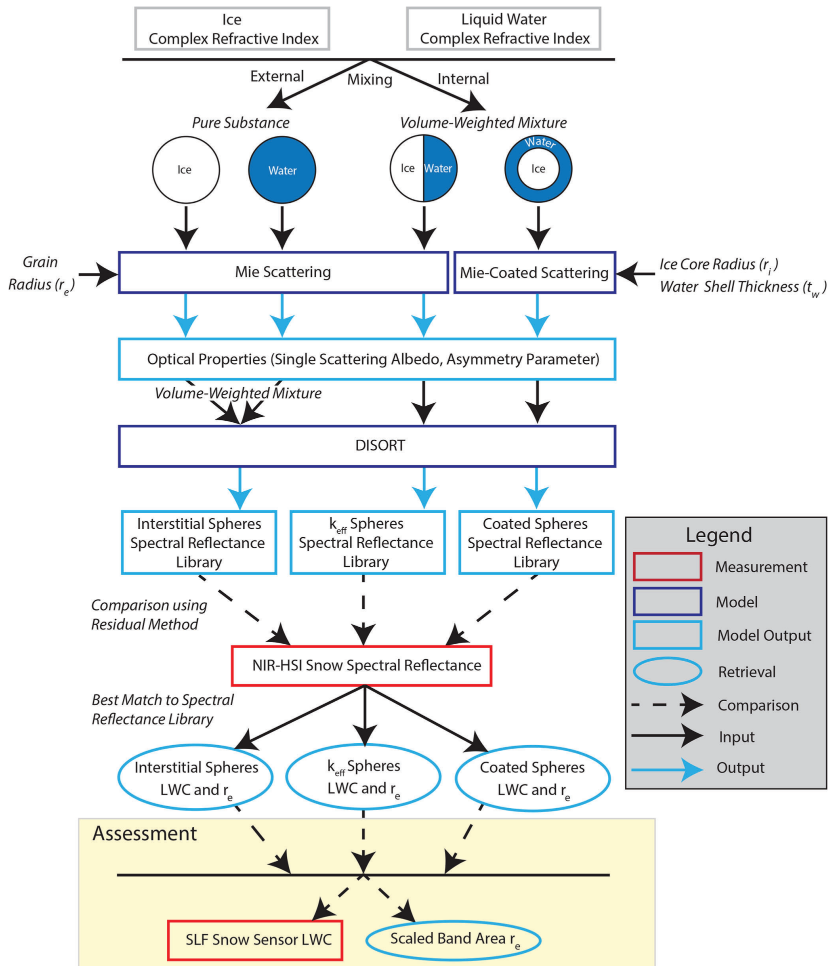

Figure 3. Liquid water content and effective grain radius retrieval and assessment workflow.

particles (PP), decomposing and fragmented precipitation particles (DF), rounded grains (RG), melt forms (MF), and faceted crystals (FC) (Fierz et al., 2009). The dry snow density, measured by weighing the sample container with a known volume and using the SLF sensor, ranged between 115 and 510 kg m^{-3}. Detailed properties for each snow sample are given in Table 1. Snow samples were made by sieving snow into a rectangular wooden sample container having dimensions of 17.1 cm × 12.4 cm × 8.5 cm ($H \times W \times D$). The wooden sample container was subdivided into three regions of interest (ROIs), each having dimensions slightly larger than the SLF sensor, such that LWC measurements would not be impacted by edge effects from the sample container. The surface of each snow sample was scraped with a crystal card to create a flat surface level with the top of the sample container and to minimize surface roughness. Snow samples were then kept in a cold room at −10 °C for 24 h to equilibrate and ensure the sample was completely dry (i.e., LWC = 0 %).

For each snow sample, an initial image was taken while the cold room was at −10 °C to obtain the dry snow condition. The dry snow surface density in each ROI was measured using the SLF sensor and used as the input dry snow density to the SLF sensor for the subsequent LWC measurements. Following dry snow measurements, the cold room was turned off, and the door was opened to ambient air, gradually increasing the air temperature in the cold room to room temperature (20 °C). The NIR-HSI images were taken every 1–3 min during the warming process, and SLF sensor measurements, in each ROI, were taken in between images. For comparison between the two instruments, the mean LWC was calculated over the 10 717 pixels within each ROI, resulting in a 0.4 mm^2 resolution, and was compared against the corresponding SLF sensor measurements at each time step, creat-

Table 1. Laboratory snow samples (reported r_e is from scaled band area method).

Sample number	Description	Sieve size (mm)	Initial r_e (µm)	Dry density (kg m^{-3})	Warming time (min)
1	PP, snowmaker snow	2	113	115	111
2	DF, snowmaker snow	2	130	212	161
3	RG, natural snow	2	176	455	118
4	MF, natural snow	5	398	440	103
5	FC, natural snow	2.5	463	493	86
6	MF, Sample 4 melt/refreeze 1×	n/a	699	468	99
7	MF, Sample 4 melt/refreeze 2×	n/a	898	510	208

n/a stands for not applicable.

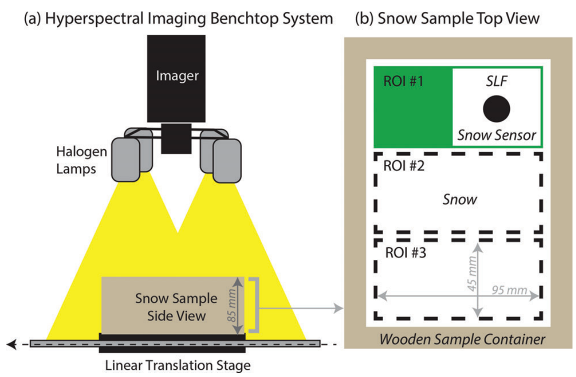

Figure 4. Schematic of laboratory setup. **(a)** Front view of the Resonon hyperspectral imaging benchtop system and wooden snow sample container. **(b)** Top view of the snow sample container showing the three regions of interest (ROIs) measured by the SLF Snow Sensor, which is shown inside of ROI no. 1.

ing a densely populated comparison dataset spanning a wide range of LWC.

3.2.2 Field

To demonstrate the applicability of the NIR-HSI method for retrieving LWC and r_e in the field, natural snow was imaged across the vertical wall of a snowpit. The snowpit was excavated to the ground within a protected study plot adjacent to the Alpine Weather Station, at Bridger Bowl Ski Area (Bozeman, MT; 45.82902° N, −110.92227° W), on 3 April 2021. The total snow depth was 150 cm, the snowpit wall was 143 cm wide, and there was approximately 2 m of working room behind the snowpit wall. The day was selected because the 2 d preceding were sunny, and diurnal temperatures did not drop below freezing, making the likelihood of imaging wet snow high. Before imaging, standard snowpit observations were collected including a temperature profile, snow density profile using a 1000 cm^3 wedge cutter, and stratigraphy with grain types.

The imager was mounted onto the Resonon outdoor field system, which includes a tripod-mounted rotational stage, and was placed 110 cm from the snowpit wall. The snowpit wall was illuminated with two 500 W halogen lamps mounted on a tripod, line-powered (120 V AC) through the weather station. The lights were placed perpendicular to the wall at a distance of 90 cm, similar to the laboratory setup presented in Donahue et al. (2021). For controlled lighting conditions, sun light (direct and diffuse) was blocked by placing an opaque tarp over the top of the snowpit. A detailed schematic of the field setup is shown in Fig. 5. For a pixel-by-pixel calibration of the NIR-HSI measurements from radiance to reflectance, a 36 % spectrally flat reflectance calibration tarp was hung in front of the snowpit wall, completely covering the field of view of the imager and ROI of the snowpit.

Images of the wall were taken at 13:00 MST, at which time there were few clouds, and the air temperature was 10 °C. Prior to imaging the snowpit sidewall, the entire face of the snowpit was cut back ∼ 10 cm to minimize impacts from exposure to ambient air temperature. The entire vertical profile of the snowpit was not captured in a single image; therefore two images were taken and stitched together capturing only the upper 110 cm of the snowpit at a 6.5 mm^2 pixel resolution. The bottom 40 cm of the snowpit was not captured because perpendicular illumination conditions could not be achieved with the minimum height of the lighting and imager tripods used.

Immediately following imaging, LWC measurements were made with the SLF sensor along a vertical profile at 5 cm increments. For optimal LWC measurements, the SLF sensor requires the dry snow density; however, the snow was already wet, and therefore the dry snow density could not be obtained. Instead, the density of the snow from the adjacent density cut measurement was used, which introduced a small error in the LWC measurement. Following the methodology proposed by FPGA Company (2018), this error was corrected by subtracting the mass of water from the wet snow density based upon the initial LWC. The updated density was used

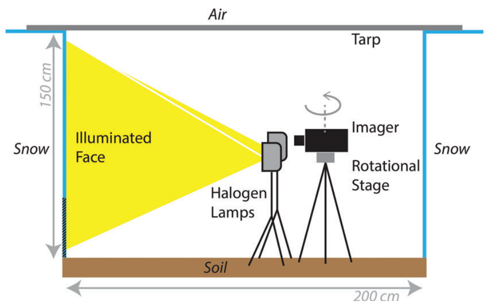

Figure 5. Schematic of the near-infrared hyperspectral imaging setup in the field for measurement of liquid water content across a snowpit wall. The area at the bottom 40 cm of the snowpit was not imaged and is shown with hatched lines.

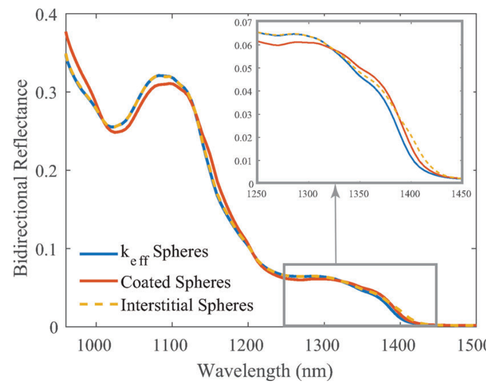

Figure 6. Simulated bidirectional reflectance of snow using three optical mixing models: (1) k_{eff} spheres, (2) coated spheres, and (3) interstitial spheres. For comparison, each mixing model has an effective grain radius of 1000 µm and 20 % liquid water content by volume.

to calculate an updated LWC using the empirical calibration equation. This calculation was repeated, with each iteration returning a smaller change in snow density. Through multiple iterations it converges on the dry snow density and corrected LWC.

3.3 Radiative transfer modeling

3.3.1 Single scattering

To simulate the optical properties of snow, the single-scattering optical properties of constituents (ice, air, water, and impurities) as well as their relative arrangement to one another must be represented. The scattering properties of a single particle are described using three dimensionless optical parameters: (1) the absorption efficiency Q_{abs}, (2) scattering efficiency Q_{sca}, and (3) asymmetry factor g (Bohren and Huffman, 2008). Dry snow particles are often assumed to scatter as a collection of ice spheres with radius r_e (e.g., Nolin and Dozier, 2000). With a known r_e and complex refractive index, Mie scattering theory (Bohren and Huffman, 2008) can be used to calculate the three dimensionless optical parameters. For clean dry snow, this modeling approach is straightforward because only the complex refractive index of ice is needed. For wet snow, on the other hand, the complex refractive index of ice and water is volume-mixed, and there are multiple approaches that can be used to define the arrangement of ice and water relative to each other. The three previously proposed mixing models used in this comparison, defined in Sect. 2, are described here.

First, the k_{eff} sphere model uses a collection of spheres with r_e and k_{eff}, which was determined using volume-weighted portions of the complex refractive index of ice (k_{ice}) and water (k_{water}).

$$k_{eff} = (1 - \%LWC) \cdot k_{ice} + \%LWC \cdot k_{water} \tag{1}$$

Second, the coated sphere model used the Miecoated scattering code of Mätzler (2002). The radius of the ice core (r_i) and thickness of the water coating (t_w) was determined by volume weights of ice (V_i) and water (V_w).

$$V_i = \frac{4}{3}\pi r_i^3 \tag{2}$$

$$V_w = \frac{\%LWC \cdot V_i}{1 - \%LWC} \tag{3}$$

$$t_w = \left[\frac{3 \cdot V_w}{4\pi + r_i}\right]^{\frac{1}{3}} - r_i \tag{4}$$

$$r_e = r_i + t_w \tag{5}$$

Lastly, the interstitial sphere model calculates the single-scattering optical properties (i.e., Q_{abs}, Q_{sca}, and g) of pure ice spheres and water spheres separately, each having the same r_e. Then, the optical properties were mixed using a volume-weighted average. This method is similar to the k_{eff} sphere model; however, the differences are a result of the non-linearity of Mie scattering theory (Lesins et al., 2002). At shorter wavelengths, the differences in reflectance are small, but at larger wavelengths a notable divergence occurs (shown in Fig. 6).

For each model clean snow is assumed, and the effects of light-absorbing particles (LAPs, i.e., dust and soot) are not considered (discussed further in Sect. 5.3.1). The single-scattering optical properties were calculated for r_e values ranging from 30–1500 µm in 10 µm intervals and 0 % to 25 % LWC in 1 % intervals, resulting in 3848 simulated combinations per model. Single-scattering optical properties for each case were then used as inputs to solve for snow reflectance, the result of multiple-scattering events.

3.3.2 Multiple scattering

To generate a spectral library to match to measured spectra, directional-hemispherical reflectance for each mixing model was simulated using a general-purpose 16-stream plane-parallel Discrete Ordinate Radiative Transfer model (DISORT; Stamnes et al., 1988). DISORT allows the user to define optical properties of multiple layers; here, a single optically thick layer was used since the penetration of NIR light into the snowpack is shallow. Optical property inputs for this layer included single-scattering albedo, defined as the ratio of the scattering efficiency and extinction efficiency $\left(\frac{Q_{\text{sca}}}{Q_{\text{sca}}+Q_{\text{abs}}}\right)$, and g, which were computed from Mie scattering theory. Incoming light can be modeled at multiple user-defined zenith angles; here, the zenith angle was set to 0° to represent nadir lighting.

The output from DISORT was directional-hemispherical reflectance, whereas NIR-HSI measurements are bidirectional reflectance. This is a suitable approach because of the experimental setup: the NIR-HSI measurements were made at nadir illumination and viewing angles and calibrated using a Lambertian white reference target. Under these conditions, snow is nearly Lambertian, allowing for a direction comparison, which would not be the case for non-nadir viewing angles, given that snow heavily favors forward scattering (Dumont et al., 2010).

3.3.3 Retrieving snow properties

To simultaneously retrieve LWC and r_e, measured spectra in each pixel of the NIR-HSI image were compared to each spectrum in the spectral library to determine the best match by finding the minimum least square residual across 106 bands, ranging from 961 to 1472 nm. Hereafter, this method for matching measured and simulated spectra is referred to as the "residual method". Examples of (1) measured spectrum from NIR-HSI, (2) retrieved simulated spectra using the interstitial sphere model, and (3) residuals across each band are shown in Fig. 7. Once the measured spectrum is best matched to a simulated spectrum, the associated r_e and LWC are assigned to the pixel, producing separate maps of r_e and LWC for the imaged area. To reduce impact from sensor noise at the lower limit of the sensor (900 nm), 961 nm was chosen as the starting point for calculating the residuals while still capturing ample spectral data for the left side of the absorption feature centered at 1030 nm (Fig. 7). At longer wavelengths, 1472 nm was chosen as the endpoint for calculating residuals because both ice and water are highly absorptive beyond this point, resulting in a low signal-to-noise ratio.

Additionally, r_e was mapped at each time step using the scaled band area method following Donahue et al. (2021). Briefly, the scaled band area is the area underneath a continuum line spanning an absorption feature and is a shape-based method that is independent of absolute reflectance. Here, the scaled band area was calculated for measured spectra using a predefined start and end point for the continuum line across the absorption feature centered at 1030 nm. The pixel-by-pixel calibration performed here reduced noise at the lower limit of the sensor compared to Donahue et al. (2021), allowing for the defined continuum endpoints to be similar to bands suggested by Nolin and Dozier (2000) (i.e., 961 and 1087 nm). A lookup table was populated with "dry snow" (all ice, no water) scaled band areas for simulated r_e ranging from 30–1500 µm. We note that we used the simulated spectra from the interstitial sphere model but that the dry snow representations for all mixing models were identical, with variation in spectra introduced only when water was represented. This allowed us to (1) define the starting r_e for each of the prepared laboratory samples (Table 1), (2) compare r_e retrieved from scaled band area to that from the residual method, and (3) assess the suitability of the scaled band area method for grain size retrievals over wet snow.

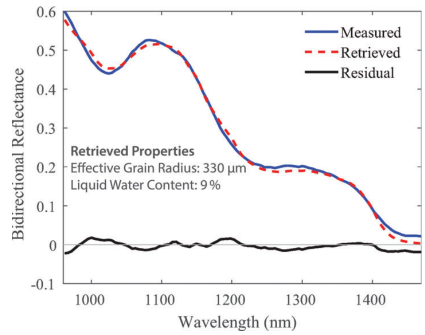

Figure 7. Example of a measured NIR-HSI spectrum, retrieved simulated spectrum using the interstitial sphere model, and the residuals at each band.

4 Results

4.1 Laboratory experiments

4.1.1 Liquid water content retrieval

The LWC retrieved from NIR-HSI was compared to the SLF sensor across seven samples, spanning a wide range of initial dry snow grain sizes from approximately 100 to 900 µm, measured using the established scaled band area method. LWC measured with the SLF sensor ranged from 0 % to 17 % across 21 ROIs and 40 time steps, producing 690 data points for comparison. It was found that the interstitial sphere model consistently performed the best, whereas the coated sphere model performed the most poorly, relative to the in situ SLF sensor measurements.

An example of the LWC maps produced as melt progressed in a single snow sample is presented in Fig. 8. These examples are of the same ROI and show LWC retrieved using the interstitial sphere model. The initial image (Fig. 8a) was taken at the start of the experiment, when the snow was dry, and 98 % of pixels (10 450 pixels) retrieved 0 % LWC. The

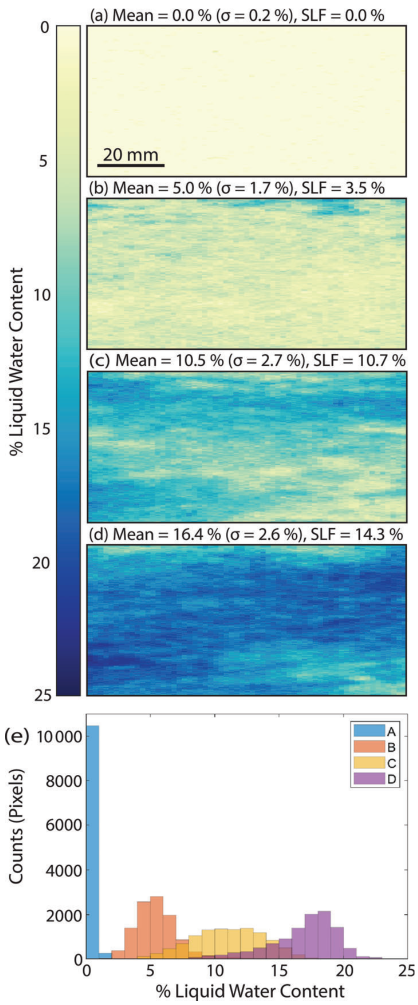

Figure 8. (a–d) Time series liquid water content mapping over a single region of interest during a laboratory experiment. **(e)** Liquid water content distribution in images **(a–d)** shown in a histogram.

other 2 % of pixels (267 pixels) retrieved 1 % LWC, which was found to be due to sensor noise. The remaining images in Fig. 8 capture melt progressing through 5 % (Fig. 8b), 10 % (Fig. 8c), and 16 % (Fig. 8d) mean LWC, and the corresponding SLF sensor measurement is noted in each panel. Additionally, the distribution of values also broadens with increasing LWC, shown in the per-pixel distribution of LWC for each image in Fig. 8e. The summary statistics show melt progression, as expected, but the maps allow visualization and quantification of melt initiation and LWC distribution. The melt features that begin to develop in early time steps can be tracked to later time steps (e.g., Fig. 8c to d).

The full performance comparison across all datasets is summarized in Fig. 9, which plots LWC from the SLF sensor against that from each mixing model applied across all samples. To help visualize the difference between experiments, the comparison points are symbolized by different colors as well as marker size that varies with the mean initial dry snow r_e retrieved using the scaled band area method. Close proximity to the 1 : 1 line would indicate the best match between NIR-HSI and the SLF sensor. The root mean square error (RMSE) and bias for each sample are summarized in Table 2.

For the two samples with the smallest initial r_e (113 and 130 µm), precipitation particles and decomposed and fragmented particles, it was found that the LWC retrieval method did not perform well using any of the mixing models, with the highest RMSE and bias (Table 2). The retrieval is near 0 % LWC in dry snow conditions; however the LWC retrievals increase rapidly as small amounts of water are introduced. In the coated sphere model, the retrievals reach the LWC limit of the spectral library (25 %) when the measured LWC from the SLF sensor was ~ 10 % (Fig. 9b). For k_{eff} and interstitial spheres, there is a similar pattern of LWC increasing too fast, although these models do not reach the upper limit of the spectral library. Because none of the models evaluated performed well for small grain sizes, these two samples (113 and 130 µm) were excluded from the calculation of the best fit line (red line in Fig. 9). This result is discussed further in Sect. 5; however, the exclusion of these data is reasonable because water is not commonly mixed with these types of particles (new snow) in natural environments and therefore not a primary focus for wet snow mapping applications.

For the remaining samples, ranging from 176–898 µm, the mixing models retrieve LWC values that more closely match the SLF sensor measurements. Visually, both k_{eff} and interstitial spheres fall close to the 1 : 1 line. The k_{eff} spheres do have the lowest RMSE and bias for the smallest grains (Samples 1–3), but for the remaining samples containing medium-to large-sized grains, the retrieved LWC consistently has a negative bias, and the RMSE is ~ 2 %. Overall, the interstitial sphere model has the lowest RMSE (~ 1 %) and bias, which does not trend with grain size, with the best comparison for Samples 4–7 and similar values to k_{eff} for Sample 3. The uncertainty in the interstitial sphere model was determined by taking the mean RMSE across Samples 3–7, which is 1.4 %. This is supported by the dry snow retrieval shown in Fig. 8a, where no pixels retrieved greater than 1 % LWC. The coated sphere model performed most poorly relative to measurements with a high RMSE and consistently had a positive bias across all samples, although like the other mixing models, the values do fall close to the 1 : 1 line at low LWC (< 7 %). Overall, these experiments and model comparisons show that the interstitial sphere model performed exceptionally well for medium to large grains, and LWC ranges between 0 % and 15 %, which are the conditions most likely to be found in natural snow covers.

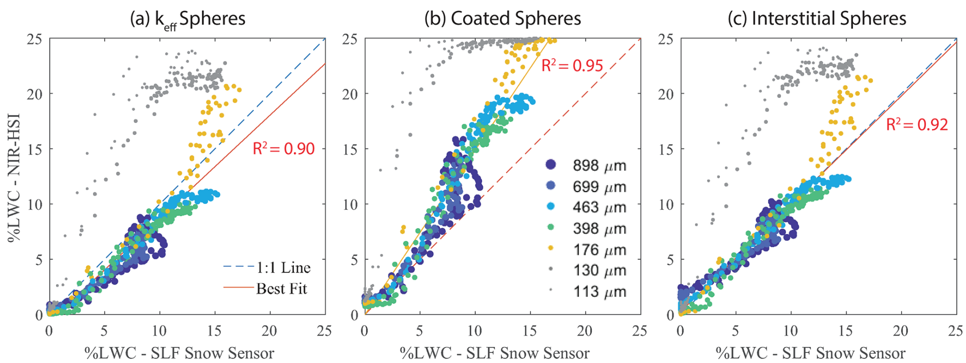

Figure 9. Comparison of LWC measured with the SLF Snow Sensor versus the mean LWC retrieved from NIR-HSI using the residual method. Three optical property mixing models are compared using the same datasets: **(a)** k_{eff} spheres, **(b)** coated spheres, and **(c)** interstitial spheres. The initial (dry) effective grain radius for each sample is shown in the legend, and the R^2 value is for the best fit line, which excludes 113 and 130 µm datasets.

Table 2. Liquid water content retrieval results from the laboratory (reported r_{e} is from scaled band area method). Bold values indicate the lowest RMSE and bias for a given sample.

				RMSE (% LWC)			Bias (% LWC)		
Sample number	n	Initial r_{e} (µm)	% LWC range	k_{eff} spheres	Coated spheres	Interstitial spheres	k_{eff} spheres	Coated spheres	Interstitial spheres
1	66	113	0–14.6	**8.7**	11.9	9.4	**7.5**	10.5	8.0
2	102	130	0–15.9	**7.7**	11.5	8.6	**7.1**	10.8	7.9
3	78	176	0–17.2	**2.0**	7.0	2.6	**1.0**	5.8	1.6
4	123	398	0–13.4	1.8	4.0	**0.9**	−1.5	3.2	**–0.5**
5	132	463	0–15.2	1.9	4.7	**1.1**	−1.5	4.0	**–0.3**
6	102	699	0–8.8	1.6	2.8	**1.0**	−1.2	2.3	**0.3**
7	90	898	0–10.4	2.2	3.3	**1.4**	−1.6	2.3	**–0.1**

4.1.2 Effective grain radius retrieval

Using the residual method, all mixing models retrieved similar grain size values because the grain size retrievals are primarily dependent on the absolute reflectance driven by ice absorption. Here, we present results from the interstitial sphere model because it performed best in the LWC retrieval. For initial dry snow conditions, the r_{e} retrieval using the scaled band area method ($r_{\mathrm{e,SBA}}$) had a positive bias relative to the residual method ($r_{\mathrm{e,residual}}$), and the bias becomes more positive with increasing grain size (Fig. 10). For the remaining wet snow comparisons, the $r_{\mathrm{e,SBA}}$ remains relatively constant or increases at low LWC followed by a decrease at high LWC. For Samples 1 and 2, $r_{\mathrm{e,SBA}}$ remained flat with increasing LWC. For Samples 3–6, $r_{\mathrm{e,SBA}}$ increased initially with low LWC and then decreases at high LWC. For Sample 7, $r_{\mathrm{e,SBA}}$ slightly increases before significantly decreasing with increasing LWC. In comparison, the $r_{\mathrm{e,residual}}$ increases with increasing LWC for all samples, which is expected because the presence of water is known to accelerate snow grain growth (Marsh, 1987). The comparison, further discussed in Sect. 5.2, shows that the scaled band area method is impacted by the presence of water, such that the residual method may be better suited for wet snow.

4.2 Field experiment

Although a controlled laboratory environment is ideal for identifying the best-suited optical mixing model, the primary applications for this method would be in situ field studies, motivating the field-based testing of the r_{e} and LWC retrieval. The maps of r_{e} and LWC generally reflect the profile measurements of LWC and stratigraphy, though at significantly higher detail (Fig. 11). The snowpit was representative of a spring intermountain snowpack undergoing melt, with the density values ranging from ~ 300 to $\sim 450\,\mathrm{kg\,m^{-3}}$ and LWC measurements ranging from $\sim 6\,\%$–$16\,\%$. The temperature profile, not shown, was isothermal at 0 °C. The general stratigraphy was ice lenses and melt form grains in the upper layers, rounded grains in the central portion, and faceted grains (depth hoar) near the ground. Note that the full pit profile is shown for observations (Fig. 11a and d), while the

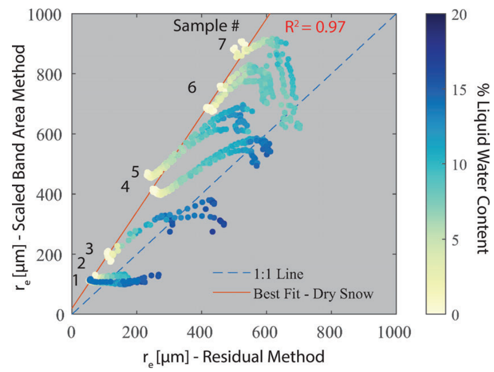

Figure 10. Mean effective grain radius (r_e) retrieval comparison between residual and scaled band area methods using the interstitial sphere model at each time step for Samples 1–7. Best fit line is drawn through the dry snow condition for each sample.

r_e and LWC retrievals extend across only the upper 110 cm (Fig. 11b and c).

The maps were processed using each of the mixing models introduced above, but based on the laboratory findings, only retrievals from the interstitial sphere model are presented here. The SLF sensor measurements were taken along the left side of the ruler (gray stripe or NaNs down the center of snowpit), represented as the dashed red box in Fig. 11c. For comparison, LWC was depth-averaged in pixels covering the area of the SLF sensor measurements (red line in Fig. 11d) in addition to the depth average LWC across the entire width of the snowpit (gray line in Fig. 11d). The mean LWC, standard deviation (σ), and number of measurements (n) for the SLF sensor, NIR-HSI along the same profile as the SLF sensor, and the depth average of the entire width of the snowpit are shown in Table 3. Generally, the LWC from the NIR-HSI retrieval had a positive bias compared to the SLF sensor, particularly notable at the top of the snowpack, although the patterns and peaks have similar trends. The difference between retrievals and measurements is discussed further in Sect. 5.1.

For comparison, when processed with the coated sphere model the LWC reached the model limit at 25 % over much of the scene. The k_{eff} sphere model did have mean values slightly closer to the SLF sensor; however this was not unexpected given that the laboratory results were biased negative. The magnitude of values, with coated spheres retrieving higher values and k_{eff} spheres retrieving lower values relative to interstitial spheres, mimics the bias present in laboratory results (Table 2).

The high resolution of the maps shows how stratigraphy influences r_e and LWC distributions in higher detail than can be captured with standard field-based observations. At the top of the snowpit, it can be discerned that the snow was saturated with water, which was pooling on top of the ice lens at 130 cm snow height. The SLF sensor only captures the average LWC, particularly between 110 and 130 cm, where there is high variability in LWC between layered ice lenses. At the ice lenses (130, 122, and 110 cm) the grains are large, while the LWC is low. Water pooling above ice lenses, rather than the ice lens itself having water content, is sensible because there is minimal pore space for water to reside or pass through. Below the ice lens, a few isolated preferential flow paths extend to lower layers, while other features show water concentrated (at ∼ 90 and ∼ 75 cm) but not flowing along the plane of the snowpit wall.

5 Discussion

5.1 Liquid water content retrieval

The interstitial sphere and k_{eff} sphere models performed similarly because the optical properties are volume-mixed in both cases, albeit internally versus externally mixed. The external mixing of interstitial water spheres results in a notable shift in the reflectance spectrum at wavelengths ranging from 1300–1450 nm when compared to k_{eff} spheres (Fig. 6). Since the interstitial sphere model performed the best, this result indicates that the particle size of water in wet snow plays an important role in the simulated reflectance, whereas the particle size of water is not considered in the k_{eff} model. Before mixing the optical properties, the particle size of the water sphere was the same size as the ice sphere, which is a reasonable approximation. It would be possible to mix water and ice spheres of differing size, although this approach is computationally expensive given that the number of possible simulated spectra combinations would approach infinity.

The coated sphere model performed reasonably in the pendular regime, where water is contained in menisci held in between the ice particles, but then considerably overestimated LWC in the funicular regime. The coated sphere model was chosen over the interstitial sphere model by Green et al. (2002), based on visual inspection, considering the bands in the ice absorption feature centered at 1030 cm, which encompasses only part of the distinct shifts between ice and water that are present in the complex refractive index across the NIR (Fig. 1). This study used a greater number of NIR bands that span multiple distinguishable shifts between ice and water, which is a more robust approach.

For small snow grains of PP (Sample 1) and DF (Sample 2) crystal type, LWC retrievals did not perform well using any of the models, one potential reason being that PP and DF crystal types are complex shapes, and reflectance may not be accurately represented using spheres. Using a ray tracing model, Picard et al. (2009) showed that grain shape can influence reflectance. Although it is possible to have wet PP and DF crystal types (e.g., rain on snow), low-density dendritic snow crystals are more commonly found at temperatures well below freezing (Judson and Doesken, 2000). It is far more common for wet snow to contain larger rounded grains pri-

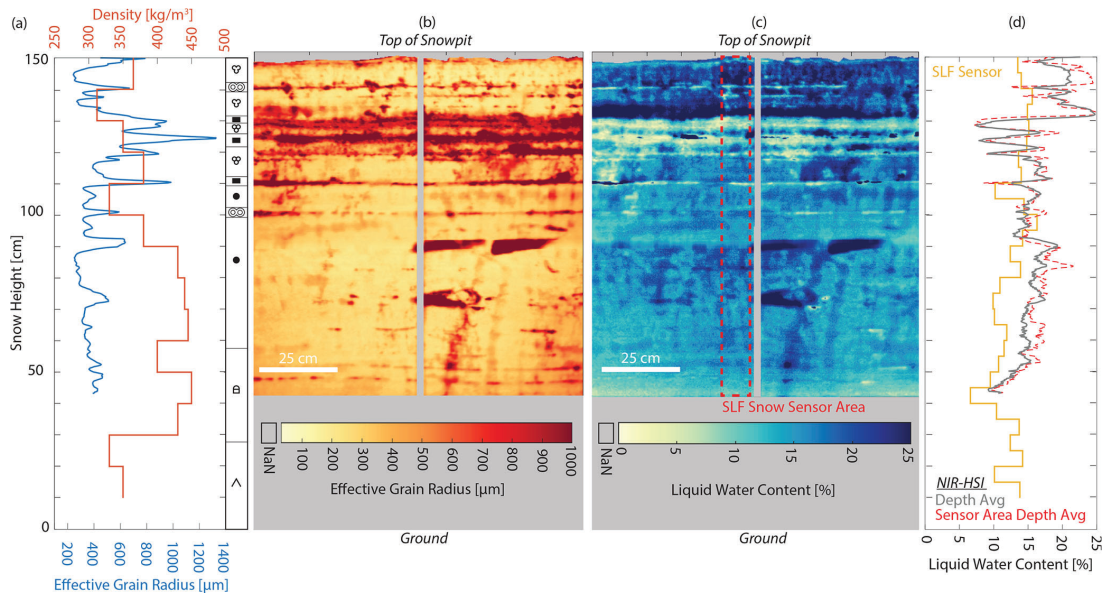

Figure 11. Results from the snowpit at Bridger Bowl Ski Area. **(a)** Density profile using 1000 cm^3 wedge cutter and depth-averaged effective grain radius. **(b)** Map of effective grain radius across snowpit wall. **(c)** Map of liquid water content across snowpit wall with the SLF sensor vertical profile area outlined by the dashed red line. **(d)** Liquid water content profiles from the SLF Snow Sensor, NIR-HSI depth averaged across the entire width of the snowpit, and NIR-HSI depth averaged over the area covered by the SLF sensor area only. NaN (not a number) values in **(b)** and **(c)** correspond to no retrieval data due to a ruler that was placed in the scene.

Table 3. Liquid water content retrieval results from the field.

		K_{eff} spheres		Coated spheres		Interstitial spheres	
	SLF sensor	Sensor area	Full profile	Sensor area	Full profile	Sensor area	Full profile
Mean LWC [%]	12.6	15.6	15.1	23.5	23.2	16.3	15.7
σ	2.3	3.2	2.7	1.8	1.1	3.4	3.2
n	28	21 758	243 386	21 758	243 386	21 758	243 386

marily because the presence of water rapidly increases the rate of snow grain growth, especially through melt and refreeze cycles. Small RG (Sample 3), having only slightly larger r_e values than the PP and DF crystals, performed similarly to the medium- and large-sized grains, further suggesting that the complex shapes of PP and DF may be driving the poor performance. Based on the results at small grain sizes, the mixing models have potential to classify dry versus wet snow but not quantitatively retrieve LWC.

Interestingly, for the largest grains, Samples 6 and 7, the highest LWC measurements from the SLF sensor are $\sim 10\,\%$ (Fig. 9). These apparent maxima, seen in both measurements and retrievals, are attributed to the large grains having a reduced water-holding capacity within the pore space (Yamaguchi et al., 2010). Although the snow sample could contain higher than 10 % LWC by volume, water is able to drain below the near-surface detection limit of the SLF sensor and NIR-HSI.

5.2 Effective grain radius retrieval

The scaled band area method assumes dry snow, but in remote sensing and field applications there is typically no a priori knowledge of snow wetness; thus comparing $r_{e,SBA}$ to $r_{e,residual}$ allows us to test the validity of this assumption for wet snow. To visualize the difference between the residual and scaled band area methods, an example of a measured spectrum from a dry and wet snow (12 % LWC) sample is shown in Fig. 12, along with the corresponding simulated spectrum retrieved using the two methods. For the dry snow spectrum, $r_{e,SBA}$ is larger than $r_{e,residual}$, which is a consistent trend across all samples (Fig. 10 best fit line). This is attributed to the scaled band area method using a fixed

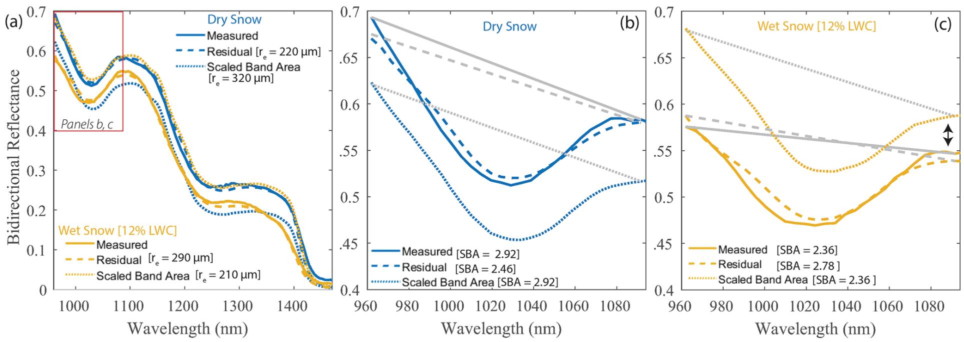

Figure 12. Effective grain radius (r_e) retrieval comparison between the residual and scaled band area methods using the interstitial sphere model. **(a)** An example of measured spectra from a dry and wet snow sample and the corresponding retrieved simulated spectra using the residual and scaled band area methods. **(b)** Dry snow spectra from **(a)** including the continuum lines, shown in gray, over the absorption feature. **(c)** Wet snow spectra from **(a)** including the continuum lines over the absorption feature, shown in gray.

wavelength range spanning the area of the absorption feature centered at 1030 nm (961 to 1087 nm), which makes it sensitive to small changes in the shape of the measured absorption feature and location of the continuum line shoulders (shown as gray lines in Fig. 12b), whereas the residual method finds the best fit spectrum over all NIR wavelengths ranging from 961 to 1472 nm. In the example shown (Fig. 12b), the left shoulder of the matched simulated spectrum using the residual method is slightly below the measured spectrum, resulting in the scaled band area of the measured spectrum (2.92) being higher than that of the matched simulated spectra (2.46).

In the wet snow case, the absorption feature centered at 1030 nm shifts to shorter wavelengths and broadens. Similar to the comparison for dry snow, the fixed wavelength range and continuum line of the scaled band area method fail to fully capture the wet snow absorption feature, resulting in a reduction in the scaled band area. This result is shown in the spectral reflectance example (Fig. 12c) and is responsible for the decreasing $r_{e,SBA}$ at high LWC seen for Samples 3–7 (Fig. 10). In this example, the shift to the left is highlighted with the arrow pointing to the flattening of the feature that is incorrectly included by the scaled band area fixed continuum line (shown as gray lines in Fig. 12c), resulting in a smaller scaled band area. This example also shows the broadening of the feature relative to the shape of ice absorption alone. The shape of the wet snow feature is better represented by the matched simulated spectrum using the residual method. It is possible that this has implications for previous studies that have applied the scaled band area method over potentially wet snow (e.g., Skiles and Painter, 2017).

5.3 Uncertainties

5.3.1 Simulated snow reflectance

All the mixing models examined in this study are approximate representations of the relative arrangement of ice and water in wet snow. The spherical particle approximation used in this study to represent wet snow is a reasonable approach because ice grains in the presence of water tend to be rounded. The arrangement of ice and water, on the other hand, is dependent on the level of water saturation; therefore using a single mixing model to determine the LWC across a large range of water saturations results in inherent uncertainty. Since no a priori knowledge of snow wetness is known when taking NIR-HSI measurements, the goal of this research only aims to find the modeling approach that has the best retrieval of LWC across ranges commonly found in natural environments when compared to an established dielectric-based instrument.

Simulations of clean snow reflectance, assuming no LAPs, were valid for the laboratory experiments; however snow in natural environments contains varying concentrations of LAPs. Since LAPs predominately effect the visible part of the spectrum (Nolin and Dozier, 2000), it is unlikely that typical concentrations would impact this retrieval method. However, at high concentrations of LAPs their impact extends into the NIR, and in extreme cases this can make the ice absorption feature more shallow (Skiles et al., 2018), which would increase uncertainties in this retrieval method.

5.3.2 Measured snow reflectance

There is uncertainty in the measurement of absolute spectral reflectance, the accuracy of which is important for using the residual method. To minimize this uncertainty in the laboratory, spectral measurements were taken with consistent lighting conditions and at close proximity, resulting in near-perfect conditions, which was ideal for the comparison study. Similarly, uncertainties related to lighting conditions in the field experiment were minimized by blocking all sunlight with an opaque tarp and illuminating the snowpit wall with a known lighting source. This approach is recommended and is used with other optical methods, such as contact spectroscopy (Painter et al., 2007; Skiles and Painter, 2017). Using natural light in a standard snowpit orientation (i.e., facing away from the sun) would make the conversion from radiance to reflectance challenging because the snowpit wall is unevenly illuminated by diffuse light and would need to be accounted for in the radiative transfer modeling. Additionally, there may not be enough light on the snowpit wall for imaging; however, this was not tested here.

Similarly, if the orientation of the imager or light source is off-nadir, this needs to be accounted for in the radiative transfer modeling such that the measured and simulated spectra are comparable. Here, we did not image the bottom 40 cm of the snowpit because positioning the camera and lights off-nadir would introduce errors in the comparison to the simulated spectra at nadir viewing, which is discussed in more detail in Donahue et al. (2021). However, the full snowpit could be imaged in nadir orientation by digging a larger snowpit such that the camera and lighting source are farther away from the snowpit wall or by using a tripod that lowers closer to the ground.

Additionally, the residual method benefits from the high signal-to-noise ratio (1885) and spectral resolution (4.9 nm) of the instrument used here. For application of this method at the airborne or satellite scales, spectral measurements contain more noise than those in the laboratory and require atmospheric and topographic correction, introducing additional uncertainty into absolute reflectance values. Although not within the scope of this study, instruments at these scales also need to account for water vapor in the air, which is discussed further in Green et al. (2006). Finally, due to the relatively minor shift in NIR reflectance, this approach is likely not suitable for mixed pixels (not pure snow), which become more common as spatial coverage and pixel sizes increase.

5.3.3 Dielectric liquid water content measurements

Dielectric instruments, including the SLF sensor used here, have their own uncertainties. Based on the empirical calibration of the SLF sensor (FPGA Company, 2018), the RMSE of the LWC measurement is $\sim 1.2\,\%$. These types of instruments also rely on an independent snow density measurement to calculate LWC. In the case of the SLF sensor, the "dry snow" density, which describes the fraction of ice in a wet snow volume, is required to calculate a LWC value (FPGA Company, 2018). In the laboratory experiments, this was not an issue because all snow samples started dry, and the dry snow density was used for all subsequent LWC measurements during melt. Conversely, in the field experiment, the snow was already wet, and there was no way of isolating a dry snow density. The preferred solution offered by FPGA Company (2018) is to measure density in the morning if the snow has refrozen, but this was not possible here. A second solution, described in Sect. 3.2.2 and applied here, is to use an iterative approach to determine an estimated dry snow density. Since the measured LWC is dominated by water content rather than snow density, the change in corrected LWC was small, ranging from 0.4 %–1.2 %. Due to the cubic empirical calibration curve (FPGA Company, 2018), high LWC values had a smaller correction, while smaller LWC values had a larger correction. Nevertheless, a known dry snow density at the time of measurement would give the most accurate LWC measurement from the SLF sensor. Although there is inherent uncertainty associated with the SLF sensor, it was found to be the most suitable LWC measurement instrument for comparison to LWC retrieved from NIR reflectance because it is non-destructive to the snow surface, measures a flat surface, and has minimal penetration into snow, similar to NIR light.

5.3.4 Field measurements

Acquiring a vertical profile of LWC, using any instrument, requires digging a snowpit and exposing the sidewall. The atmospheric exposure can change snow properties and introduce uncertainties to the measurement. Shea et al. (2012) observed that a statistically significant change in the surface temperature across a snowpit wall occurred within the first 90 s of exposure, providing evidence that atmospheric equalization affects the surface temperature more strongly than from heat behind the snowpit wall. Here, the snowpit was isothermal, and the air temperature was above freezing (10 °C), meaning that any additional energy into the snowpack directly goes to melting snow and increasing LWC. To minimize these uncertainties, a systematic approach was taken where the snowpit sidewall was cut back ~ 10 cm prior to taking hyperspectral images and SLF sensor measurements. Additionally, the snowpit was covered with an opaque tarp, blocking all diffuse sunlight on the snowpit wall. Acquiring two hyperspectral images took approximately 2 min, while acquiring the 28 SLF sensor measurements in a vertical profile took approximately 5 min, resulting in the snowpit sidewall being exposed for ~ 7 min. The comparison of the two instruments cannot occur simultaneously and requires the snowpit to be exposed for an extended time, which would lead to uncertainties if the LWC on the snowpit wall increased during this time.

5.4 Implications for future applications

Controls on liquid water movement through snow include LWC, grain size, and wet snow metamorphism (Hirashima et al., 2019). Multi-dimensional snowmelt models have been developed to represent the relationship between grain growth and water percolation (Hirashima et al., 2014), but limited observations for validation at large spatial scales currently exist. Being able to coincidently map r_e and LWC spatial distributions in such high detail could support process-based studies and validate models coupling wetting front propagation with grain size and grain growth.

Coincident r_e and LWC maps could also be used to better interpret microwave remote sensing retrievals and for comparison to microwave radiative transfer models, such as the Microwave Emission Model for Layered Snowpacks (MEMLS) (Wiesmann and Mätzler, 1999) and the Dense Media Radiative Transfer Multi-Layer model (DMRT-ML) (Picard et al., 2013). Generally, these models are initialized with physical snow properties, including r_e, LWC, and layer thickness. Currently, discrete in situ measurements of r_e and LWC measurements are taken using instruments, such as the IceCube and the SLF sensor, respectively. These instruments are generally affordable and portable and do not require a large snowpit working space. However, to measure snow properties, multiple instruments are needed, and measurements are discrete and asynchronous, making it challenging to capture spatial variability. Additionally, multiple measurements require the snowpit wall to be exposed for longer, increasing uncertainty in the measured snow properties. Although logistically more challenging to implement in the field, the NIR-HSI method addresses these limitations by measuring r_e, LWC, and layer thickness in high resolution simultaneously while minimizing the time the snowpit wall is exposed to ambient air.

There is also broader relevance for the assessment and development of snow property retrievals from measured spectral reflectance with upcoming satellite imaging spectrometer missions. These include the Surface Biology and Geology (SBG) imaging spectrometer mission and the Copernicus Hyperspectral Imaging Mission (CHIME). Although algorithm suites have been developed to retrieve snow properties from airborne imaging spectroscopy (Painter et al., 2013), LWC is not a standard part of the retrieval and has only been demonstrated as a case study (Green et al., 2002). Time series mapping of LWC could be used to monitor melt initiation and how it varies with slope, aspect, and elevation.

6 Conclusions

The results in this study show that the externally mixed interstitial sphere model performs best when compared to a dielectric LWC measurement instrument, relative to the previously proposed k_{eff} sphere (Hyvarinen and Lammasniemi, 1987) and coated sphere models (Green et al., 2002). It was also found that for the smallest grains (i.e., new and decomposing precipitation particles), none of the models investigated compared well to the SLF sensor. For low LWC (< 7 %), all the retrievals compare well to measurements, but at higher LWC the k_{eff} and coated spheres were biased positive and negative, respectively. Overall and across the widest range of initial grain types, r_e (162–859 µm) and LWC (0 %–17.2 %), *the interstitial sphere model performed the best*, with ~ 1 % uncertainty.

For the r_e comparison, between the two optically based residual and scaled band area methods, it was found that the scaled band area retrieval had a positive bias compared to the residual method. This bias was lowest for small grains and increased with grain size. For wet snow, the scaled band area method was impacted by the presence of water due to the shift in the absorption feature to shorter wavelengths, resulting in decreasing r_e at high LWC. Because scaled band area implicitly assumes dry snow, it is based on ice absorption alone, and caution is encouraged when applying this method without knowing that the snow is dry.

The field application of the NIR-HSI method produced maps that reflect the general understanding of what a snapshot of a snowpit would look like during snowmelt progression but mapped the stratigraphy of snow properties (i.e., LWC and grain size) at much higher resolution relative to standard profile-based observations. The retrieved LWC was found to be slightly higher than that measured by the SLF sensor, which was attributed to both the inability to determine the dry snow density and the high level of detail in the maps that could not be captured by the volume-averaged dielectric sensor.

Data availability. Data will be available upon request from the lead author.

Author contributions. CD conceptualized the study, collected laboratory and field data, conducted DISORT model simulations, and analyzed the results. SMS provided the hyperspectral imager, assisted with data collection, and advised CD during conceptualization and DISORT model simulations. KH acquired funding for this research, was responsible for project administration, and supervised CD throughout the study. CD wrote the original draft manuscript, and all co-authors contributed during review and editing.

Competing interests. The contact author has declared that neither they nor their co-authors have any competing interests.

Disclaimer. Publisher's note: Copernicus Publications remains neutral with regard to jurisdictional claims in published maps and institutional affiliations.

Acknowledgements. This research was supported by the NASA New Investigator Program award 80NSSC18K0822. Additionally, S. McKenzie Skiles was supported by the NSF CZO-Net award EAR-2012091. We thank Joseph Shaw for providing the Resonon linear scanning stage used in this study. We thank

Michael Dvorsak and Ladean McKittrick for their assistance in the laboratory. We thank Pete Maleski and the Bridger Bowl Ski Patrol for allowing us to conduct fieldwork at the Alpine Weather Station and for transporting our instruments into the field. We acknowledge the use of the Subzero Research Laboratory in the Department of Civil Engineering at Montana State University. We thank Ryan Webb and Chander Shekhar for providing insightful comments that helped improve this paper.

Financial support. This research has been supported by the National Aeronautics and Space Administration (grant no. 80NSSC18K0822). S. McKenzie Skiles was funded by the National Science Foundation award EAR-2012091.

Review statement. This paper was edited by Carrie Vuyovich and reviewed by Chander Shekhar and Ryan Webb.

References

A2 Photonic Sensors: WISe – Snow liquid water content sensor – User Manual, A2 Photonics Sensors, Grenoble, France, 2019.

Avanzi, F., Hirashima, H., Yamaguchi, S., Katsushima, T., and De Michele, C.: Observations of capillary barriers and preferential flow in layered snow during cold laboratory experiments, The Cryosphere, 10, 2013–2026, https://doi.org/10.5194/tc-10-2013-2016, 2016.

Bohren, C. F. and Huffman, D. R.: Absorption and scattering of light by small particles, John Wiley & Sons, ISBN-13: 978-0-471-29340-8, 2008.

Colbeck, S.: Grain clusters in wet snow, J. Colloid Interface Sci., 72, 371–384, 1979.

Colbeck, S. C.: An overview of seasonal snow metamorphism, Rev. Geophys., 20, 45–61, 1982.

Conway, H. and Raymond, C. F.: Snow stability during rain, J. Glaciol., 39, 635–642, https://doi.org/10.3189/S0022143000016531, 1993.

Davis, R. E., Dozier, J., LaChapelle, E. R., and Perla, R.: Field and laboratory measurements of snow liquid water by dilution, Water Resour. Res., 21, 1415–1420, 1985.

Davis, R. E., Nolin, A. W., Jordan, R., and Dozier, J.: Towards predicting temporal changes of the spectral signature of snow in visible and near-infrared wavelengths, Ann. Glaciol., 17, 143–148, https://doi.org/10.3189/S026030550001274X, 1993.

Denoth, A.: An electronic device for long-term snow wetness recording, Ann. Glaciol., 19, 104–106, 1994.

Denoth, A., Foglar, A., Weiland, P., Mätzler, C., Aebischer, H., Tiuri, M., and Sihvola, A.: A comparative study of instruments for measuring the liquid water content of snow, J. Appl. Phys., 56, 2154–2160, 1984.

DeWalle, D. R. and Rango, A.: Principles of snow hydrology, Cambridge University Press, Cambridge, ISBN 978-0-521-29032-6, 2008.

Donahue, C., Skiles, S. M., and Hammonds, K.: In situ effective snow grain size mapping using a compact hyperspectral imager, J. Glaciol., 67, 49–57, 2021.

Dumont, M., Brissaud, O., Picard, G., Schmitt, B., Gallet, J.-C., and Arnaud, Y.: High-accuracy measurements of snow Bidirectional Reflectance Distribution Function at visible and NIR wavelengths – comparison with modelling results, Atmos. Chem. Phys., 10, 2507–2520, https://doi.org/10.5194/acp-10-2507-2010, 2010.

Eiriksson, D., Whitson, M., Luce, C. H., Marshall, H. P., Bradford, J., Benner, S. G., Black, T., Hetrick, H., and McNamara, J. P.: An evaluation of the hydrologic relevance of lateral flow in snow at hillslope and catchment scales, Hydrol. Process., 27, 640–654, 2013.

Fierz, C., Armstrong, R., Durand, Y., Etchevers, P., Greene, E., McClung, D., Nishimura, K., Satyawali, P., and Sokratov, S.: The international classification for seasonal snow on the ground, IHP-VII Technical Documents in Hydrology No. 83, IACS Contribution No. 1, UNESCO-IHP, Paris, 2009.

FPGA Company: SLF Snow Sensor – User Manual, Version 1.4, FPGA Company, available at: https://fpga-company.com/wp-content/uploads/2018/10/SLFSnowSensor-User-Manual-Version-1.3.pdf (last access: 5 November 2021), 2018.

Gerdel, R. W.: The transmission of water through snow, Eos Trans. Am. Geophys. Union, 35, 475–485, 1954.

Green, R. O., Dozier, J., Roberts, D., and Painter, T.: Spectral snow-reflectance models for grain-size and liquid-water fraction in melting snow for the solar-reflected spectrum, Ann. Glaciol., 34, 71–73, https://doi.org/10.3189/172756402781817987, 2002.

Green, R. O., Painter, T. H., Roberts, D. A., and Dozier, J.: Measuring the expressed abundance of the three phases of water with an imaging spectrometer over melting snow, Water Resour. Res., 42, W10402, https://doi.org/10.1029/2005WR004509, 2006.

Gupta, R. P., Haritashya, U. K., and Singh, P.: Mapping dry/wet snow cover in the Indian Himalayas using IRS multispectral imagery, Remote Sens. Environ., 97, 458–469, https://doi.org/10.1016/j.rse.2005.05.010, 2005.

Hirashima, H., Yamaguchi, S., and Katsushima, T.: A multi-dimensional water transport model to reproduce preferential flow in the snowpack, Cold Reg. Sci. Technol., 108, 80–90, https://doi.org/10.1016/j.coldregions.2014.09.004, 2014.

Hirashima, H., Avanzi, F., and Wever, N.: Wet-snow metamorphism drives the transition from preferential to matrix flow in snow, Geophys. Res. Lett., 46, 14548–14557, 2019.

Hyvarinen, T. and Lammasniemi, J.: Infrared measurement of free-water content and grain size of snow, Opt. Eng., 26, 264342, https://doi.org/10.1117/12.7974077, 1987.

Jones, E., Rango, A., and Howell, S.: Snowpack liquid water determinations using freezing calorimetry, Hydrol. Res., 14, 113–126, 1983.

Judson, A. and Doesken, N.: Density of freshly fallen snow in the central Rocky Mountains, B. Am. Meteorol. Soc., 81, 1577–1588, 2000.

Kuroda, M. and Hurukawa, I.: Measurement of water content of snow, in: Proceedings of the Rome symposium, Int. Assoc. of Hydrol. Sci. and Assoc. Int. des Hydrol., vol. 39 (IV), IAHS Publ., Rome, 38–41, 1954.

Lesins, G., Chylek, P., and Lohmann, U.: A study of internal and external mixing scenarios and its effect on aerosol optical properties and direct radiative forcing, J. Geophys. Res.-Atmos., 107, AAC 5-1–AAC 5-12, 2002.

Lund, J., Forster, R. R., Rupper, S. B., Deeb, E. J., Marshall, H., Hashmi, M. Z., and Burgess, E.: Mapping snowmelt progression in the Upper Indus Basin with synthetic aperture radar, Front. Earth Sci., 7, 318, https://doi.org/10.3389/feart.2019.00318, 2020.

Lundberg, A.: Laboratory calibration of TDR-probes for snow wetness measurements, Cold Reg. Sci. Technol., 25, 197–205, 1997.

Marsh, P.: Grain growth in a wet arctic snow cover, Cold Reg. Sci. Technol., 14, 23–31, https://doi.org/10.1016/0165-232X(87)90041-3, 1987.

Mätzler, C.: MATLAB functions for Mie scattering and absorption, version 2, available at: https://boris.unibe.ch/146550/1/199.pdf (last access: 5 November 2021), 2002.

Mazurkiewicz, A. B., Callery, D. G., and McDonnell, J. J.: Assessing the controls of the snow energy balance and water available for runoff in a rain-on-snow environment, J. Hydrol., 354, 1–14, https://doi.org/10.1016/j.jhydrol.2007.12.027, 2008.

Nolin, A. W. and Dozier, J.: A Hyperspectral Method for Remotely Sensing the Grain Size of Snow, Remote Sens. Environ., 74, 207–216, https://doi.org/10.1016/S0034-4257(00)00111-5, 2000.

Painter, T. H., Molotch, N. P., Cassidy, M., Flanner, M., and Steffen, K.: Contact spectroscopy for determination of stratigraphy of snow optical grain size, J. Glaciol., 53, 121–127, https://doi.org/10.3189/172756507781833947, 2007.

Painter, T. H., Seidel, F. C., Bryant, A. C., McKenzie Skiles, S., and Rittger, K.: Imaging spectroscopy of albedo and radiative forcing by light-absorbing impurities in mountain snow, J. Geophys. Res.-Atmos., 118, 9511–9523, 2013.

Picard, G., Arnaud, L., Domine, F., and Fily, M.: Determining snow specific surface area from near-infrared reflectance measurements: Numerical study of the influence of grain shape, Cold Reg. Sci. Technol., 56, 10–17, 2009.

Picard, G., Brucker, L., Roy, A., Dupont, F., Fily, M., Royer, A., and Harlow, C.: Simulation of the microwave emission of multi-layered snowpacks using the Dense Media Radiative transfer theory: the DMRT-ML model, Geosci. Model Dev., 6, 1061–1078, https://doi.org/10.5194/gmd-6-1061-2013, 2013.

Rowe, P., Fergoda, M., and Neshyba, S.: Temperature-Dependent Optical Properties of Liquid Water From 240 to 298 K, J. Geophys. Res.-Atmos., 125, e2020JD032624, https://doi.org/10.1029/2020JD032624, 2020.

Schmid, L., Heilig, A., Mitterer, C., Schweizer, J., Maurer, H., Okorn, R., and Eisen, O.: Continuous snowpack monitoring using upward-looking ground-penetrating radar technology, J. Glaciol., 60, 509–525, 2014.

Schneebeli, M.: Development and stability of preferential flow paths in a layered snowpack, IAHS Publications, Series of Proceedings and Reports, Int. Assoc. Hydrolog. Sci., 228, 89–96, 1995.

Seligman, G., Seligman, G. A., and Douglas, C.: Snow structure and ski fields: being an account of snow and ice forms met with in nature, and a study on avalanches and snowcraft, Macmillan and Company, LTd, https://doi.org/10.1002/jctb.5000561864, 1936.

Shea, C., Jamieson, B., and Birkeland, K. W.: Use of a thermal imager for snow pit temperatures, The Cryosphere, 6, 287–299, https://doi.org/10.5194/tc-6-287-2012, 2012.

Shekhar, C., Srivastava, S., Negi, H. S., and Dwivedi, M.: Hyperspectral data based investigations for snow wetness mapping, Geocarto Int., 34, 664–687, 2019.

Shi, J. and Dozier, J.: Radar backscattering response to wet snow, in: IEEE Proc. IGARSS'92, 26–29 May 1992, Houston, TX, USA, Piscataway, NJ, USA, 927–929, 1992.

Sihvola, A. and Tiuri, M.: Snow fork for field determination of the density and wetness profiles of a snow pack, IEEE T. Geosci. Remote, GE-24, 717–721, 1986.

Skiles, S. M. and Painter, T.: Daily evolution in dust and black carbon content, snow grain size, and snow albedo during snowmelt, Rocky Mountains, Colorado, J. Glaciol., 63, 118–132, 2017.

Skiles, S. M., Flanner, M., Cook, J. M., Dumont, M., and Painter, T. H.: Radiative forcing by light-absorbing particles in snow, Nat. Clim. Change, 8, 964–971, 2018.

Stamnes, K., Tsay, S.-C., Wiscombe, W., and Jayaweera, K.: Numerically stable algorithm for discrete-ordinate-method radiative transfer in multiple scattering and emitting layered media, Appl. Optics, 27, 2502–2509, 1988.

Stein, J., Laberge, G., and Lévesque, D.: Monitoring the dry density and the liquid water content of snow using time domain reflectometry (TDR), Cold Reg. Sci. Technol., 25, 123–136, 1997.

Tiuri, M., Sihvola, A., Nyfors, E., and Hallikaiken, M.: The dielectric constant of snow at microwave frequencies, IEEE J. Ocean. Eng., 9, 377–382, 1984.

Waldner, P. A., Schneebeli, M., Schultze-Zimmermann, U., and Flühler, H.: Effect of snow structure on water flow and solute transport, Hydrol. Process., 18, 1271–1290, https://doi.org/10.1002/hyp.1401, 2004.

Walker, A. and Goodison, B.: Discrimination of a wet snow cover using passive microwave satellite data, Ann. Glaciol., 17, 307–311, 1993.

Warren, S. G. and Brandt, R. E.: Optical constants of ice from the ultraviolet to the microwave: A revised compilation, J. Geophys. Res.-Atmos., 113, D14220, https://doi.org/10.1029/2007jd009744, 2008.

Webb, R., Williams, M. W., and Erickson, T.: The spatial and temporal variability of meltwater flow paths: Insights from a grid of over 100 snow lysimeters, Water Resour. Res., 54, 1146–1160, 2018.

Webb, R. W., Jennings, K., Finsterle, S., and Fassnacht, S. R.: Two-dimensional liquid water flow through snow at the plot scale in continental snowpacks: simulations and field data comparisons, The Cryosphere, 15, 1423–1434, https://doi.org/10.5194/tc-15-1423-2021, 2021.

Wiesmann, A. and Mätzler, C.: Microwave emission model of layered snowpacks, Remote Sens. Environ., 70, 307–316, 1999.

Williams, M. W., Erickson, T. A., and Petrzelka, J. L.: Visualizing meltwater flow through snow at the centimetre-to-metre scale using a snow guillotine, Hydrol. Process., 24, 2098–2110, 2010.

Yamaguchi, S., Katsushima, T., Sato, A., and Kumakura, T.: Water retention curve of snow with different grain sizes, Cold Reg. Sci. Technol., 64, 87–93, https://doi.org/10.1016/j.coldregions.2010.05.008, 2010.

Yosida, Z.: A Method for Determining the Thaw Water Content in a Snow Layer, J. Meteorol. Soc. Jpn. Ser. II, 18, 321–328, 1940.

Zuanon, N.: A2 Photonic Sensors: IceCube, a portable and reliable instrument for snow specific surface area measurement in the field, in: International Snow Science Workshop, Grenoble, Chamonix Mont-Blanc, 2013.

CHAPTER FOUR

LABORATORY OBSERVATIONS OF PREFERENTIAL FLOW PATHS IN SNOW USING UPWARD-LOOKING POLARIMETRIC RADAR AND HYPERSPECTRAL IMAGING

Manuscript in Chapter 4

Author: Christopher Donahue

Contributions: Co-conceptualized the study, collected radar and hyperspectral imaging data in the laboratory, processed and analyzed data, created visualizations, and wrote the original manuscript.

Co-Author: Kevin Hammonds

Contributions: Co-conceptualized the study, acquired funding for this research, was responsible for project administration, supervised CD throughout the study, and reviewed and edited the original draft manuscript.

Manuscript Information

Christopher Donahue and Kevin Hammonds
Remote Sensing
Status of Manuscript:
____ Prepared for submission to a peer-reviewed journal
____ Officially submitted to a peer-reviewed journal
__x__ Accepted by a peer-reviewed journal
____ Published in a peer-reviewed journal

Multidisciplinary Digital Publishing Institute
Submitted: 22 March 2022
Accepted: 24 April 2022
Published in Print:

remote sensing

Article

Laboratory observations of preferential flow paths in snow using upward-looking polarimetric radar and hyperspectral imaging

Christopher Donahue[1,*] and Kevin Hammonds[1]

[1] Department of Civil Engineering, Montana State University, Bozeman, MT, 59717, USA; donahue@christopher@outlook.com, kevin.hammonds@montana.edu
* Correspondence: donahue@christopher@outlook.com

Abstract: Infiltration of liquid water in a seasonal snowpack is a complex process that consists of two primary mechanisms: a semi-uniform melting front, or matrix flow, and heterogeneous preferential flow paths. Distinguishing between these two mechanisms is important for monitoring snow melt progression, which is relevant for hydrology and avalanche forecasting. It has been demonstrated that single co-polarized upward-looking radar can be used to track matrix flow, whereas preferential flow paths have yet to be detected. Here, from within a controlled laboratory environment, continuous polarimetric upward-looking C-band radar was used to monitor melting snow samples to determine if cross-polarized radar returns were sensitive to the presence and development of preferential flow paths. The experimental dataset consisted of six samples, for which the melting process was interrupted at increasing stages of preferential flow path development. Using a new serial-section hyperspectral imaging method, polarimetric radar returns were compared against the 3-dimensional liquid water content distribution and preferential flow path morphology. It was observed that the cross-polarized signal increased by 13.1 dB across these experiments. This comparison showed that the metrics used to characterize the flow path morphology related to the increase in cross-polarized radar returns spanning the six samples, indicating that upward-looking polarimetric radar has potential to identify preferential flow paths.

Keywords: upward-looking radar, hyperspectral imaging, wet snow, liquid water content, preferential flow paths

Citation: Donahue, C.; Hammonds, K.; Laboratory observations of preferential flow paths in snow using upward-looking polarimetric radar and hyperspectral imaging. *Remote Sens.* **2022**, *14*, x. https://doi.org/10.3390/xxxxx

Academic Editor:

Received: March 22, 2022
Accepted:
Published:

1. Introduction

The initiation of snow melt and subsequent infiltration of liquid water into a seasonal snowpack are important processes for snow hydrology and avalanche forecasting. Movement of liquid water in the snowpack is generally described as either homogenous matrix flow or heterogenous preferential flow. Homogenous matrix flow describes the slow vertical melting front that initiates at the top of the snowpack and moves vertically downward, semi-uniformly, within the horizontal plane [1]. Preferential flow paths, typically preceding homogenous matrix flow [2], are pathways of concentrated water that can transport large amounts of water vertically through the snowpack [3, 4]. When preferential flow paths reach an impermeable layer in the snowpack, such as an ice crust or capillary barrier, water will begin to pool and flow laterally [5], which can increase wet snow avalanche hazard by weakening the snow and lubricating the layer [6]. Observations of preferential flow paths have been predominately made using dye tracers (e.g., [7]), though these types of experiments rely on destructive sampling to visualize a single time step. Although preferential flow paths play a large role in water transport within a snowpack [8], they are challenging to detect and measure.

Non-destructive measurements of snow properties, including wet snow, have been demonstrated using radar, which at longer wavelengths can penetrate through the snow volume [9]. For ground-based radar remote sensing of wet snow, radars have been used in various viewing configurations, including downward-, side-, and upward-looking configurations. Downward-looking radars are limited in wet snow conditions, when the snow surface becomes saturated with water, due to the attenuation and reduced penetration of microwaves [10]. Side-looking radar has been demonstrated to identify preferential flow paths in a natural snowpack by excavating a snowpit and orienting the antennas perpendicular to the snowpit wall [11], however, this is not a practical method for continuous snow monitoring. A promising configuration for continuous wet snow monitoring has been shown to be upward-looking radar [12], buried underneath the snowpack, because the attenuation of microwaves does not happen until the melting front reaches the base of the snowpack and observations can occur non-destructively over a longer period of time relative to downward-looking radar at similar wavelengths.

The application of radar in an upward-looking configuration was first demonstrated by Gubler and Hiller [13], which has led to additional studies exploring the capability for continuous snowpack monitoring in dry and wet snow conditions. In dry snow, previous retrievals from ground-penetrating (GPR) and L-band (1-2 GHz) frequency modulated continuous wave (FMCW) radars have included snow height, internal stratigraphy layers, settlement, and density [14-18]. In wet snow conditions, previous retrievals from GPR have included volumetric liquid water content (LWC) and homogenous matrix flow tracking as it approaches the radar [12].

In this previous work, data was primarily collected using a single co-polarized configuration; the radar transmits and receives electromagnetic (EM) waves in the same orientation, either vertical-vertical (VV) or horizontal-horizontal (HH). In this configuration, co-polarized backscatter (σ_{VV} or σ_{HH}) is dominated by single bounce reflections, which are useful for identifying planar features perpendicular to the antennas that have variations in relative permittivity (ε_r), such as the air-snow interface, stratigraphy layers, pooling water on an impermeable layer, and homogenous matrix flow, examples of which are shown in Figure 1a-b. The detection of preferential flow paths has not been demonstrated in the upward-looking configuration, which is likely because the structure and spatial heterogeneity of preferential flow paths do not return a strong and consistent co-polarized signal that can be differentiated from other horizontal layers in the snowpack.

Although not yet demonstrated in an upward-looking configuration in wet snow, polarimetric radar data is generally better suited to extract geometrical structure, shape, and orientation of the target [19] and may have potential for identifying the presence of preferential flow paths. In addition to co-polarized data, full polarimetric radars include cross-polarized transmit-receive data (i.e., vertical-horizontal (VH) and horizontal-vertical (HV). Cross-polarized backscatter (σ_{VH} or σ_{HV}) is a result of the incident EM wave being depolarized as a result of multiple scattering events that can occur at the surface due to roughness, or within the volume due to inhomogeneities in the bulk material that contain variations in ε_r [20]. Dry snow, consisting of ice and air, has a low ε_r (~1.8), whereas liquid water has a much greater ε_r (~88) [21, 22]. When preferential flow paths are present, the volume of the snowpack contains large heterogenous variations in ε_r, such that multiple scattering events and the subsequent depolarization of an EM wave is probable. The idealized schematic in Figure 1c illustrates the concept behind this hypothesis.

The goal of this study was to test the hypothesis that preferential flow paths within a snow volume will depolarize an incident EM wave, causing an enhanced cross-polarized signal using an upward-looking polarimetric radar. This was tested within a controlled laboratory environment by taking continuous polarimetric radar measurements of prepared snow samples while they were melted from above using a simulated solar lamp. To quantitatively characterize the LWC and morphology of the preferential flow paths, for comparison to the collected radar data, at the end of each experiment the snow samples were serial-sectioned and LWC maps from hyperspectral imaging were used to create a reconstructed 3D model of LWC [23].

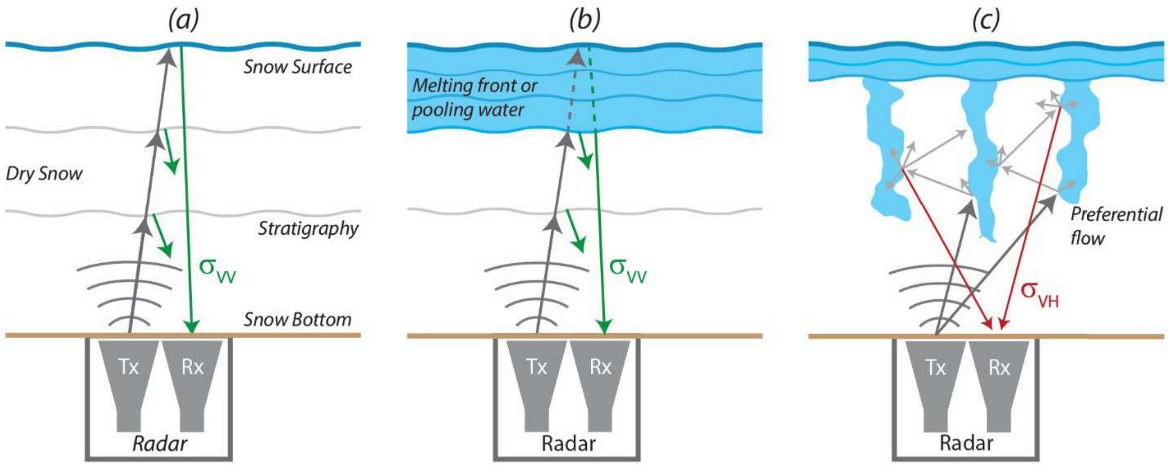

Figure 1. Idealized schematic of an upward-looking radar configuration in (a) dry snow, (b) melting snow with wetting front or pooling water (c) preferential flow paths. Single bounce returns are co-polarized (σ_{VV}, shown in green), while multiple scattering returns are depolarized and detected with the cross-polarized antenna (σ_{VH}, shown in red).

2. Methods

From within a controlled laboratory environment, where prescribed snow structures can be manufactured and characterized, upward-looking polarimetric radar was used to investigate the feasibility of detecting preferential flow paths. Snow samples were prepared and placed underneath a simulated solar lamp to induce melt while being continuously measured by a C-band (7.29 GHz) radar. The experimental set presented here consists of six snow samples, each one terminated at progressively increased stages of preferential flow path development. Following termination, the snow samples were near-coincidently serial-sectioned and imaged with a hyperspectral imager before a per-pixel LWC was retrieved across each image using the methodology described in [23]. The stack of serial-section images was reconstructed into a 3D model representing the distribution of LWC within the sample, such that preferential flow paths could be characterized and compared to the radar data. Preferential flow morphology parameters, computed by binarizing the 3D model at different LWC thresholds, were compared against the cross-polarized radar returns integrated over the snow sample volume at the end of the melting experiment ($(\sigma_{VH}^{vol})_{t=end}$). Additional experimental detail is given in sections 2.1-2.4, while an experimental workflow is presented in Figure 2.

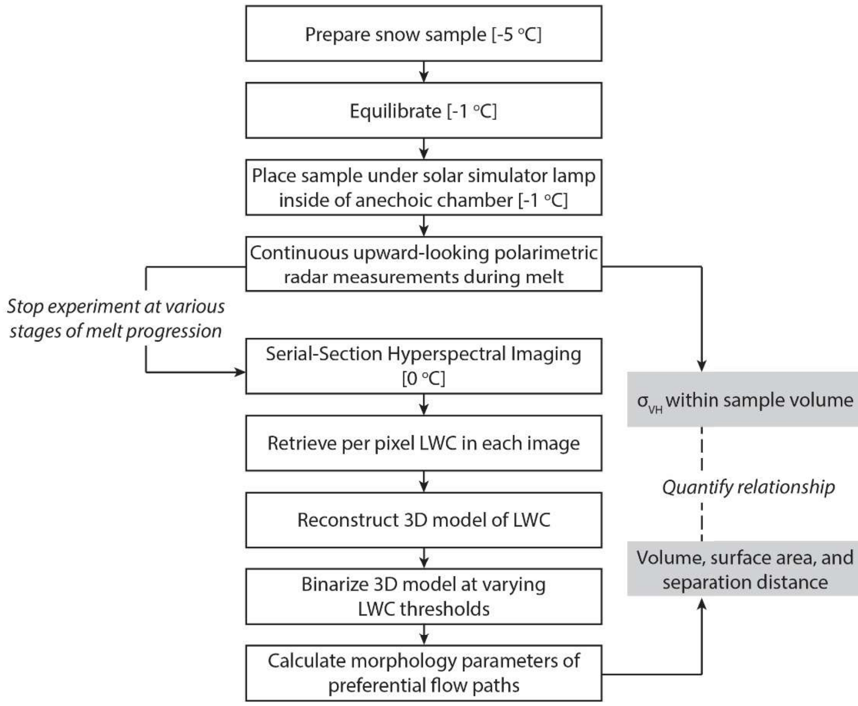

Figure 2. Laboratory experimental workflow

2.1 Snow sample preparation

Laboratory snow samples were prepared inside of a polystyrene foam container, commonly referred to as Styrofoam, because it is nearly invisible to the radar due to its low relative permittivity (ε_r = 1.1). The 42 x 42 x 38 cm (L x W x H) sample container was filled with clean rounded snow grains that were produced in a laboratory snow-maker, similar to the machine described in [24]. The produced snow was stored in a cold room at -10 °C for multiple weeks which allowed the dendritic crystals to metamorphose into rounded grains of varying size. Snow grains were sieved using a 2 mm sieve to create a single homogenous layer within the sample container. The bulk density of the samples, measured by weighing the entire sample, ranged from 370 to 497 kg m^{-3}. The top surface of each sample was scraped with a straight edge to level the snow surface with the top of the sample container. To mitigate edge effects from water flowing down the sides of the sample container along the side walls, the top of the snow sample was shaded along the edge using a piece of polystyrene foam extending 2.5 cm from the sample container side wall. The details for each snow sample are outlined in Table 1.

Table 1. Snow sample properties

Snow Sample	Density [kg m^{-3}]	Time under solar lamp [min]
1	497	20
2	489	30
3	370	60
4	399	120
5	479	50
6	378	40

2.2 Radar experimental setup and raw data processing

To reduce radar reflections from the walls inside the cold room, each snow sample was placed inside of a custom-built anechoic chamber, represented in Figure 3. The frame of the anechoic chamber was built with plywood, to dimensions of 95 x 95 x 200 cm (L x W x H), and the interior walls were lined with 7.6 cm thick convoluted foam absorbers (Mast Technologies MF32-0002-01) designed to attenuate microwaves at frequencies ranging from 1 GHz to 18 GHz. The top of the anechoic chamber was left open, and the chamber was located underneath a programmable metal-halide lamp that simulates the solar spectrum. The shortwave radiation flux of the lamp was set to 900 W m^{-2}, which is a flux commonly observed in the spring when seasonal snowpacks undergo melt [25]. Snow samples were placed in the center of the chamber, 41 cm below the solar lamp, on an integrated shelf built into the chamber. The radar was located at the base of the chamber with the antennas pointing upward 75 cm from the bottom of the snow sample.

This study used a SensorLogic (https://www.sensorlogic.ai/) Onza ultra-wideband (UWB) radar development kit, which integrates the Novelda XeThru X4 radar technology onto a BeagleBone Black compatible cape. The radar was configured to operate at a center frequency of 7.29 GHz (C-band) with a bandwidth of 1.5 GHz, such that the operating frequency range covered 6.54-8.04 GHz. The radar unit was configured in a quasi-monostatic configuration consisting of two linearly polarized 15 dBi gain horn antennas (WR-137) designed to operate between 5.85-8.20 GHz. The far field radiation pattern of the antennas, defined by the Fraunhofer distance [26], was 43 cm and the bottom of the snow sample was in this region. To collect four polarimetric measurements (VV, HH, VH, HV), the two antennas were mounted 11 cm apart on a custom-built stepper motor assembly that automatically rotated the antennas through precise 90^{o} rotations between each radar acquisition, such that the antennas were either parallel or orthogonal to each other. During the melt experiment, continuous radar measurements were made. At each antenna configuration, twenty radar traces were collected and averaged for that time step. Each polarization measurement and subsequent antenna rotation took 15 seconds, with all four polarizations collected in approximately 60 seconds.

Each melt experiment started with the snow sample isothermal at -1 ^{o}C, such that the snow sample was dry (i.e., no liquid water) and the cold content was nearly depleted. First, the radar was turned on to collect three full polarimetric measurements of the snow sample in the dry state. Next, the solar lamp was turned on to begin the melting process. By visual inspection of the real-time radar data, melt experiments were terminated at various stages of melt progression to get a set of samples that captured a range of preferential flow path sizes and patterns that could be compared to the radar signal.

Post-processing steps were identical for all radar traces. The received signal was normalized to an absolute voltage value between 0-1.2 V. To reduce noise, two processing steps were applied; (1) a background signal, taken without a snow sample in the anechoic chamber, was removed from each radar trace in the frequency domain and (2) a bandpass filter spanning the frequency range of the radar (5.65-8.04 GHz) was used to remove high and low frequency noise [27]. Following the processing steps used in [14], a linear-time varying gain was applied to signals to enhance the upper regions of the snow sample that were impacted by radar range loss. For visualization in a radargram format, the processed signal was enveloped using a Hilbert transform [28].

Using a simplified form of the snow radar backscatter model [29], the total radar backscatter received at the antenna for each transmit-receive polarizations p and q (σ_{pq}^{tot}) was decomposed into three components:

$$\sigma_{pq}^{tot} = \sigma_{pq}^{top} + \sigma_{pq}^{vol} + \sigma_{pq}^{bot}, \tag{1}$$

where σ_{pq}^{top} is the backscatter at the air-snow interface at the top of the snow sample, σ_{pq}^{vol} is the backscatter from the snow volume, and σ_{pq}^{bot} is the backscatter at the polystyrene foam-snow interface at the bottom of the snow sample. Of particular interest in this study was σ_{VH}^{vol} because the preferential flow paths develop within the snow volume. To calculate σ_{VH}^{vol}, the magnitude of the radar signal was integrated over range bins (i.e., fast time) that represented the snow volume. Using the strong co-polarized returns from the top and bottom of the snow samples, the limits of the range bins were selected by picking the signal minima following the top and bottom snow surface reflections. Due to the six snow samples having variations in bulk density (370-497 kg m-3), this methodology resulted in the number of range bins to vary by approximately 2 cm (43-47 total range bins) between samples. To not introduce a bias due to the total number of range bins that were integrated, the smallest number of range bins (43 range bins) was used for all samples. In the denser samples, where the number of range bins were larger, the volume range was centered in the middle of the volume, which resulted in at most 2 bins (~1 cm) being excluded on each end.

The characterization of preferential flow paths using the serial-section hyperspectral imaging method, discussed further is section 2.3, only captured the approximate state of the preferential flow paths within the snow volume at the final time step of the continuous radar measurements. Hence, the primary radar parameter used for comparison to the morphology parameters was σ_{VH}^{vol} calculated at the final timestep of the continuous radar measurements, denoted as $(\sigma_{VH}^{vol})_{t=end}$. Since there were no continuous quantifiable preferential flow morphology parameters that could be collected during the melt experiment, the radar data prior to the final time step could only be qualitatively assessed against the final state of the preferential flow paths.

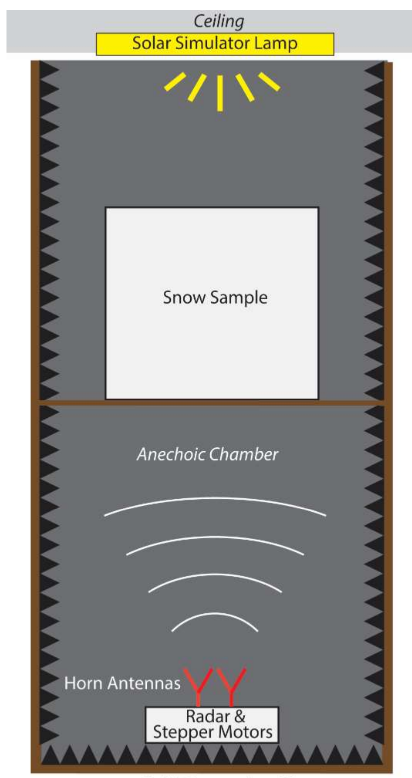

Figure 3. Schematic of laboratory snow melt experiments within an anechoic chamber inside of a cold room with continuous upward-looking polarimetric radar measurements.

2.3 Serial-section hyperspectral imaging and data cube processing

For 3D visualization and quantification of preferential flow paths within the snow volume, each sample was serial-section imaged using a compact hyperspectral imager (Figure 4a). Inside the cold room, set at 0 °C, the sidewalls of the sample container were removed to expose the snow sample. The sample was cut along the vertical profile in ~1.5 cm intervals using a sharpened piece of aluminum sheet metal (60 x 60 cm) that extended beyond the edges of the sample. Following each cut, the snow sample was moved ~1.5 cm towards the imager to maintain a consistent distance between the snow surface and the imager, which maintained a consistent pixel resolution for each image. Each sample was serial-sectioned into 28-33 sections. Following the experimental setup detailed in [30] and briefly described here, each exposed face was illuminated using two diffuse halogen lamps. A Resonon Pika NIR-320 hyperspectral imager was mounted onto a tripod mounted rotational stage to collect the NIR spectral radiance in each pixel from 900-1700 nm. A Spectrolon® 99% reflectance calibration target was placed in the scene of each image to convert each pixel from radiance to bidirectional reflectance.

Following the methodology detailed in [23], the spectral shift in NIR reflectance between ice and liquid water was leveraged to retrieve volumetric LWC on a pixel-by-pixel basis (1.3 mm pixel resolution). Each image contained 315 x 285 (W x H) pixels with LWC values ranging from 0-25 % LWC and the stack of images was reconstructed into a 3D model with each voxel representing the LWC in the snow sample (Figure 4b). The high pixel resolution in the imaging/cutting plane (x-y, Figure 4) was maintained and each image in the stack was stretched in the cutting direction (z, Figure 4) to represent ~1.5 cm, resulting in a 3D model containing 315 x 315 x 285 voxels (L x W x H) having a 2.4 mm^3 resolution. A 3D box filter [31], with a filter size of 9, was used to make the edges between voxels continuously smooth.

Within the 3D model, a smaller volume of interest (VOI, gray volume in Figure 4c) was extracted that contained only the preferential flow paths inside the volume of the snow sample and was used to quantify morphology parameters for comparison to the radar signal, discussed further in section 2.4. In order to only evaluate the contribution from the preferential flow paths, the VOI excluded the top 3.5 cm that included the matrix flow, the bottom 2 cm that included pooling water at the bottom of the samples, and 3.5 cm from the snow sample edge to remove edge effects. The same VOI dimensions were used for all samples, which contained 245 x 262 x 262 voxels.

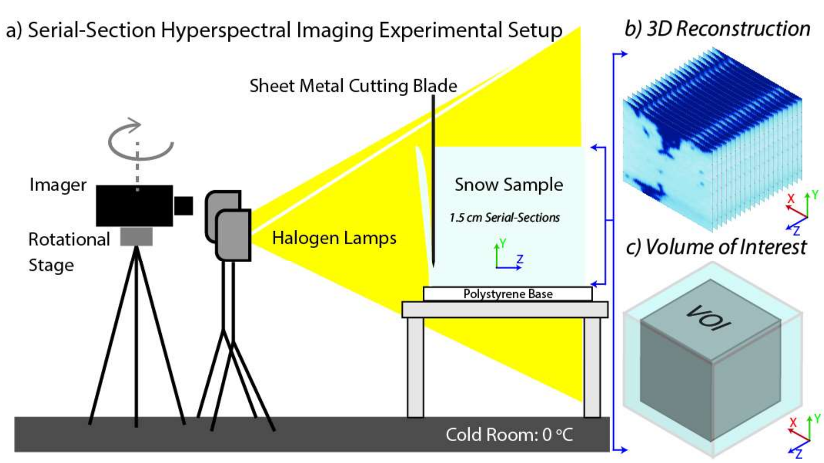

Figure 4. a) Schematic of serial-section hyperspectral imaging experimental setup inside of cold room. b) Visualization of a stack of serial-section images reconstructed to represent the 3D distribution of liquid water content in the snow sample. c) Schematic of the entire volume of the reconstructed snow sample (light blue) and the volume of interest (VOI, gray) within the snow sample volume.

2.4 Preferential flow morphology

The preferential flow path morphology within the VOI was used as a comparison to $(\sigma_{VH}^{vol})_{t=end}$. To calculate morphology parameters, the 3D LWC model must be in a binarized form, such that the preferential flow paths are represented as objects. Using a LWC threshold, the 3D structure was binarized into an object at 1% steps ranging from 0% to 7% LWC. At a 0% LWC threshold, all voxels were included as part of the object which resulted in a cube the size of the VOI (Figure 5a). As the threshold is step-wise increased, all voxels containing LWC values less than the threshold were removed from the object and the preferential flow paths, having higher LWC values, were revealed. For example, in Figure 5b-d, the threshold is increased from 2-6% LWC and with each threshold increase the preferential flow path becomes more defined.

Morphology parameters were calculated using the Bruker CT Analyzer (CTAN) software package, an X-ray computed microtomography (micro-CT) 3D image analysis software. The 2D binarized image stacks were loaded into the program and 3D morphology parameters were computed for each sample at each threshold. The morphology analysis focused on three parameters that quantitatively describe the structure of the preferential flow paths: (1) object volume, (2) object surface area, and (3) object separation distance. Object separation is a measure of the mean thickness of open space or cavities that separates the object structures, which is determined by fitting spheres within the open space [32].

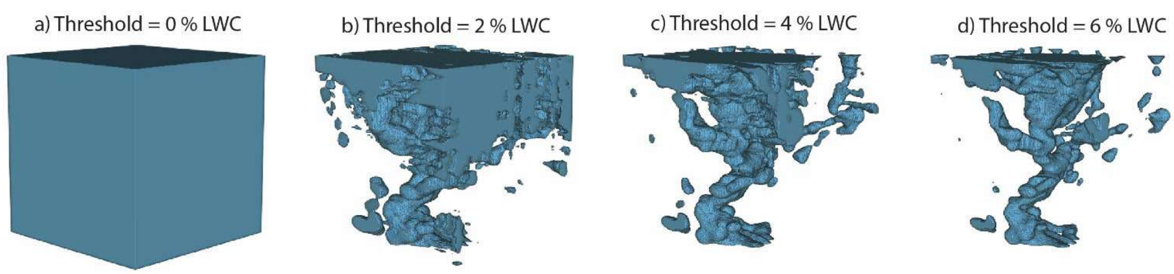

Figure 5. An example (Sample 6) of binarizing the volume of interest (VOI) using a liquid water content (LWC) threshold equal to a) 0% b) 2% c) 4% and d) 6%.

3. Results

3.1 Upward-looking radar observations

The continuous radar measurements for σ_{VV} and σ_{VH} are presented in radargrams for each snow sample in columns one and two of Figure 6, respectively, and it is worth noting that the color scale for σ_{VV} is an order of magnitude greater than σ_{VH}. The snow samples are ordered (1-6) in increasing magnitude of $(\sigma_{VH}^{vol})_{t=end}$, which are shown in Table 2, and does not consistently correspond to the duration of each experiment. The red tick marks indicate the location of the peak backscatter from the top (σ^{top}) and bottom (σ^{bot}) of the snow samples and the region between the white tick marks represents the limits of the range bins that were integrated to compute the backscatter within the sample volume (σ^{vol}). Although σ_{HH} and σ_{HV} were also collected, they are not presented here because they were nearly identical to σ_{VV} and σ_{VH}, given the radar was in an orthogonal orientation relative to the snow sample.

Generally, and as expected, σ_{VV} captured single bounce reflections from surfaces that were perpendicular to the antennas, which were the top and bottom surfaces of the snow sample and pooling layers of water. At the start of the experiments when the snow was dry, σ_{VV} detected the top and bottom of the snow sample, with negligible returns within the snow volume (Figure 6, column one). In all samples, melt initiated at the top snow surface at approximately 10 minutes, which caused σ_{VV}^{top} to increase due to the introduction of water increasing ε_r. As melt progresses and water began to percolate through the snow volume, σ_{VV}^{top} generally began to decrease. In Samples 1-3, σ_{VV}^{vol} remained negligible across the duration of each experiment, suggesting there were no single bounce returns from preferential flow paths, while Samples 4-6 exhibited measurable returns at late stages of the experiment. This is discussed in terms of preferential flow path morphology in section 4.2. For comparison, $(\sigma_{VH}^{vol})_{t=end}$ and $(\sigma_{VV}^{vol})_{t=end}$ are summarized in Table 2.

In comparison to σ_{VV}, σ_{VH} had relatively low magnitude returns at top and bottom surfaces in dry conditions, which were not present in all samples (e.g., Samples 4-5 at 0 minutes). Additionally, σ_{VH}^{vol} had measurable returns, whereas σ_{VV}^{vol} did not. As the top of the sample began to melt, as seen in σ_{VV}^{top}, σ_{VH}^{top} also increased, although the returns were time-delayed compared to σ_{VV}^{top}, which was likely due to the returned EM waves being multiple scattered by irregularities in the wet surface. Interestingly, exhibited in all samples at the snow surface and discussed further in section 4.1, there are periods where σ_{VV}^{top} faded while σ_{VH}^{top} enhanced. As melt progressed further, σ_{VH}^{vol} enhanced and appeared to track water movement within the snow sample, which supports the hypothesis that the heterogenous nature of preferential flow paths has a depolarizing effect on incident EM waves.

Table 2. Integrated co- and cross-polarized backscatter within the snow sample volume at the final time step of the melt experiment.

Snow Sample	$(\sigma_{VV}^{vol})_{t=end}$ [dB]	$(\sigma_{VH}^{vol})_{t=end}$ [dB]
1	-0.1	-12.6
2	6.3	-12.3
3	9.8	-5.1
4	8.1	-2.2
5	13.1	0.2
6	14.6	0.5

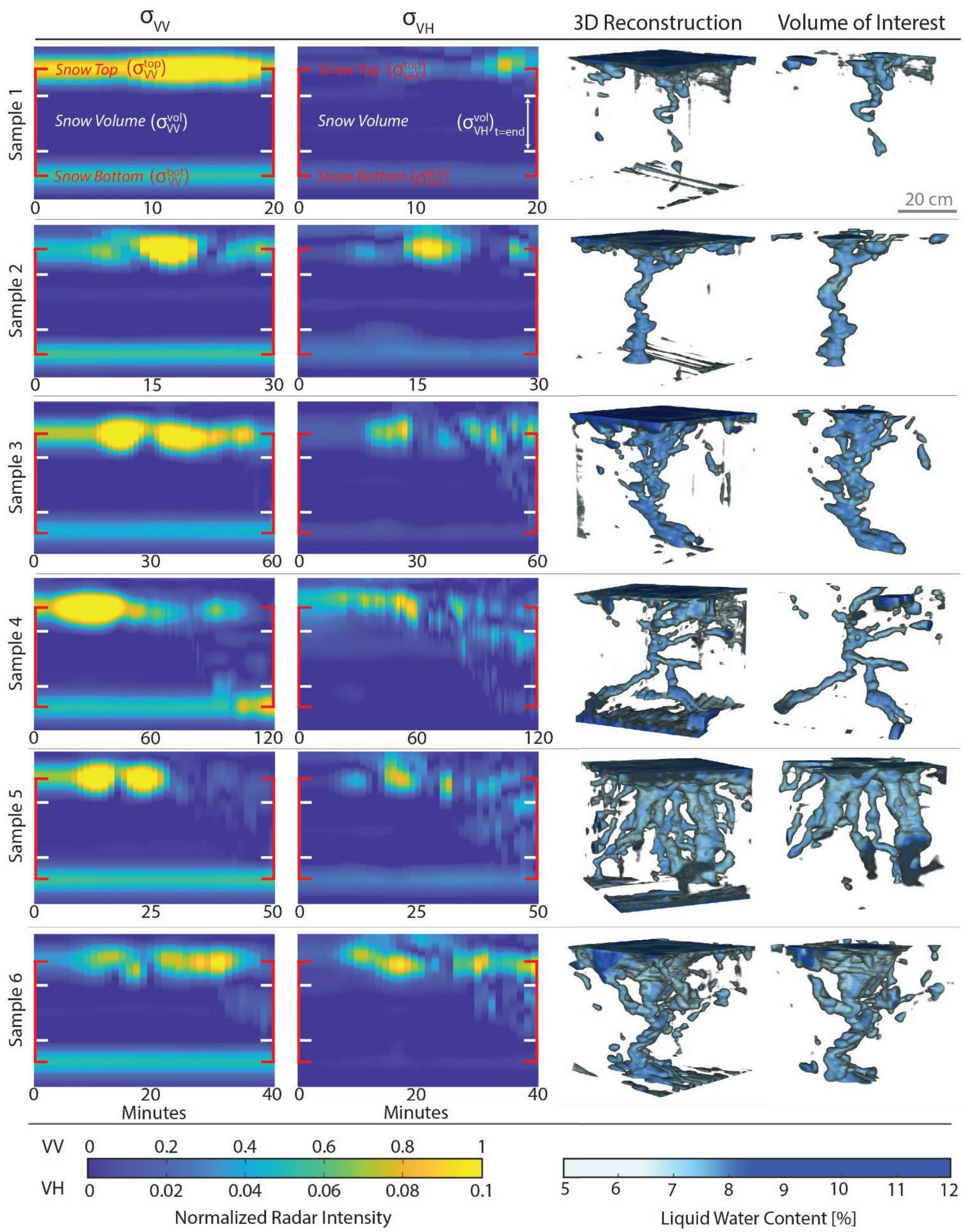

Figure 6. The first two columns are the continuous co-polarized and cross-polarized radargram for each melt experiment (Samples 1-6). The snow sample top and bottom are indicated with the red tick marks and the snow sample volume is represented as the area between the white tick marks. The second two columns are the corresponding 3D reconstruction and volume of interest with the liquid water content threshold set to 5%.

3.2 Liquid water content 3D reconstructions

The 3D LWC reconstructions, shown in Figure 6 (third column), show the main features of water movement through the snow sample. The structures are shown with a 5% LWC threshold; all voxels with LWC <5% are transparent, and the remaining voxels LWC values are indicated using the color scale. Generally, all samples had a similar structure including homogenous matrix flow at the top of the snow surface, preferential flow paths in the snow volume, and varying amounts of pooling water at the bottom of the sample container.

Example VOIs, the portion of the sample used to characterize the structure, are also shown in Figure 6 (fourth column). The VOIs retain the preferential flow path structure, while removing the pooling water at the surface and base of the sample and edge effects. By visual inspection, the preferential flow paths from Sample 1 to 6 were progressively more complex, which generally coincided with the sample ordering based on increasing $(\sigma_{VH}^{vol})_{t=end}$. This result suggests that σ_{VH}^{vol} was sensitive to the development of the preferential flow path prior to the final time step of the melting experiments, because σ_{VH}^{vol} appears to correspond with the timing of water percolation in the snow volume.

3.3 Preferential flow path morphology

In combination, the 3D LWC models and radar data indicate that the development of preferential flow paths creates opportunities for multiple scattering, increasing σ_{VH}^{vol}. Preferential flow path morphology, characterized by volume, surface area, and separation distance, exhibited linear relationships with $(\sigma_{VH}^{vol})_{t=end}$ at LWC thresholds between 4–7%. At the lower thresholds (1-3%) the flow path structures were not fully resolved, see Figure 5a-b, and R-squared values were low (Table 3). Overall, the morphology parameters had the best fit (R-squared) at 5% LWC threshold, which is represented in blue in Figure 7 and used to visualize the 3D structure in Figure 5.

As shown in Figure 7, preferential flow volume and surface area had positive trends with $(\sigma_{VH}^{vol})_{t=end}$, which makes intuitive sense because as more preferential flow paths were developed the likelihood of multiple scattering increased. The preferential flow path separation distance had a negative trend with $(\sigma_{VH}^{vol})_{t=end}$, which indicates that structures close together have higher likelihood of causing multiple scattering while structures farther away are less likely to cause multiple scattering and subsequent depolarization. At each threshold, volume and surface area have similar trendlines, but shift to smaller values as the threshold is increased and more of the object is removed. The trendlines for separation distance are similar but shift to larger separation distances at higher thresholds due to more of the object being removed.

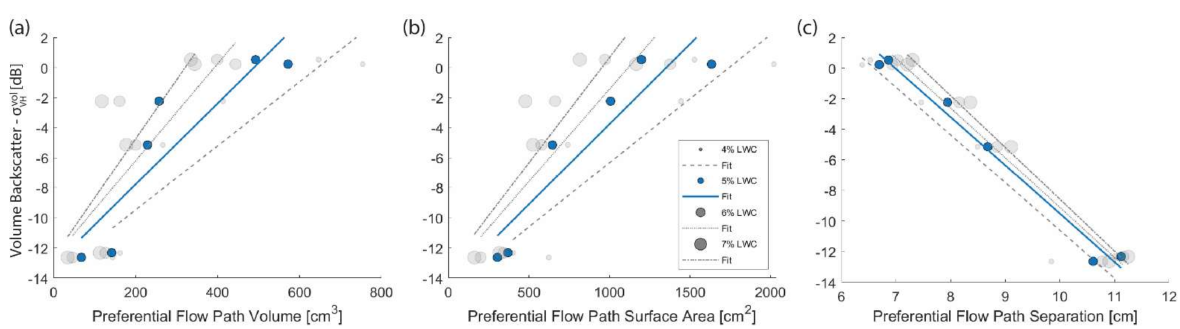

Figure 7. Morphology parameters (a) preferential flow path volume, (b) preferential flow path surface area, and (c) preferential flow path separation distance derived at liquid water content (%LWC) thresholds ranging from 4-7% and plotted versus the cross-polarized volume component from the final timestep in the melt experiment, $(\sigma_{VH}^{vol})_{t=end}$.

Table 3. Coefficient of determination (R-squared) between the morphology parameters at each liquid water content (LWC) threshold and the cross-polarized volume component at the final timestep in the melt experiment, $(\sigma_{VH}^{vol})_{t=end}$. Bold values indicate LWC thresholds that are included in Figure 7.

LWC Threshold [%]	Volume	Surface Area	Separation Distance
1	0.31	0.27	0.46
2	0.51	0.35	0.61
3	0.76	0.60	0.74
4	**0.84**	**0.82**	**0.95**
5	**0.81**	**0.86**	**0.98**
6	**0.74**	**0.79**	**0.99**
7	**0.70**	**0.73**	**0.99**

4. Discussion

4.1 Radar response from the top of the snow sample

Due to melt initiation, there is a strong σ_{VV}^{top} exhibited in all snow samples, which was followed by a period during which σ_{VV}^{top} weakened while σ_{VH}^{top} coincidentally strengthened (Figure 6). In Samples 2-6, this period was then followed by σ_{VH}^{top} weakening while σ_{VV}^{top} strengthened again. To investigate the snow structure and LWC distribution that caused this radar response, the Sample 1 experiment was terminated within this period. Although it was challenging to determine the exact cause of this response, by visual inspection of the 3D LWC model in Sample 1, we hypothesize that this time coincides with the period where the top snow layer becomes sufficiently saturated to overcome capillary forces, and due to gravity begins to drain below the snow surface [33]. This process has two effects on the radar response: (1) the LWC at the snow surface is reduced, lowering ε_r, and therefore σ_{VV}^{top} and (2) the underside of the snow surface develops heterogenous distributions of water (Figure 6, Sample 1), similar to surface roughness, and the high variation in ε_r increases multiple scattering, strengthening σ_{VH}^{top}.

4.2 Radar response from the snow volume

Single bounce radar returns typically produce large magnitude peaks and are easy to classify, whereas cross-polarized returns due to multiple scattering within a volume can appear noisy and are challenging to interpret. The cross-polarized returns from the experiments presented here generally do not have large magnitude peaks, but rather display multiple low magnitude peaks over the volume region. The returns, though, appear to track the progression of melt toward the bottom of the sample. Although it was not possible to quantify the state of preferential flow path development within the snow volume during the continuous radar measurements, some qualitative explanations of the volume returns can be made based on the final 3D LWC model.

In Samples 1 and 2, σ_{VV}^{vol} and σ_{VH}^{vol} were both negligible, likely due to the preferential flow paths being relatively undeveloped (Sample 1) or in a simple columnar form with no complexities (Sample 2). In Sample 3, while there are negligible returns in σ_{VV}^{vol}, σ_{VH}^{vol} seemed to track the development of the preferential flow path, which was more complex than Sample 2. This sample is a good example of the cross-polarized radar response being sensitive to a complex preferential flow path while it went undetected in the co-polarized returns. In Sample 4, there were unique horizontal preferential flow path features that were not present in other samples, which seemed to be detected by σ_{VV}^{vol} and σ_{VH}^{vol}. Sample 5 had the greatest number of individual preferential flow paths that were spatially distributed in the sample volume, which caused a large σ_{VH}^{vol}, while σ_{VV}^{vol} was small. This result suggests that the spatially distributed preferential flow paths depolarized the incoming radar signal, while the cumulative radar cross-section was not large enough for single bounce returns (σ_{VV}^{vol}). In Sample 6, the returns from σ_{VV}^{vol} and σ_{VH}^{vol} visually look similar, which could be due to the relatively wide funnel shape that was created by the preferential flow paths that could cause single bounce and multiple scattering returns.

Although $(\sigma_{VV}^{vol})_{t=end}$ had a general increasing trend with preferential flow path complexity, similar to $(\sigma_{VH}^{vol})_{t=end}$ (Table 2), it would not be possible to solely use this signal to classify the returns as anything other than a horizontal layer of pooling water. Layers containing pooling water in the horizontal plane result in strong co-polar returns and negligible cross-polar returns. Conversely, preferential flow paths resulted in weak co-polar returns and strengthened the cross-polar returns (Figure 6); indicating that the combination of radar returns could be used to classify this process.

4.3 Uncertainties

4.3.1 Polarimetric radar measurements

In single antenna (mono-static) polarimetric radars, the system switches between channels to send and receive EM waves in different polarizations, which can introduce cross-talk and gain imbalances between polarization channels. To interpret the data held in polarimetric radar returns, these need to be corrected by using calibration targets because many analysis methods depend on magnitudes and ratios of each polarization [34]. Here, a quasi-monostatic configuration was used that consisted of two antennas wired to separate transmit and receive ports, which minimized cross-talk. Additionally, instead of switching between channels, this radar setup rotated one antenna 90° relative to the other, maintaining an identical gain between polarization measurements. Although a calibration target was not used here, the polarimetric measurements are relative to each other and still represent the polarimetric response observed during the snow melt experiments.

4.3.2 Serial-sectioning and 3D reconstruction

Generating the 3D LWC models from serial-section images introduces uncertainties in the spatial distribution of water. To generate the 3D model, each LWC map in the imaging plane (x-y axes in Figure 4) was stretched in the cutting direction (z-axis in Figure 4) to represent ~1.5 cm of depth in the model. This resulted in the resolution of LWC in x-y axes being 10x higher than in the z-axis, though it allowed for the high-resolution detail of mapped LWC to be maintained. This approach introduces uncertainty in LWC along the z-axis because the reconstruction assumes the images are representative of LWC across the 1.5 cm serial-sections. However, this is a reasonable approach because the penetration of NIR light into snow is approximately 1-2 cm [35].

Under laboratory conditions, the LWC retrieval from NIR hyperspectral imaging has an uncertainty of ~1% LWC by volume [23]. This level of uncertainty could impact the binarized morphology of the preferential flow paths delineated during LWC thresholding. The incremental threshold changes of 1% LWC, though, resulted in relatively minor changes to the morphology parameters. The exception to this was at the transition from 0% to 1% (dry to wet snow transition) where there was a large change in binarized morphology (Figure 5). Still, of most relevance to this analysis, the trendlines exhibited in the morphology parameters were maintained across thresholds ranging from 4-7%, which indicates that the radar response is dominated by areas of increased LWC.

4.3.3 Morphology analysis

The LWC thresholding method used in the morphology analysis simplifies the actual distribution of LWC in the sample, however, this process was necessary to quantify the preferential flow path morphology. By visual inspection, the preferential flow path morphology was well represented at thresholds between 4-7% LWC, which is where trends were found between $(\sigma_{VH}^{vol})_{t=end}$ and the morphology parameters. Although radars operating at C-band are sensitive to lower LWC values (1-3%), there were no morphology trends found, suggesting that larger quantities of water dominate the radar response compared to lower values.

4.4 Outlook for application in the field

Radar frequency plays a large role in the measured response from a snowpack. Previous field studies used an upward-looking GPR system, which operates at a lower frequency (0.9 GHz) compared to the C-band (7.29 GHz) radar used here. Due to the long wavelength (~33 cm), GPR systems can penetrate deeper into wet snow, but are less likely to scatter at features smaller than the wavelength. Although not investigated here, it is unlikely that preferential flow paths would cause a similar cross-polarized radar response for GPR. In comparison, C-band radar has a shallower penetration into wet snow, but the ~5 cm wavelength is more likely to scatter at smaller features, which is better suited for detecting preferential flow paths in the field.

Another important consideration for field applications is the complexity of a seasonal snowpack, which is not well represented by the homogenous single layer snow samples analyzed here. Seasonal snowpacks contain stratigraphic layers, ice crusts, and capillary barriers that can impede the vertical movement of water in a preferential flow path, causing pooling or horizontal diversion of water away from the upward-looking radar. The presence of pooling water causes strong single bounce reflections, which would predominately enhance σ_{VV}. Additionally, preferential flow paths would need to develop directly above the radar, making the probability of detection lower. Although there are challenges associated with field application, collection of polarimetric data in an upward-looking configuration could help classify more features within the snow volume, that would otherwise be misclassified or missed all together using a single polarization radar.

5. Conclusions

Under controlled laboratory conditions, snow samples were melted by a simulated solar lamp while being continuously measured with an upward-looking polarimetric radar. Six snow samples were analyzed that captured the progression of preferential flow path development with increasing complexity. Using a new hyperspectral serial-section imaging technique, preferential flow paths were characterized in 3D such that the morphology could be related to the cross-polarized radar signal. We found that:

i. Within a snow volume, the cross-polarized radar response from an upward-looking UWB (C-band) radar is sensitive to the development of preferential flow paths.
ii. A new serial-section hyperspectral imaging method, presented here for the first time, was able to quantify in high resolution the 3D LWC distribution and preferential flow morphology within a snow sample.
iii. Incremental increases in the development and complexity of the preferential flow paths (Samples 1-6), as defined by morphology parameters, resulted in an overall increase of 13.1 dB in $(\sigma_{VH}^{vol})_{t=end}$, which ranged from -12.6 to 0.5 dB.
iv. Preferential flow path morphology parameters, including object volume, object surface area, and object separation distance, exhibited linear trends with $(\sigma_{VH}^{vol})_{t=end}$ at LWC thresholds ranging from 4-7% LWC.

This work demonstrates that there is value in having both co-polarized and cross-polarized capabilities in an upward-looking radar installation. Co-polarized radar is only capable of capturing horizontal/perpendicular features in the snowpack, however structures in other orientations exist, such as preferential flow paths. Cross-polarized radar provides a supplementary dataset that can be used to better classify radar returns.

Author Contributions: Conceptualization, C.D. and K.H.; methodology, C.D.; software, C.D.; validation, C.D.; formal analysis, C.D.; investigation, C.D.; resources, K.H.; data curation, C.D.; writing—original draft preparation, C.D.; writing—review and editing, C.D. and K.H.; visualization, C.D.; supervision, K.H.; project administration, K.H.; funding acquisition, K.H. All authors have read and agreed to the published version of the manuscript.

Funding: This research was funded by NATIONAL AERONAUTICS AND SPACE ADMINISTRATION (NASA), grant number 80NSSC18K0822.

Data Availability Statement: Data available upon request from lead author.

Acknowledgments: The radar and hyperspectral imager used in this study were provided by SensorLogic and Dr. McKenzie Skiles, respectively. We would like to thank Dr. HP Marshall and Will Tidd for engaging in many conversations about radar. We would also like to thank Ladean McKittrick, McKenzie Skiles, Michael Dvorsak, Evan Schehrer, and Khristian Jones for their assistance in the laboratory. We acknowledge the use of the Subzero Research Laboratory in the Department of Civil Engineering at Montana State University.

Conflicts of Interest: The authors declare no conflict of interest.

References

1. Marsh, P. and M.K. Woo, Wetting front advance and freezing of meltwater within a snow cover: 1. Observations in the Canadian Arctic. Water Resources Research, 1984. 20(12): p. 1853-1864.
2. Webb, R., M.W. Williams, and T. Erickson, The spatial and temporal variability of meltwater flow paths: Insights from a grid of over 100 snow lysimeters. Water Resources Research, 2018. 54(2): p. 1146-1160.
3. Colbeck, S.C., Water flow through heterogeneous snow. Cold Regions Science and Technology, 1979. 1(1): p. 37-45.
4. Schneebeli, M., Development and stability of preferential flow paths in a layered snowpack. IAHS Publications-Series of Proceedings and Reports-Intern Assoc Hydrological Sciences, 1995. 228: p. 89-96.
5. Eiriksson, D., et al., An evaluation of the hydrologic relevance of lateral flow in snow at hillslope and catchment scales. Hydrological Processes, 2013. 27(5): p. 640-654.
6. Perla, R.I. and M. Martinelli, Avalanche handbook. 1976: US Department of Agriculture, Forest Service.
7. Williams, M.W., T.A. Erickson, and J.L. Petrzelka, Visualizing meltwater flow through snow at the centimetre-to-metre scale using a snow guillotine. Hydrological Processes, 2010. 24(15): p. 2098-2110.
8. Webb, R.W., S.R. Fassnacht, and M.N. Gooseff, Hydrologic flow path development varies by aspect during spring snowmelt in complex subalpine terrain. The Cryosphere, 2018. 12(1): p. 287-300.
9. Marshall, H.-P. and G. Koh, FMCW radars for snow research. Cold Regions Science and Technology, 2008. 52(2): p. 118-131.
10. Marshall, H.P., G. Koh, and R.R. Forster, Ground-based frequency-modulated continuous wave radar measurements in wet and dry snowpacks, Colorado, USA: an analysis and summary of the 2002–03 NASA CLPX data. Hydrological Processes, 2004. 18(18): p. 3609-3622.
11. Albert, M., G. Koh, and F. Perron, Radar investigations of melt pathways in a natural snowpack. Hydrological processes, 1999. 13(18): p. 2991-3000.
12. Mitterer, C., et al., Upward-looking ground-penetrating radar for measuring wet-snow properties. Cold Regions Science and Technology, 2011. 69(2-3): p. 129-138.
13. Gubler, H. and M. Hiller, The use of microwave FMCW radar in snow and avalanche research. Cold Regions Science and Technology, 1984. 9(2): p. 109-119.
14. Heilig, A., M. Schneebeli, and O. Eisen, Upward-looking ground-penetrating radar for monitoring snowpack stratigraphy. Cold Regions Science and Technology, 2009. 59(2): p. 152-162.
15. Schmid, L., et al., Continuous snowpack monitoring using upward-looking ground-penetrating radar technology. Journal of Glaciology, 2014. 60(221): p. 509-525.
16. Heilig, A., et al., Seasonal and diurnal cycles of liquid water in snow—Measurements and modeling. Journal of Geophysical Research: Earth Surface, 2015. 120(10): p. 2139-2154.
17. Heilig, A., O. Eisen, and M. Schneebeli, Temporal observations of a seasonal snowpack using upward-looking GPR. Hydrological Processes, 2010. 24(22): p. 3133-3145.
18. Okorn, R., et al., Upward-looking L-band FMCW radar for snow cover monitoring. Cold Regions Science and Technology, 2014. 103: p. 31-40.
19. Lee, J.-S. and E. Pottier, Polarimetric radar imaging: from basics to applications. 2017: CRC press.
20. Cloude, S., Polarisation: applications in remote sensing. 2009: OUP Oxford.
21. Matzler, C., Microwave permittivity of dry snow. IEEE Transactions on Geoscience and Remote Sensing, 1996. 34(2): p. 573-581.
22. Archer, D.G. and P. Wang, The dielectric constant of water and Debye-Hückel limiting law slopes. Journal of physical and chemical reference data, 1990. 19(2): p. 371-411.
23. Donahue, C., S.M. Skiles, and K. Hammonds, Mapping liquid water content in snow at the millimeter scale: an intercomparison of mixed-phase optical property models using hyperspectral imaging and in situ measurements. The Cryosphere, 2022. 16(1): p. 43-59.
24. Schleef, S., et al., An improved machine to produce nature-identical snow in the laboratory. Journal of Glaciology, 2014. 60(219): p. 94-102.

25. Skiles, S.M. and T. Painter, Daily evolution in dust and black carbon content, snow grain size, and snow albedo during snowmelt, Rocky Mountains, Colorado. Journal of Glaciology, 2017. 63(237): p. 118-132.
26. Walter, C.H., Traveling wave antennas. 1970: New York: Dover Publications.
27. Shenoi, B.A., Introduction to digital signal processing and filter design. 2005: John Wiley & Sons.
28. Bracewell, R.N., The Fourier transform and its applications. Vol. 31999. 1986: McGraw-hill New York.
29. Ulaby, F.T., Microwave remote sensing active and passive. Rader remote sensing and surface scattering and emission theory, 1982: p. 848-902.
30. Donahue, C., S.M. Skiles, and K. Hammonds, In situ effective snow grain size mapping using a compact hyperspectral imager. Journal of Glaciology, 2021. 67(261): p. 49-57.
31. MathWorks, Image Processing Toolbox Reference. 2022, The MathWorks, Inc. p. 1397-1399.
32. Hildebrand, T. and P. Rüegsegger, A new method for the model-independent assessment of thickness in three-dimensional images. Journal of microscopy, 1997. 185(1): p. 67-75.
33. Colbeck, S., A theory of water percolation in snow. Journal of glaciology, 1972. 11(63): p. 369-385.
34. Sarabandi, K. and F.T. Ulaby, A convenient technique for polarimetric calibration of single-antenna radar systems. IEEE Transactions on Geoscience and Remote Sensing, 1990. 28(6): p. 1022-1033.
35. Nolin, A.W. and J. Dozier, A Hyperspectral Method for Remotely Sensing the Grain Size of Snow. Remote Sensing of Environment, 2000. 74(2): p. 207-216.

CHAPTER FIVE

CONCLUSIONS AND FUTURE OUTLOOK

The work presented in this dissertation demonstrates the utility of developing remote sensing methods and assessing the accuracy of snow property retrievals in a controlled laboratory environment to support larger scale remote sensing studies. For example, the effective snow grain size retrieval presented in Chapter 2 was near-coincidently assessed against precise snow microstructure measurements from micro-CT. Due to sample casting and transport difficulties, this cannot easily be performed on field snow samples. Similarly, previous case studies had demonstrated LWC retrievals from measured and simulated spectral reflectance, however the accuracy and optimal wet snow radiative transfer simulation approach could not be determined in the field. Using the systematic laboratory approach presented in Chapter 3, snow melt conditions were controlled while in situ LWC measurements were taken, which was used to generate a large dataset, such that the optimal wet snow radiative transfer inversion approach for retrieving LWC could be determined.

In terms of upward-looking radar, the laboratory allowed for multiple melt experiments, whereas field applications require burying the radar underneath the snowpack and limits the dataset to a single melt season. Additionally, the state of the snowpack cannot be characterized in the detail obtained in the laboratory. The laboratory upward-looking radar experiments presented in Chapter 4 were stopped at various stages of melt to characterize the state of the snow sample for radar interpretation and multiple situations could be assessed relatively quickly. Although laboratory remote sensing experiments are at a small scale, the remote sensing instrument response to specific snow conditions directly translates to larger scales.

While developing and assessing remote sensing instruments in the laboratory has advantages, there remain limitations and precautions that should be considered. For instance, optical remote sensing in the laboratory simplifies actual solar illumination conditions found in the field, where direct and diffuse light need to be accounted for. Additionally, scattering in the atmosphere is neglected in the laboratory, whereas atmospheric corrections are needed to get accurate field reflectance data. In terms of radar remote sensing, the complexities of a natural heterogenous snowpack, which impact radar volume scattering, cannot be well represented in prepared laboratory snow samples. For example, a natural seasonal snowpack contains multiple stratigraphy layers, which have large horizontal and vertical spatial variations in snow grain size, grain shape, crusts, ice lenses, and LWC that likely collectively play a role in the volume scattering component. Smaller laboratory snow samples, on the other hand, are prepared by sieving snow into a container in an attempt to mimic a natural snowpack, but typically only capture a subset of the complexities found in a natural snowpack.

For future work, the remote sensing methods developed in the laboratory and presented in this dissertation should be evaluated further for field applications. The hyperspectral imaging retrieval methods presented in Chapters 2 and 3 were tested in the field by imaging a vertical profile of a snowpit sidewall, but another obvious extension of this work would be to mount the imager to an uncrewed aerial vehicle (UAV) to map surface snow properties. High resolution grain size and LWC maps at the hillslope to watershed scales could be used to investigate topography impacts on albedo and LWC distribution. This could be useful for ground truthing coarser-scale satellite remote sensing retrievals because a single flight can map spatial variability across satellite pixels, supplementing or replacing current methods that compare to point measurements (e.g., Bair and others, 2019).

The polarimetric upward-looking radar and 3D LWC retrieval datasets, presented in Chapter 4, could be used in the future to test 2D and 3D water infiltration models (Hirashima and others, 2014, Hirashima and others, 2017). The experimental datasets consist of a characterized initial effective grain size distribution, continuous snowmelt timing from the radar measurements, and the final state of 3D LWC distribution from the hyperspectral imager, which are critical parameters for initializing and analyzing the results of these types of models. Additional experiments using this established methodology could be conducted to test the model against more complex stratigraphic layers including crusts and capillary barriers. Polarimetric radar in an upward-looking configuration should also be tested in the field in future studies to investigate the effects from complex and heterogenous stratigraphic layering in a natural snowpack.

In addition to demonstrating the value of method development in a controlled laboratory, the work presented in Chapter 4 highlights the utility of using a multi-sensor fusion approach to snow remote sensing. Remote sensing instruments, passive and active, operate at specific frequency ranges that have characteristic responses to physical properties in a snowpack, each of which have unique advantages and disadvantages. Recognizing this, the multiyear NASA SnowEx campaign aims to characterize the performance of multiple sensors and to identify synergies between them to find the optimal suite of sensors for global snow cover monitoring at the satellite-borne scale (Durand and others, 2019). Fusing data products from optical and radar remote sensing methods provide surface properties, that are critical for snow melt timing, and volumetric properties, that are critical for SWE and LWC estimates, which combined are critical for monitoring and forecasting water resources held in the form of snow.

REFERENCES CITED

A2 Photonic Sensors 2019. WISe - Snow liquid water content sensor - User Manual.

Albert, M., G. Koh and F. Perron 1999. Radar investigations of melt pathways in a natural snowpack. *Hydrological processes*, **13**(18): 2991-3000.

Ambach, W. and A. Denoth 1980. The dielectric behaviour of snow: a study versus liquid water content.

Archer, D.G. and P. Wang 1990. The dielectric constant of water and Debye-Hückel limiting law slopes. *Journal of physical and chemical reference data*, **19**(2): 371-411.

Arnaud, L., G. Picard, N. Champollion, F. Domine, J. Gallet, E. Lefebvre, M. Fily and J. Barnola 2011. Measurement of vertical profiles of snow specific surface area with a 1 cm resolution using infrared reflectance: instrument description and validation. *Journal of Glaciology*, **57**(201): 17-29.

Avanzi, F., H. Hirashima, S. Yamaguchi, T. Katsushima and C.D. Michele 2016. Observations of capillary barriers and preferential flow in layered snow during cold laboratory experiments. *The Cryosphere*, **10**(5): 2013-2026.

Avanzi, F., G. Petrucci, M. Matzl, M. Schneebeli and C. De Michele 2017. Early formation of preferential flow in a homogeneous snowpack observed by micro-CT. *Water Resources Research*, **53**(5): 3713-3729.

Bair, E., T. Stillinger, K. Rittger and M. Skiles 2021. COVID-19 lockdowns show reduced pollution on snow and ice in the Indus River Basin. *Proceedings of the National Academy of Sciences*, **118**(18).

Bair, E.H., K. Rittger, S.M. Skiles and J. Dozier 2019. An examination of snow albedo estimates from MODIS and their impact on snow water equivalent reconstruction. *Water Resources Research*, **55**(9): 7826-7842.

Bales, R.C., N.P. Molotch, T.H. Painter, M.D. Dettinger, R. Rice and J. Dozier 2006. Mountain hydrology of the western United States. *Water Resources Research*, **42**(8).

Barnett, T.P., J.C. Adam and D.P. Lettenmaier 2005. Potential impacts of a warming climate on water availability in snow-dominated regions. *Nature*, **438**(7066): 303-309.

Bohren, C.F. and R.L. Beschta 1979. Snowpack albedo and snow density. *Cold Regions Science and Technology*, **1**(1): 47-50.

Bohren, C.F. and D.R. Huffman 2008. *Absorption and scattering of light by small particles.* John Wiley & Sons.

Bracewell, R.N. 1986. *The Fourier transform and its applications.* McGraw-hill New York.

Brucker, L., G. Picard, L. Arnaud, J.-M. Barnola, M. Schneebeli, H. Brunjail, E. Lefebvre and M. Fily 2011. Modeling time series of microwave brightness temperature at Dome C, Antarctica, using vertically resolved snow temperature and microstructure measurements. *Journal of Glaciology*, **57**(201): 171-182.

Cloude, S. 2009. *Polarisation: applications in remote sensing.* OUP Oxford.

Colbeck, S. 1972. A theory of water percolation in snow. *Journal of glaciology*, **11**(63): 369-385.

Colbeck, S. 1979a. Grain clusters in wet snow. *Journal of Colloid and Interface Science*, **72**(3): 371-384.

Colbeck, S.C. 1979b. Water flow through heterogeneous snow. *Cold Regions Science and Technology*, **1**(1): 37-45.

Colbeck, S.C. 1982. An overview of seasonal snow metamorphism. *Reviews of Geophysics*, **20**(1): 45-61.

Colbeck, S.C. 1991. The layered character of snow covers. *Reviews of Geophysics*, **29**(1): 81-96.

Conway, H. and C.F. Raymond 1993. Snow stability during rain. *Journal of Glaciology*, **39**(133): 635-642.

Davis, R.E., J. Dozier, E.R. LaChapelle and R. Perla 1985. Field and laboratory measurements of snow liquid water by dilution. *Water Resources Research*, **21**(9): 1415-1420.

Davis, R.E., A.W. Nolin, R. Jordan and J. Dozier 1993. Towards predicting temporal changes of the spectral signature of snow in visible and near-infrared wavelengths. *Annals of Glaciology*, **17**: 143-148.

Denoth, A. 1994. An electronic device for long-term snow wetness recording. *Annals of Glaciology*, **19**: 104-106.

Denoth, A., A. Foglar, P. Weiland, C. Mätzler, H. Aebischer, M. Tiuri and A. Sihvola 1984. A comparative study of instruments for measuring the liquid water content of snow. *Journal of Applied Physics*, **56**(7): 2154-2160.

DeWalle, D.R. and A. Rango 2008. *Principles of snow hydrology.* Cambridge University Press.

Donahue, C., S.M. Skiles and K. Hammonds 2021. In situ effective snow grain size mapping using a compact hyperspectral imager. *Journal of Glaciology*, **67**(261): 49-57.

Donahue, C., S.M. Skiles and K. Hammonds 2022. Mapping liquid water content in snow at the millimeter scale: an intercomparison of mixed-phase optical property models using hyperspectral imaging and in situ measurements. *The Cryosphere*, **16**(1): 43-59.

Dozier, J. and T.H. Painter 2004. Multispectral and hyperspectral remote sensing of alpine snow properties. *Annual Review of Earth and Planetary Sciences*, **32**.

Dumont, M., O. Brissaud, G. Picard, B. Schmitt, J.-C. Gallet and Y. Arnaud 2010. High-accuracy measurements of snow Bidirectional Reflectance Distribution Function at visible and NIR wavelengths-comparison with modelling results.

Durand, M., C. Gatebe, E. Kim, N. Molotch, T. Painter, M. Raleigh, M. Sandells and C. Vuyovich 2019. NASA SnowEx Science Plan: Assessing approaches for measuring water in Earth's seasonal snow, Version 1.6. *National Aeronautics and Space Administration (NASA): Washington, DC, USA*.

Eiriksson, D., M. Whitson, C.H. Luce, H.P. Marshall, J. Bradford, S.G. Benner, T. Black, H. Hetrick and J.P. McNamara 2013. An evaluation of the hydrologic relevance of lateral flow in snow at hillslope and catchment scales. *Hydrological Processes*, **27**(5): 640-654.

Ellerbruch, D. and H. Boyne 1980. Snow stratigraphy and water equivalence measured with an active microwave system. *Journal of Glaciology*, **26**(94): 225-233.

Fierz, C., Armstrong, R.L., Durand, Y., Etchevers, P., Greene, E., McClung, D.M., Nishimura, K., Satyawali, P.K., Sokratov, S.A. 2009. The International classification for seasonal snow on the ground. *International Association of Cryospheric Sciences*.

Flanner, M.G. and C.S. Zender 2005. Snowpack radiative heating: Influence on Tibetan Plateau climate. *Geophysical Research Letters*, **32**(6).

Flanner, M.G., C.S. Zender, J.T. Randerson and P.J. Rasch 2007. Present-day climate forcing and response from black carbon in snow. *Journal of Geophysical Research: Atmospheres*, **112**(D11).

Flin, F., J.-B. Brzoska, B. Lesaffre, C. Coléou and R.A. Pieritz 2004. Three-dimensional geometric measurements of snow microstructural evolution under isothermal conditions. *Annals of glaciology*, **38**: 39-44.

FPGA Company 2018. *SLF Snow Sensor - User Manual.* FPGA Company.

Gallet, J.C., F. Domine, C.S. Zender and G. Picard 2009. Measurement of the specific surface area of snow using infrared reflectance in an integrating sphere at 1310 and 1550 nm. *The Cryosphere*, **3**(2): 167-182.

Gardner, A.S. and M.J. Sharp 2010. A review of snow and ice albedo and the development of a new physically based broadband albedo parameterization. *Journal of Geophysical Research: Earth Surface*, **115**(F1).

Gerdel, R.W. 1954. The transmission of water through snow. *Eos, Transactions American Geophysical Union*, **35**(3): 475-485.

Gergely, M., F. Wolfsperger and M. Schneebeli 2014. Simulation and Validation of the InfraSnow: An Instrument to Measure Snow Optically Equivalent Grain Size. *Geoscience and Remote Sensing, IEEE Transactions on*, **52**: 4236-4247.

Green, R.O. and J. Dozier 1996. Retrieval of surface snow grainsize and melt water from AVIRIS spectra.

Green, R.O., J. Dozier, D. Roberts and T. Painter 2002. Spectral snow-reflectance models for grain-size and liquid-water fraction in melting snow for the solar-reflected spectrum. *Annals of Glaciology*, **34**: 71-73.

Green, R.O., T.H. Painter, D.A. Roberts and J. Dozier 2006. Measuring the expressed abundance of the three phases of water with an imaging spectrometer over melting snow. *Water Resources Research*, **42**(10).

Grenfell, T.C. and S.G. Warren 1999. Representation of a nonspherical ice particle by a collection of independent spheres for scattering and absorption of radiation. *Journal of Geophysical Research: Atmospheres*, **104**(D24): 31697-31709.

Gubler, H. and M. Hiller 1984. The use of microwave FMCW radar in snow and avalanche research. *Cold Regions Science and Technology*, **9**(2): 109-119.

Gupta, R.P., U.K. Haritashya and P. Singh 2005. Mapping dry/wet snow cover in the Indian Himalayas using IRS multispectral imagery. *Remote Sensing of Environment*, **97**(4): 458-469.

Hallikainen, M. 1977. Dielectric properties of sea ice at microwave frequencies. *STIN*, **78**: 11293.

Hallikainen, M., F. Ulaby and M. Abdel-Razik 1982. Measurements of the dielectric properties of snow in the 4-18 GHz frequency range. *1982 12th European Microwave Conference*, IEEE, 151-156.

Hallikainen, M., F. Ulaby and M. Abdelrazik 1986. Dielectric properties of snow in the 3 to 37 GHz range. *IEEE transactions on Antennas and Propagation*, **34**(11): 1329-1340.

Hammonds, K., R. Lieb-Lappen, I. Baker and X. Wang 2015. Investigating the thermophysical properties of the ice–snow interface under a controlled temperature gradient: Part I: Experiments & Observations. *Cold Regions Science and Technology*, **120**: 157-167.

Heilig, A., O. Eisen and M. Schneebeli 2010. Temporal observations of a seasonal snowpack using upward-looking GPR. *Hydrological Processes*, **24**(22): 3133-3145.

Heilig, A., C. Mitterer, L. Schmid, N. Wever, J. Schweizer, H.P. Marshall and O. Eisen 2015. Seasonal and diurnal cycles of liquid water in snow—Measurements and modeling. *Journal of Geophysical Research: Earth Surface*, **120**(10): 2139-2154.

Heilig, A., M. Schneebeli and O. Eisen 2009. Upward-looking ground-penetrating radar for monitoring snowpack stratigraphy. *Cold Regions Science and Technology*, **59**(2): 152-162.

Hildebrand, T. and P. Rüegsegger 1997. A new method for the model-independent assessment of thickness in three-dimensional images. *Journal of microscopy*, **185(**1): 67-75.

Hirashima, H., F. Avanzi and N. Wever 2019. Wet-snow metamorphism drives the transition from preferential to matrix flow in snow. *Geophysical Research Letters*, **46**(24): 14548-14557.

Hirashima, H., F. Avanzi and S. Yamaguchi 2017. Liquid water infiltration into a layered snowpack: evaluation of a 3-D water transport model with laboratory experiments. *Hydrology & Earth System Sciences*, **21**(11).

Hirashima, H., S. Yamaguchi and T. Katsushima 2014. A multi-dimensional water transport model to reproduce preferential flow in the snowpack. *Cold Regions Science and Technology*, **108**: 80-90.

Hori, M., K. Sugiura, K. Kobayashi, T. Aoki, T. Tanikawa, K. Kuchiki, M. Niwano and H. Enomoto 2017. A 38-year (1978–2015) Northern Hemisphere daily snow cover extent product derived using consistent objective criteria from satellite-borne optical sensors. *Remote sensing of environment*, **191**: 402-418.

Hyvarinen, T. and J. Lammasniemi 1987. Infrared measurement of free-water content and grain size of snow. *Optical Engineering*, **26**(4): 264342.

Jones, E., A. Rango and S. Howell 1983. Snowpack liquid water determinations using freezing calorimetry. *Hydrology Research*, **14**(3): 113-126.

Judson, A. and N. Doesken 2000. Density of freshly fallen snow in the central Rocky Mountains. *Bulletin of the American Meteorological Society*, **81**(7): 1577-1588.

Kendra, J.R., K. Sarabandi and F.T. Ulaby 1998. Radar measurements of snow: Experiment and analysis. *IEEE Transactions on Geoscience and Remote Sensing*, **36**(3): 864-879.

Kuroda, M. 1954. Measurement of water content of snow. *International Association of Hydrological Sciences Publication*.

Lee, J.-S. and E. Pottier 2017. *Polarimetric radar imaging: from basics to applications.* CRC press.

Leinss, S., H. Löwe, M. Proksch, J. Lemmetyinen, A. Wiesmann and I. Hajnsek 2016. Anisotropy of seasonal snow measured by polarimetric phase differences in radar time series. *The Cryosphere*, **10**(4): 1771-1797.

Lesins, G., P. Chylek and U. Lohmann 2002. A study of internal and external mixing scenarios and its effect on aerosol optical properties and direct radiative forcing. *Journal of Geophysical Research: Atmospheres*, **107**(D10): AAC 5-1-AAC 5-12.

Liang, S. and J. Wang 2020. Chapter 19 - Snow water equivalent. *Advanced Remote Sensing (Second Edition)*, Academic Press, 713-763.

Lievens, H., M. Demuzere, H.-P. Marshall, R.H. Reichle, L. Brucker, I. Brangers, P. de Rosnay, M. Dumont, M. Girotto and W.W. Immerzeel 2019. Snow depth variability in the Northern Hemisphere mountains observed from space. *Nature communications*, **10**(1): 1-12.

Lorensen, W.E. and H.E. Cline 1987. Marching cubes: A high resolution 3D surface construction algorithm. *ACM siggraph computer graphics*, **21**(4): 163-169.

Lund, J., R.R. Forster, S.B. Rupper, E.J. Deeb, H. Marshall, M.Z. Hashmi and E. Burgess 2020. Mapping snowmelt progression in the Upper Indus Basin with synthetic aperture radar. *Frontiers in Earth Science*, **7**: 318.

Lundberg, A. 1997. Laboratory calibration of TDR-probes for snow wetness measurements. *Cold Regions Science and Technology*, **25**(3): 197-205.

Marks, D., J. Domingo, D. Susong, T. Link and D. Garen 1999. A spatially distributed energy balance snowmelt model for application in mountain basins. *Hydrological processes*, **13**(12-13): 1935-1959.

Marks, D. and J. Dozier 1992. Climate and energy exchange at the snow surface in the Alpine Region of the Sierra Nevada: 2. Snow cover energy balance. *Water Resources Research*, **28**(11): 3043-3054.

Marsh, P. 1987. Grain growth in a wet arctic snow cover. *Cold Regions Science and Technology*, **14**(1): 23-31.

Marsh, P. and M.K. Woo 1984. Wetting front advance and freezing of meltwater within a snow cover: 1. Observations in the Canadian Arctic. *Water Resources Research*, **20**(12): 1853-1864.

Marshall, H.-P. and G. Koh 2008. FMCW radars for snow research. *Cold Regions Science and Technology*, **52**(2): 118-131.

Marshall, H.-P. and M. Robertson 2016. Continuous Real-time Snow Properties with Ground Penetrating Radar. *Proceedings of the 2016 ISSW, Breckenridge, CO*.

Marshall, H.-P., M. Schneebeli and G. Koh 2007. Snow stratigraphy measurements with high-frequency FMCW radar: comparison with snow micro-penetrometer. *Cold regions science and technology*, **47**(1-2): 108-117.

Marshall, H.P., G. Koh and R.R. Forster 2004. Ground-based frequency-modulated continuous wave radar measurements in wet and dry snowpacks, Colorado, USA: an analysis and summary of the 2002–03 NASA CLPX data. *Hydrological Processes*, **18**(18): 3609-3622.

MathWorks 2022. Image Processing Toolbox Reference. The MathWorks, Inc., 1397-1399.

Matzl, M. and M. Schneebeli 2006. Measuring specific surface area of snow by near-infrared photography. *Journal of Glaciology*, **52**(179): 558-564.

Matzler, C. 1996. Microwave permittivity of dry snow. *IEEE Transactions on Geoscience and Remote Sensing*, **34**(2): 573-581.

Mätzler, C. 2002. MATLAB functions for Mie scattering and absorption, version 2.

Matzler, C., H. Aebischer and E. Schanda 1984. Microwave dielectric properties of surface snow. *IEEE Journal of Oceanic Engineering*, **9**(5): 366-371.

Mazurkiewicz, A.B., D.G. Callery and J.J. McDonnell 2008. Assessing the controls of the snow energy balance and water available for runoff in a rain-on-snow environment. *Journal of Hydrology*, **354**(1): 1-14.

McGrath, D., R. Webb, D. Shean, R. Bonnell, H.P. Marshall, T.H. Painter, N.P. Molotch, K. Elder, C. Hiemstra and L. Brucker 2019. Spatially extensive ground-penetrating radar snow depth observations during NASA's 2017 SnowEx campaign: Comparison with In situ, airborne, and satellite observations. *Water Resources Research*, **55**(11): 10026-10036.

Mitterer, C., A. Heilig, J. Schweizer and O. Eisen 2011. Upward-looking ground-penetrating radar for measuring wet-snow properties. *Cold Regions Science and Technology*, **69**(2-3): 129-138.

Nolin, A.W. and J. Dozier 2000. A Hyperspectral Method for Remotely Sensing the Grain Size of Snow. *Remote Sensing of Environment*, **74**(2): 207-216.

Okorn, R., G. Brunnhofer, T. Platzer, A. Heilig, L. Schmid, C. Mitterer, J. Schweizer and O. Eisen 2014. Upward-looking L-band FMCW radar for snow cover monitoring. *Cold Regions Science and Technology*, **103**: 31-40.

Painter, T.H., A.C. Bryant and S.M. Skiles 2012. Radiative forcing by light absorbing impurities in snow from MODIS surface reflectance data. *Geophysical Research Letters*, **39**(17).

Painter, T.H. and J. Dozier 2004a. The effect of anisotropic reflectance on imaging spectroscopy of snow properties. *Remote Sensing of Environment*, **89**(4): 409-422.

Painter, T.H. and J. Dozier 2004b. Measurements of the hemispherical-directional reflectance of snow at fine spectral and angular resolution. *Journal of Geophysical Research: Atmospheres*, **109**(D18).

Painter, T.H., N.P. Molotch, M. Cassidy, M. Flanner and K. Steffen 2007. Contact spectroscopy for determination of stratigraphy of snow optical grain size. *Journal of Glaciology*, **53**(180): 121-127.

Painter, T.H., K. Rittger, C. McKenzie, P. Slaughter, R.E. Davis and J. Dozier 2009. Retrieval of subpixel snow covered area, grain size, and albedo from MODIS. *Remote Sensing of Environment*, **113**(4): 868-879.

Painter, T.H., F.C. Seidel, A.C. Bryant, S. McKenzie Skiles and K. Rittger 2013. Imaging spectroscopy of albedo and radiative forcing by light-absorbing impurities in mountain snow. *Journal of Geophysical Research: Atmospheres*, **118**(17): 9511-9523.

Perla, R.I. and M. Martinelli 1976. *Avalanche handbook.* US Department of Agriculture, Forest Service.

Picard, G., L. Arnaud, F. Domine and M. Fily 2009. Determining snow specific surface area from near-infrared reflectance measurements: Numerical study of the influence of grain shape. *Cold Regions Science and Technology*, **56**(1): 10-17.

Picard, G., L. Brucker, A. Roy, F. Dupont, M. Fily, A. Royer and C. Harlow 2013. Simulation of the microwave emission of multi-layered snowpacks using the Dense Media Radiative transfer theory: the DMRT-ML model. *Geoscientific Model Development*, **6**(4): 1061-1078.

Pielmeier, C. and M. Schneebeli 2003. Developments in the Stratigraphy of Snow. *Surveys in Geophysics*, **24**(5): 389-416.

Raymond, C.F. and K. Tusima 1979. Grain Coarsening of Water-Saturated Snow. *Journal of Glaciology*, **22**(86): 83-105.

Roth, K., R. Schulin, H. Flühler and W. Attinger 1990. Calibration of time domain reflectometry for water content measurement using a composite dielectric approach. *Water resources research*, **26**(10): 2267-2273.

Rott, H., C. Mätzler, D. Strobl, S. Bruzzi and K. Lenhart 1988. Study on SAR land applications for snow and glacier monitoring. *ESA Contract No. 6618/F/FL (SC), Final Report*.

Rott, H., S.H. Yueh, D.W. Cline, C. Duguay, R. Essery, C. Haas, F. Heliere, M. Kern, G. Macelloni and E. Malnes 2010. Cold regions hydrology high-resolution observatory for snow and cold land processes. *Proceedings of the IEEE*, **98**(5): 752-765.

Rowe, P., M. Fergoda and S. Neshyba 2020. Temperature-Dependent Optical Properties of Liquid Water From 240 to 298 K. *Journal of Geophysical Research: Atmospheres*, **125**(17): e2020JD032624.

Rutter, N., M.J. Sandells, C. Derksen, J. King, P. Toose, L. Wake, T. Watts, R. Essery, A. Roy and A. Royer 2019. Effect of snow microstructure variability on Ku-band radar snow water equivalent retrievals. *The Cryosphere*, **13**(11): 3045-3059.

Sarabandi, K. and F.T. Ulaby 1990. A convenient technique for polarimetric calibration of single-antenna radar systems. *IEEE Transactions on Geoscience and Remote Sensing*, **28**(6): 1022-1033.

Schleef, S., M. Jaggi, H. Löwe and M. Schneebeli 2014. An improved machine to produce nature-identical snow in the laboratory. *Journal of Glaciology*, **60**(219): 94-102.

Schmid, L., A. Heilig, C. Mitterer, J. Schweizer, H. Maurer, R. Okorn and O. Eisen 2014. Continuous snowpack monitoring using upward-looking ground-penetrating radar technology. *Journal of Glaciology*, **60**(221): 509-525.

Schneebeli, M. 1995. Development and stability of preferential flow paths in a layered snowpack. *IAHS Publications-Series of Proceedings and Reports-Intern Assoc Hydrological Sciences*, **228**: 89-96.

Schneebeli, M. and S.A. Sokratov 2004. Tomography of temperature gradient metamorphism of snow and associated changes in heat conductivity. *Hydrological Processes*, **18**(18): 3655-3665.

Seidel, F.C., K. Rittger, S.M. Skiles, N.P. Molotch and T.H. Painter 2016. Case study of spatial and temporal variability of snow cover, grain size, albedo and radiative forcing in the Sierra Nevada and Rocky Mountain snowpack derived from imaging spectroscopy. *The Cryosphere*, **10**(3): 1229-1244.

Seligman, G., G.A. Seligman and C. Douglas 1936. *Snow structure and ski fields: being an account of snow and ice forms met with in nature, and a study on avalanches and snowcraft.* Macmillan and Company, limited.

Shea, C., B. Jamieson and K. Birkeland 2012. Use of a thermal imager for snow pit temperatures. *The Cryosphere*, **6**(2): 287-299.

Shekhar, C., S. Srivastava, H.S. Negi and M. Dwivedi 2019. Hyper-spectral data based investigations for snow wetness mapping. *Geocarto International*, **34**(6): 664-687.

Shenoi, B.A. 2005. *Introduction to digital signal processing and filter design.* John Wiley & Sons.

Shi, J. and J. Dozier 1992. Radar backscattering response to wet snow. *Proc. IGARSS'92*, 927.

Shi, J. and J. Dozier 1995. Inferring snow wetness using C-band data from SIR-C's polarimetric synthetic aperture radar. *IEEE transactions on geoscience and remote sensing*, **33**(4): 905-914.

Sihvola, A. and M. Tiuri 1986. Snow fork for field determination of the density and wetness profiles of a snow pack. *IEEE Transactions on Geoscience and Remote Sensing*, (5): 717-721.

Simpkins, G. 2018. Snow-related water woes. *Nature Climate Change*, **8**(11): 945-945.

Skiles, S.M., M. Flanner, J.M. Cook, M. Dumont and T.H. Painter 2018. Radiative forcing by light-absorbing particles in snow. *Nature Climate Change*, **8**(11): 964-971.

Skiles, S.M. and T. Painter 2017. Daily evolution in dust and black carbon content, snow grain size, and snow albedo during snowmelt, Rocky Mountains, Colorado. *Journal of Glaciology*, **63**(237): 118-132.

Skiles, S.M. and T.H. Painter 2018. Assessment of radiative forcing by light-absorbing particles in snow from in situ observations with radiative transfer modeling. *Journal of Hydrometeorology*, **19**(8): 1397-1409.

Stamnes, K., S.-C. Tsay, W. Wiscombe and K. Jayaweera 1988. Numerically stable algorithm for discrete-ordinate-method radiative transfer in multiple scattering and emitting layered media. *Applied optics*, **27**(12): 2502-2509.

Stein, J., G. Laberge and D. Lévesque 1997. Monitoring the dry density and the liquid water content of snow using time domain reflectometry (TDR). *Cold Regions Science and Technology*, **25**(2): 123-136.

Tiuri, M., A. Sihvola, E. Nyfors and M. Hallikaiken 1984. The complex dielectric constant of snow at microwave frequencies. *IEEE Journal of oceanic Engineering*, **9**(5): 377-382.

Ulaby, F.T. 1982. Microwave remote sensing active and passive. *Rader remote sensing and surface scattering and emission theory*: 848-902.

Waldner, P.A., M. Schneebeli, U. Schultze-Zimmermann and H. Flühler 2004. Effect of snow structure on water flow and solute transport. *Hydrological Processes*, **18**(7): 1271-1290.

Walker, A. and B. Goodison 1993. Discrimination of a wet snow cover using passive microwave satellite data. *Annals of Glaciology*, **17**: 307-311.

Walter, C.H. 1970. *Traveling wave antennas.* New York: Dover Publications.

Warren, S.G. 1982. Optical properties of snow. *Reviews of Geophysics*, **20**(1): 67-89.

Warren, S.G. and R.E. Brandt 2008. Optical constants of ice from the ultraviolet to the microwave: A revised compilation. *Journal of Geophysical Research: Atmospheres*, **113**(D14).

Webb, R., M.W. Williams and T. Erickson 2018a. The spatial and temporal variability of meltwater flow paths: Insights from a grid of over 100 snow lysimeters. *Water Resources Research*, **54**(2): 1146-1160.

Webb, R.W., S.R. Fassnacht and M.N. Gooseff 2018b. Hydrologic flow path development varies by aspect during spring snowmelt in complex subalpine terrain. *The Cryosphere*, **12**(1): 287-300.

Webb, R.W., K. Jennings, S. Finsterle and S.R. Fassnacht 2021. Two-dimensional liquid water flow through snow at the plot scale in continental snowpacks: simulations and field data comparisons. *The Cryosphere*, **15**(3): 1423-1434.

Wiesmann, A. and C. Mätzler 1999. Microwave emission model of layered snowpacks. *Remote sensing of environment*, **70**(3): 307-316.

Williams, M.W., T.A. Erickson and J.L. Petrzelka 2010. Visualizing meltwater flow through snow at the centimetre-to-metre scale using a snow guillotine. *Hydrological Processes*, **24**(15): 2098-2110.

Winebrenner, D., D. Long and B. Holt 1998. Mapping the progression of melt onset and freeze-up on Arctic sea ice using SAR and scatterometry. *Analysis of SAR Data of the Polar Oceans*, Springer, 129-144.

Wiscombe, W.J. and S.G. Warren 1980. A Model for the Spectral Albedo of Snow. I: Pure Snow. *Journal of the Atmospheric Sciences*, **37**(12): 2712-2733.

Yamaguchi, S., T. Katsushima, A. Sato and T. Kumakura 2010. Water retention curve of snow with different grain sizes. *Cold Regions Science and Technology*, **64**(2): 87-93.

Yosida, Z. 1940. A Method for Determining the Thaw Water Content in a Snow Layer. *Journal of the Meteorological Society of Japan. Ser. II*, **18**(10): 321-328.

Zuanon, N., A2 Photonic Sensors 2013. IceCube, a portable and reliable instrument for snow specific surface area measurement in the field. *International Snow Science Workshop*, Grenoble – Chamonix Mont-Blanc

APPENDICES

APPENDIX A

SUPPLEMENTARY TABLE 1. EFFECTIVE GRAIN RADIUS LOOKUP TABLE

(0^{o} ILLUMINATION ANGLE)

Supplementry Table 1. Effective Grain Radius Lookup Table (0^o Illumination Angle)	
Effective Grain Radius (r_e) (µm)	Scaled Band Area (A_b)
30	0.565
40	0.641
50	0.710
60	0.777
70	0.842
80	0.903
90	0.962
100	1.017
150	1.247
200	1.428
250	1.583
300	1.722
350	1.848
400	1.965
450	2.072
500	2.174
550	2.270
600	2.359
650	2.443
700	2.525
750	2.602
800	2.675
850	2.746
900	2.813
950	2.880
1000	2.939
1050	2.998
1100	3.057
1150	3.115
1200	3.169
1250	3.219
1300	3.269
1350	3.321
1400	3.368
1450	3.415
1500	3.460